Spectral modeling of Cassini-VIMS data to investigate the surface properties of Enceladus

Owain Fryer
TU4040

Delft University of Technology

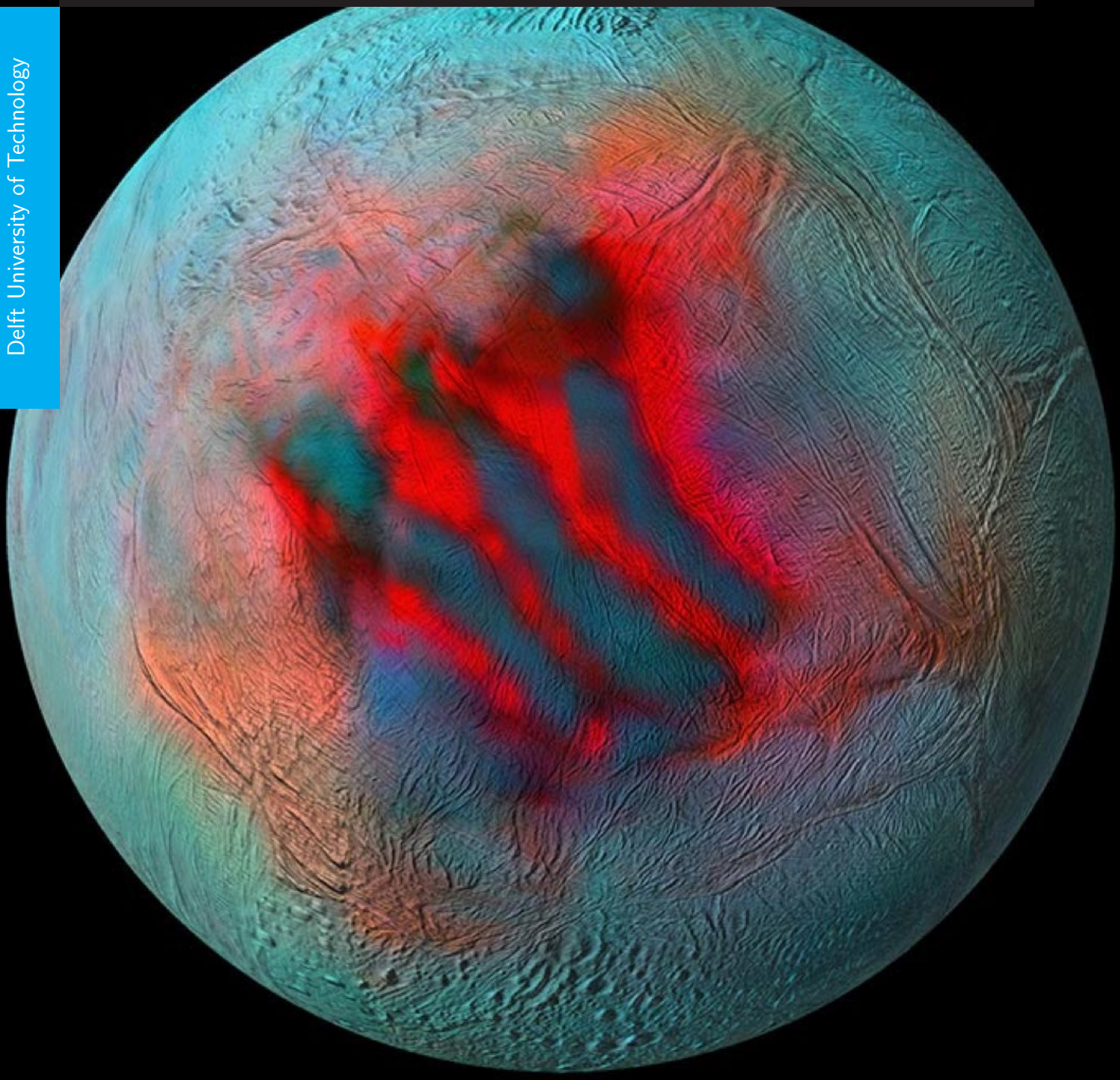

Spectral modeling of Cassini-VIMS data to investigate the surface properties of Enceladus

Master Thesis

by

Owain Fryer

in partial fulfillment of the requirements for the degree of

Master of Science
in Aerospace Engineering

at Delft University of Technology

Supervised By:
Dr. S. CAZAUX

Committee Members:
Dr. Ir. E. Mooij,
Dr. Ir. W. van der Wal,
Dr. J. Loicq,
Ir. M. S. Fayolle-Chambre

An electronic version of this thesis can be found at `https://repository.tudelft.nl/`.

TU Delft Delft University of Technology

Acknowledgements

The work done on this report represents nearly a year's worth of research. During this time, I have had help from several people to complete this work. First, I would like to thank my thesis supervisor, Dr. Stéphanie Cazaux. Our weekly meetings helped me stay on track over this year-long period and allowed me to use my time efficiently. I would also like to thank my assessment committee members. In particular, Marie Fayolle-Chambre guided me during my research and shared her work using the Hapke model. Outside of the university, I would like to thank Benoît Seignovert and the Laboratoire de Planétologie et Géodynamique (LPG) of Nantes University for providing software and python notebooks that aided in collecting and processing the VIMS data. Lastly, I would like to thank everyone that has taken an interest in my thesis project.

Contents

1 Introduction

Saturn's second moon Enceladus gained scientific interest after the discovery of jets were found emerging from the southern pole of the moon. Since this discovery was made at the beginning of the Cassini mission, the orbiter was able to make more observations of the icy moon before the mission was complete. These observations allowed for large sets of data to be collected and researched to learn more about Enceladus. This research will use the data acquired by the Cassini mission to obtain more information about the surface of Enceladus.

Much research has been done on the southern pole of Enceladus since the plumes in this region are of interest. This research has led to many hypotheses about what is occurring beneath the surface of the moon. One study compared the southern region of Enceladus to the rest of the moon and discovered a region in the northern hemisphere which has similar features known as the red region. The correlation between the two regions was unknown. There have been studies that map the grain size and crystallinity values of the ice on the surface of Enceladus. These studies found the south pole had larger values than the rest of the surface due to the presence of the plumes.

This study will determine the grain size, density, surface roughness, crystallinity, and temperature of the surface ice on Enceladus to increase our understanding of the processes occurring on the icy moon. This will be done by using the data collected from the VIMS instrument onboard the Cassini spacecraft. The data will be corrected to allow for the data collected at different viewing angles to be compared to one another. The data will then be compared to laboratory optical constants of water ice to determine the parameters mentioned above. The surface will be split up into three regions that will be compared: the red region in the northern hemisphere, the crater region, and the tiger stripes region. Comparing these regions aim to give insight into the ways that the surface of Enceladus has formed and continues to change. The results found in this study could be useful in further research on the surface of Enceladus and other moons in the Saturn system. Knowing more about Enceladus is useful in understanding the formations and processes occurring on bodies in our solar system. This study hopes to answer the following research questions:

- What regions on Enceladus have enough VIMS data to make the comparisons?
- What does the infrared spectra of each location tell us about the ice?
  - What is the size of the ice particles?
  - What is the density of the surface?
  - What is the roughness of the surface?
  - What is the ratio of crystalline and amorphous ice?
  - What is the temperature of the observed surface?
- When comparing the regions, what similarities and differences are found, and what does this reveal about the process occurring beneath the ice?
- What trends can be observed locally in the different regions and what can that reveal about the surface?
- Is the anomaly in the northern hemisphere due to plume debris or resurfacing?

This report will consist of seven additional sections. Section 2 will discuss the Saturn system and introduce one of Saturn's moons Enceladus. Section 3 will discuss the Cassini-Huygens mission and explain the process of spectroscopy. Section 4 will detail the methods used to acquire and process the data that is used in the study. Section 5 will explain the model used to compare the data and extract the results. Section 6 will show the results from the study. Section 7 will discuss the results and provide a conclusion and recommendation for future work. Finally, Section 8 will validate the results found in this study by comparing the patterns found in previous work completed. These chapters will aim to answer the research questions mentioned above.

2 Enceladus and the Saturn System

This section will discuss the Saturn system in Section 2.1 and give a more in-depth look at the target of this study, Saturn's second moon Enceladus in Section 2.2.

2.1 Saturn System

It was previously thought that the rings of Saturn were formed from debris leftover from the formation of the planet. The debris makeup from this formation would lead to a half-rock, half-ice mixture which is similar to the composition of many satellites in the outer region of our Solar System [1]. The composition of Saturn's rings is more than 90 percent water ice. Saturn only has one large satellite, Titan, which is rare for a planet the size of Saturn. This implies that Saturn at one point in time had other much larger satellites that were destroyed due to tidal forces tearing the satellites apart as they migrated inward towards Saturn [1]. The formation of Saturn's rings from the destruction of one or more of Saturn's satellites would account for the current makeup of the rings and their lack of rock composition [2]. Figure 1 shows the seven major ring groupings and seven major moons. The letters assigned to each ring are ordered by how early the ring section was discovered. Rings D, C, B, and A are within the Roche limit, which is why there are no large moons that have formed this close to Saturn [3]. Within this limit, the tidal forces are strong enough to pull apart debris and stop the formation of large objects [4]. Once outside of this limit, the tidal forces lessen, which allows for the formation of moons. The seven major moons of Saturn are Mimas, Enceladus, Tethys, Dione, Rhea, Titan, and Iapetus. This study will focus on the iciest moon of Saturn, Enceladus.

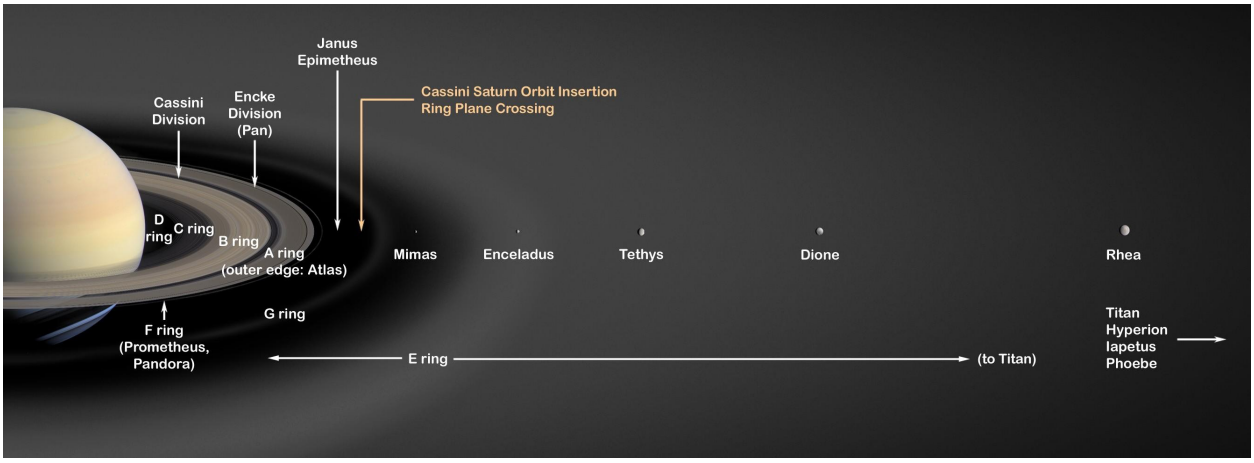

Figure 1: Layout of the Rings of Saturn [3]

2.2 Enceladus

This section will discuss the main geological features of Saturn's second-closest moon Enceladus. Enceladus has a 500-kilometer diameter and is Saturn's sixth-largest moon [5]. The surface of the moon is mostly covered with clean white ice which makes it the most reflective body in our Solar System with a geometric albedo of 1.375 [5]. Since the reflective properties of the ground are so high, the little heat is absorbed from the light which makings Enceladus an extremely cold

body. The surface of Enceladus varies greatly from older portions of the surface which have been bombarded with debris to newer portions of the surface which have been deformed by the moon's plate tectonics. In 2005, the Cassini spacecraft discovered water-rich plumes ejecting from the southern pole of the moon which astronomers concluded is from a subsurface ocean of liquid water. These observations along with the fact there are few impact craters on the south polar region show that Enceladus is currently geologically active [5]. The features of the moon that will be expanded upon are the moon's surface, plumes, and subsurface ocean. These geological features will be useful while examining the data found from the Cassini mission data.

2.2.1 Plumes and Subsurface Ocean

The plumes on Enceladus are only found emanating from the south pole of the moon. The openings of the plumes stretch along with the four fractures in the surface known as the tiger stripes. The tiger stripes are composed of double ridges and the center of which can be 2 km wide and 0.5 km deep [6]. Although most of the plumes emanate from within these double ridges, some plume jets can be found emitting from simple fractures without complex structures. The measurements collected from Enceladus have shown that the source of the plumes is connected to an underlying ocean below the crust of the moon. The major processes in the model are shown below in Figure 2a [6]. In Figure 2a near the surface of Enceladus, there is a lateral motion of the crust which causes the cracks to open and close due to forces caused by the tidal stress [6]. The presence of an ocean enhances the flexing of the crust by generating large tidal stresses. The tiger stripes are aligned with one of the maximum tidal stress directions and are believed to be formed in response to these stresses [6]. These stresses now control the width of the cracks depending on how large the tidal forces are. Evidence of this phenomenon has been observed that the overall brightness of the plumes is greater at the moon's apoapsis than it is at its periapse [6]. The plume will become brighter when more mass is ejected from the surface. The activity of the plumes still occurs at the periapse which implies that the cracks do not close entirely.

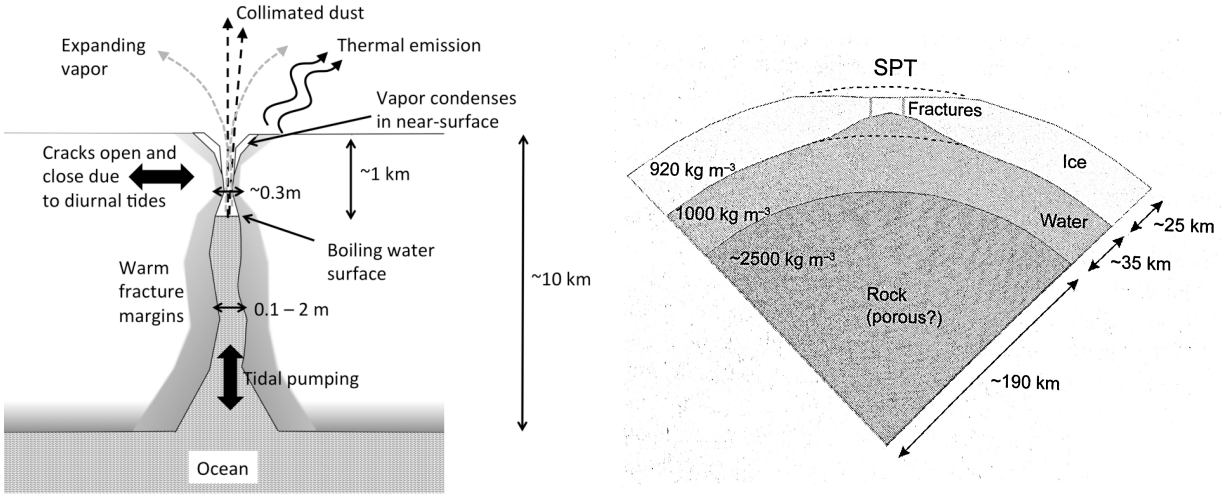

(a) Plume schematic of the plumbing connecting the surface of of Enceladus to the underlying ocean. [6]

(b) Schematic of the Subsurface layers of Enceladus. [7]

Figure 2: The internal processes and formations below the surface of Enceladus.

Enceladus is far from the sun and has a reflective surface, it was assumed that the moon was solid ice throughout its core. The plumes are composed primarily of solid water ice and a gaseous component. The gaseous component is largely made up of water vapor and has minor traces of CO_2, NH_3, CH_4, and H_2 [6]. Figure 3 shows the mixing ratios from Cassini's fifth flyby. H_2 becomes present when H_2O dissociation occurs, and the atoms split in an irreversible process [8]. The minor presence of those gas species suggests that there is hydrothermal cycling between a rocky interior and a cryosphere. This implies that there is a liquid ocean below the layer of ice crust which is shown in Figure 2b. Ammonia (NH_3) has a dramatic effect when mixed with liquid water and can lower the freezing point by almost 100 K [9]. The presence of ammonia makes it easier for a subsurface ocean to be sustained below the ice on Enceladus. If the water temperature drops below the freezing point, the H2O particles will freeze, and the ammonia will be more concentrated in the remaining liquid water [7]. This increase of ammonia in the liquid water will make it increasingly more difficult to freeze the water due to the increase in the concentration of ammonia [9]. The solid portion of debris has a presence of sodium and potassium salt [6]. This is another indication that the source of the plumes is a liquid ocean below the surface. If the source of the solid particles had been from a gas that sublimated as it came to the surface, the solid portion of the debris would be nearly salt-free. The liquid water interacts with silicates below the surface of the crust and dissolves the salt. The only way for the plum debris to contain the salt deposits is if the droplets of the liquid are frozen quickly. The salty grains found in the debris imply that there must be a direct connection between the liquid water source and the vacuum of space [6]. If the liquid were to freeze slowly, the water particles would freeze, but the salt would remain in the liquid water. The particles would then be primarily water without any traces of salt. This conclusion is shown in Figure 2a as the liquid ocean connects to the surface of Enceladus and ejects out into space.

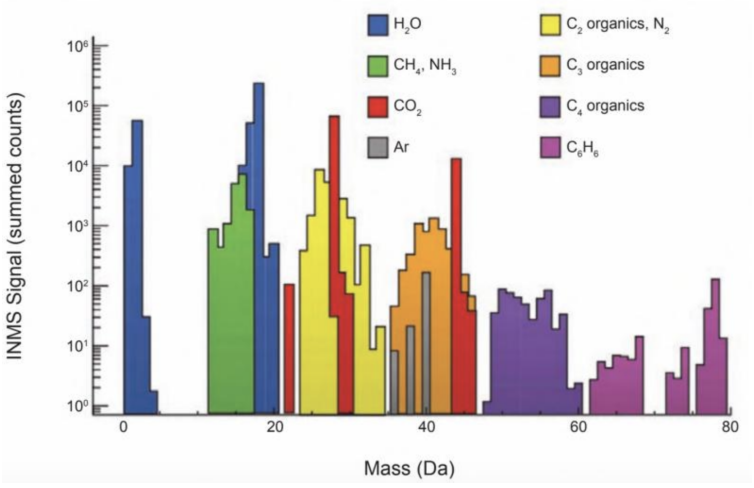

Figure 3: Volume mixing ratios based on analysis of the data collected from Cassini during its fifth flyby of Enceladus. Due to the high velocity of the flyby, the spectrum is dominated by species from molecular fragmentation of high mass organic compounds probably residing in plume ice grains. [8]

2.2.2 Surface Characteristics

Understanding the surface of Enceladus and the way its geological features are laid out helps better provide context for the data that has been collected from the Cassini mission. The surface of Enceladus is made up of four main geological regions. Each of these regions can be shown below in

Figure 4. The four regions are the cratered terrain, trailing hemisphere terrain, leading hemisphere terrain, and the south polar terrain [10]. As shown below in Figure 4, each of the regions can be split up into sub-regions where the land within each region changes. The four geological regions of Enceladus can be put into time epochs from how old the surface history is. The youngest region is the south polar terrain which is still active. This region is called the 'tiger stripes' region and is dominated by large fractures in the ice where large plumes emerge. The second oldest regions are the leading and trailing hemispheres which have ridges and troughs associated with geological activity. Enceladus is tidally locked to Saturn and takes the same amount of time to rotate around its axis as it does to rotate around Saturn [10]. The leading hemisphere is always pointing in the direction of motion of Enceladus. The oldest region of Enceladus is the cratered terrain which is noted by the large amounts of craters in the region [10].

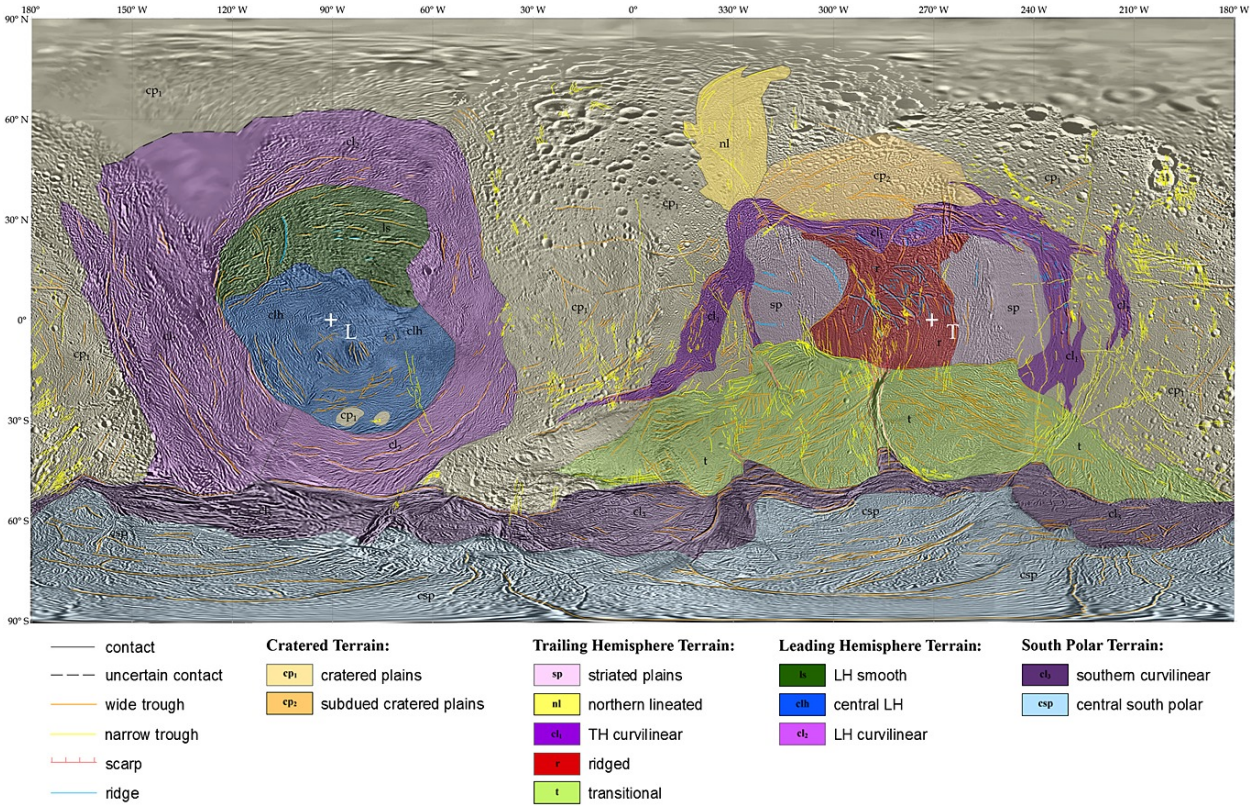

Figure 4: Mosaic Terrain Map of Enceladus [10]

2.2.3 Previous Studies on the Surface of Enceladus

Several studies have been performed on the surface of Enceladus. Many of these studies directed their attention to the plume region in the southern hemisphere or at the surface of Enceladus as a whole. This section will discuss previous works that have been done which relate to this study.

Many studies focus on the crystallinity and grain size of the ice around the surface of Enceladus. The most recent study was conducted by Robidel et al. (2020) and the Nantes University to make a mosaic of the surface of Enceladus [11]. The cubes used in this study have been applied a correction that corrects for the extreme viewing angles at the edges of data cubes. These extreme viewing

angles caused the edges of the images to have seams. The correction that was applied allowed for a smooth transition between images to make the mosaic more impressive. The same photometric correction will be applied to the data in this study to allow for better comparisons of different data points. The mosaic was a false-color image that shows locations with high crystallinity points and grain size. The more red the location, the higher the values. The method for finding these results was found by finding the ratio between the 3.1 and 1.65 μm absorption bands. These bands are a strong indicator of crystallinity and grain size of water ice. Figure 5 shows the mosaic that was produced. This study found large values of crystalline ice and large grain sizes around the tiger stripe region, which was expected. The study found an anomaly in the northern hemisphere which also had large values of crystallinity and grain size. The study was unable to go into more detail as to what the cause behind this anomaly is since it was not in the scope of the research goal. This study will push further the analysis of the VIMS data compared to Nantes, as the Hapke model will be used to determine detailed characteristics of the surface.

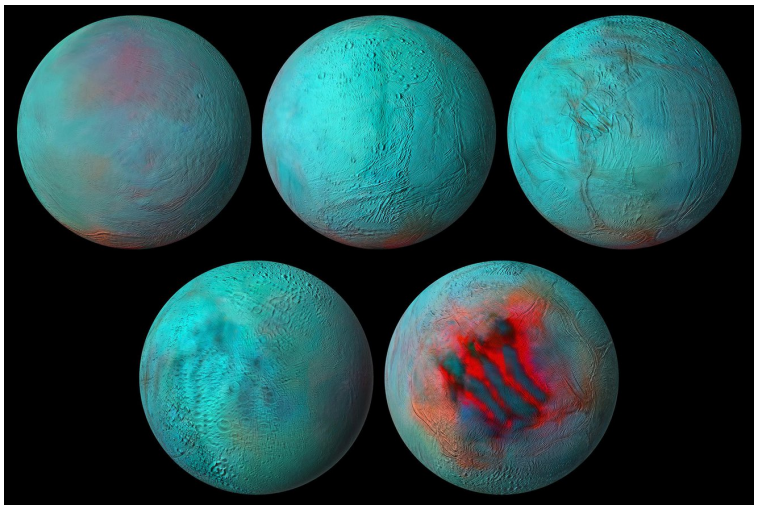

Figure 5: Infrared composite images of Enceladus from Cassini data. [11]

Another study that focuses on the crystallinity of water ice on the surface of Enceladus was performed by Newman et al. (2008) [12]. The study looked at the levels of crystalline and amorphous ice on the surface. The different percentages of ice shed light on the processes that are occurring on the surface such as the formation and evolution. The difference between the ice types can be seen in many different wavelengths of the spectra. Crystalline ice is formed by freezing the ice at higher temperatures so it will freeze slowly and the molecules will be able to arrange in a uniform arrangement. Amorphous ice is normally formed by the ice being frozen rapidly at very low temperatures. Newman goes on to talk about how amorphous ice can also be created from damaged crystalline ice particles. The crystalline ice gets bombarded by radiation and breaks down the uniform arrangement, and after long periods will turn into crystalline ice. The analysis of the south pole shows that the radiation has caused a large portion of the surface to be amorphous, but the region is continually recrystallized due to the high temperatures [12].

Studies have been performed by Filacchione et al. (2016), which have investigated the surface temperature of Saturn's icy satellites [13]. In this study, the temperature of the surface was determined by looking at the 3.6 μm peak that occurs in crystalline water ice. The location of the peak shifts with the change of temperature. The study creates partial mosaics of the surface of seven of Saturn's moons. Figure 6 shows the partial mosaic of the surface of Enceladus and the location of the 3.6 μm peak.

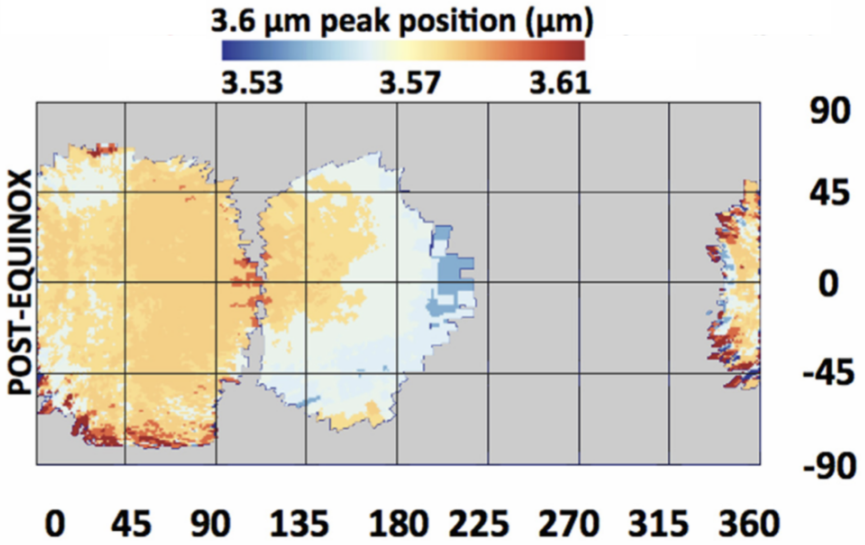

Figure 6: Post-equinox temperature map showing the different deposition temperatures of water ice on the surface of Enceladus. The latitude on this map is the same orientation as the latitude used throughout this study; however, the longitude differs. 0° on this map correlates to 180°W, 180° correlates to 0°, and 360° correlates to 180°E.

3 Cassini-Huygens Mission and Spectroscopy

3.1 Cassini-Huygens Mission

The Cassini-Huygens mission, which is commonly referred to as the Cassini mission, was a joint mission between NASA, the European Space Agency (ESA), and the Italian Space Industry. The main purpose of this mission, which will further be explained in Section 3.1.2, was to explore the Saturn system, which included the rings and satellites of Saturn. The mission comprised of two components, the Cassini space probe, and the Huygens lander. The Huygens lander was scheduled to land on Saturn's largest moon, Titan. The Cassini probe was scheduled to study the planet and its system from a separate orbit around Saturn. Pertaining to Enceladus, Cassini acquired data from the moon to explain the composition, temperatures, and structures present of the surface [14]. The trajectory of the mission and its orbit around Saturn will be explained in more detail in Section 3.1.1. In Section 11, more detail of the relevant instrumentation used onboard the Cassini mission will be provided.

3.1.1 Trajectory

Cassini was launched on October 15, 1997, and was active in space for almost 20 years. The Cassini mission orbited Saturn for 13 years after entering the planet's orbit on July 1, 2004 [15]. During the almost seven-year voyage to the Saturn system, Cassini made gravity-assist maneuvers around Venus, Earth, and Jupiter [15]. This section will explain the trajectory of the Cassini probe as it pertains to the research that will be conducted in this project.

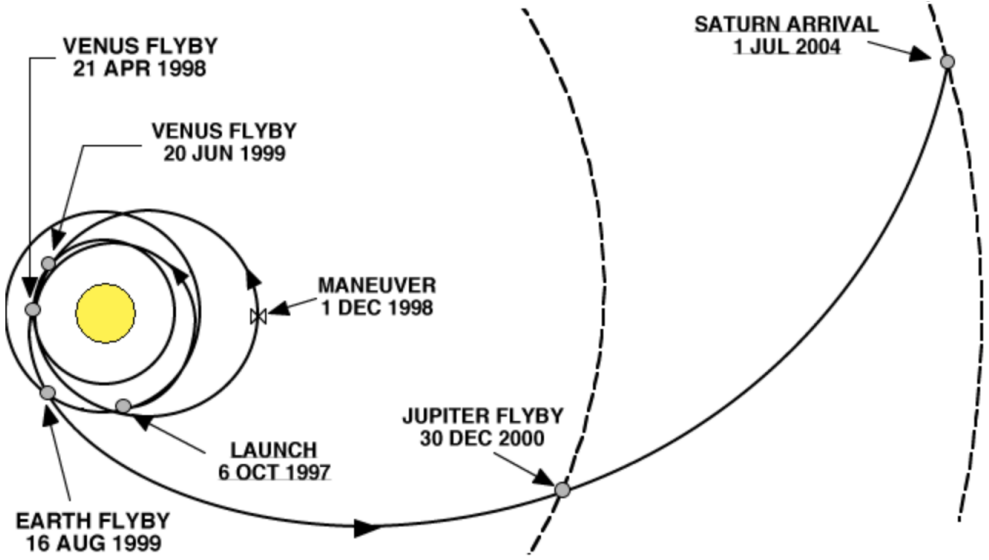

Figure 7: Trajectory of Cassini [16]

The spacecraft had a complex trajectory after it left Earth and started its trip to the Saturn system. The spacecraft made four gravity-assist maneuvers around three different planets which can be seen in Figure 7. Cassini started its trajectory by making two swing-by's of Venus on April 21, 1998, and June 20, 1999. After the second swing-by of Venus, Cassini made a swing-by of Earth on August 16, 1999, on a path for Jupiter. On December 30, 2000, Cassini made its final gravity-assist maneuver as it made a swing-by of Jupiter [17]. Finally, on July 1, 2004, Cassini arrived at Saturn

and began its orbit around the planet. This complicated flight plan for Cassini was necessary since the satellite itself was heavy and the rocket technology at the time was not able to push the satellite further out into Saturn's orbit within a relatively short amount of time.

After Cassini arrived in the Saturn system, it began collecting data to complete the scientific goals of the mission. Cassini was able to discover two new moons of Saturn that were previously unknown: Methone and Pallene [18]. In October of 2004, Cassini made its first flyby of Titan and collected data which concluded that the surface of the moon was relatively level with peaks no more than 50 meters in altitude [19]. Cassini also took clear photos of the moon which can be seen below in Figure 8 showing the surface beneath Titan's thick atmosphere. At the end of 2004, the Huygens lander was deployed to land on Titan. The most notable discovery from the Huygens lander was that there are methane lakes on the surface of the moon that get replenished by rain from hydrocarbon clouds. Also, data from both the Cassini probe and the Huygens lander provided evidence that Titan has an internal liquid ocean beneath the surface.

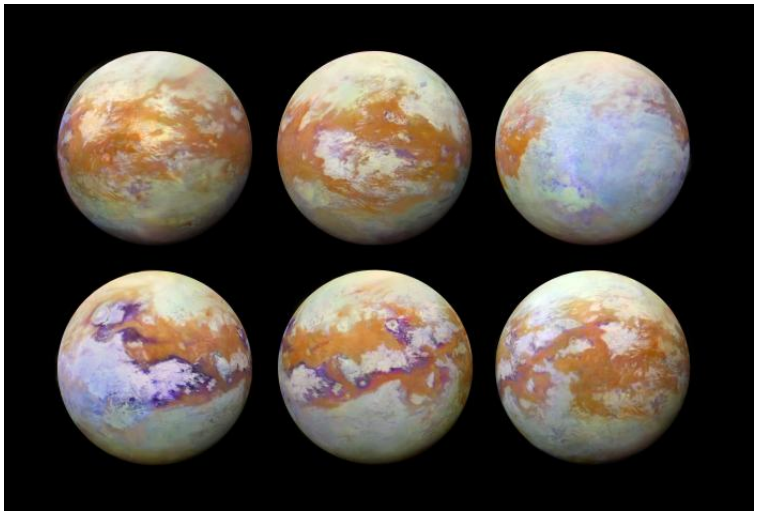

Figure 8: Six images of Titan taken by the Cassini spacecraft using infrared imaging from the VIMS instrument. [19]

In 2005, Cassini made its first flyby of Enceladus. The probe detected a significant exosphere present around the moon and a strange change in the magnetic field of Saturn during the flyby of the moon [20]. After the data had been processed, it was concluded that this flux in the magnetic field was caused by the escape of magnetic particles from the surface of Enceladus [20]. This caused the team of scientists to allow for more flyby's of the moon, and in July of 2005, the cameras onboard Cassini captured images of water vapor and ice particles being ejected from the moon. This discovery became a large focus for the remainder of the mission and allowed Cassini to complete 23 flybys of Enceladus [20]. The Cassini mission was supposed to only last until 2008; however, the mission was extended two times. The first extension was a two-year-long mission called the Cassini Equinox Mission and the second extension was a seven-year-long mission called the Cassini Solstice Mission [21]. These two extensions allowed the Cassini probe to complete 60 additional orbits around Saturn in the Equinox Mission, and an additional 155 orbits in the Solstice Mission [21]. At the end of the Cassini Mission, the conclusion was known as The Grand Finale which can be seen below in Figure 9. During this phase, the probe would make 22 deep dives into the planet's cloud tops and innermost rings. After the deep dives were complete, the probe plunged

into Saturn's inner atmosphere and was burnt up and destroyed in 2017 [21]. The destruction of the probe was to ensure that the surrounding moons would not be contaminated by any foreign materials or organisms on board.

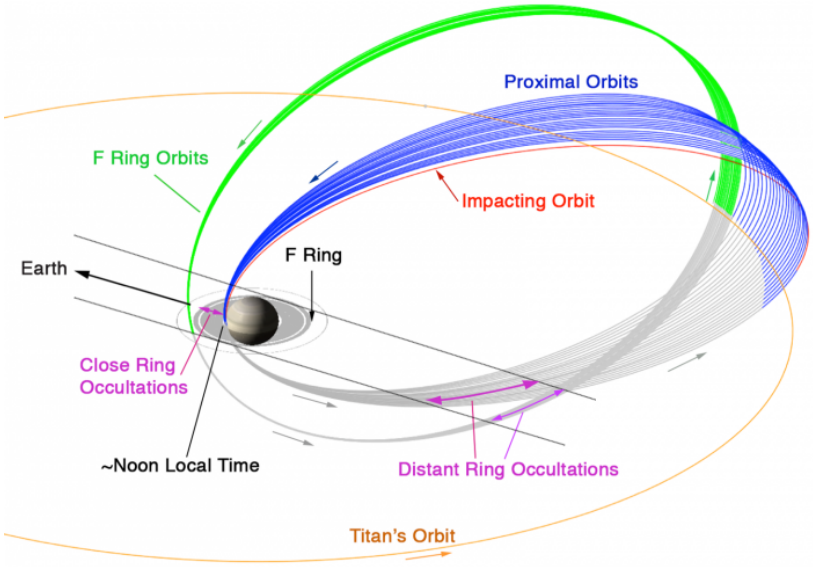

Figure 9: Trajectory of Cassini during The Grand Finale stage [22]

3.1.2 Objectives

As mentioned above in the previous section, the Cassini-Huygens mission had three phases: the Prime phase, the Equinox phase, and the Solstice phase. Each of these phases had different objectives set out by the team operating the mission. The original objectives for the mission were split into five categories: Saturn, its rings, the magnetosphere, the icy moons, and Titan. The focus of the literature study is on the data acquired from the Cassini mission of Saturn's icy moons. Therefore, only the objectives related to the icy moons will be discussed. The objectives for Cassini studying Saturn's icy moons during the Primary phase are shown below [23].

- Map the surface geology and composition and determine the icy moon's geological histories.
- Determine the physical processes responsible for the surface and subsurface structure.
- Determine their bulk compositions and internal structure.
- Investigate their interactions with Saturn's magnetosphere and ring system.

The following objectives were to be completed for icy moons during the Equinox Mission phase [23].

- Study long-term seasonal changes on the mid-sized moons Enceladus, Rhea, Thethys, Dione, Mimas, and Iapetus.
- Based on new information aquired during the Primary phase, determine whether Enceladus has an ocean, and search for possible anomalies in its internal structure.
- Determine whether Rhea has a ring system of its own.

- Search for low-level activity on Dione, such as a tenuous exosphere.

The following objectives were to be completed for icy moons during the Solstice Mission phase [23].

- Monitor long-term variability - in particular, seasonal variations in cryo-volcanic activity on Enceladus to help provide new constraints on the mechanism behind the moons plume formation.
- Study potential temporal variability especially in Enceladus' ocean and interior structure, Dione's activity, Rhea's differntation state.
- Carry out a comparative study of Saturn's mid-sized moons, specifically their cratering and comparative geology and surface compositions.

The data gathered from each of these three phases of the Cassini mission allowed for a multitude of measurements and information available for the icy moon of Enceladus. The data from this mission was acquired from a suite of instruments, which will be described in the section below.

3.1.3 Instrumentation

To complete the mission objectives listed above, Cassini contained a wide variety of remote sensing and in-situ instrumentation. On the orbiter, there are ten instruments, many of which are capable of multiple functions from which data can be gathered. The orbiter and the instrumentation onboard can be seen below in Figure 10. The description of each instrument and what each instrument will be recording can be seen below in Table 1.

In the MSc project, the research will focus on two of the spectrometers onboard the Cassini probe. The first is the Visible and Infrared Mapping Spectrometer (VIMS) and the second is the Composite Infrared Spectrometer (CIRS), both of these are circled in Figure 10. Both of these instruments are remote sensing and will be analyzing the surface of Enceladus as Cassini fly's by the moon. Both of these instruments are used to determine the composition, distribution, and thermal characteristics of the icy moon's surface materials.

The Cassini VIMS instrument was used for remote sensing capturing images using visible and infrared (IR) light. The instrument consists of two cameras, one to measure the visible light, the other the infrared. VIMS measures reflected and emitted radiation from wavelengths between 350 and 5100 nm [14]. The IR camera consists of a Cassegrain telescope which will point along with the instrument's instantaneous field of view (IFOV) [14]. The IFOV of the camera will be considered as one pixel of the overall image. As the IFOV sweeps across it will collect data which will create a row of pixels and then drop down to the next row. This process is repeated until a single image full of these "pixels" is put together [24]. The IFOV of VIMS is 1.8° X 1.8° and will be put together by a 3 by 3 layout of the pixels [24]. VIMS achieves a spectral resolution of 7.3 nm and a spatial resolution of 500 µrad [24]. The visible camera consists of a Shafer telescope which will collect data with the same resolution as the IR camera. This camera's IFOV is an entire row of pixels [14]. A two-dimensional image using this camera is created when the camera is scanned over the scene and the rows of pixels are arranged together to form the image.

Dual Technique Magnetometer-	Studied Saturn's magnetic field and its interactions with the solar wind, the rings and moons of Saturn.
Visible and Infrared Mapping Spectrometer-	Identified chemical compositions on the surfaces, atmospheres, and rings of Saturn and its moons by measuring colours of visible light and infrared energy emitted or reflected.
Radio and Plasma Wave Science Instrument-	Investigated plasma waves, natural emissions of radio energy, and dust.
Imaging Science Subsystem-	Took pictures in visible, near-ultraviolet, and near-infrared light.
Composite Infrared Spectrometer-	Measured infrared energy from the surfaces, atmospheres, and rings of Saturn and its moons to study their temperature and compositions.
Radio-	Searched for gravitational waves in the Universe. Studied the atmosphere, rings, and gravity fields of Saturn and its moons by measuring telltale changes in radio waves sent from the spacecraft.
Ion and Neutral Mass Spectrometer-	Examined neutral and charged particles near Titan, Saturn, and moons to learn more about their extended atmospheres and ionospheres.
Cassini Plasma Spectrometer-	Explored plasma within and near Saturn's magnetic field.
Magnetosphere Imaging Instrument-	Imaged Saturn's magnetosphere and measured interactions between the magnetosphere and solar wind.
Ultraviolet Imaging Spectrograph-	Measured ultraviolet energy from atmospheres and rings to study their structure, chemistry, and composition.

Table 1: Description of instrumentation on board Cassini [25]

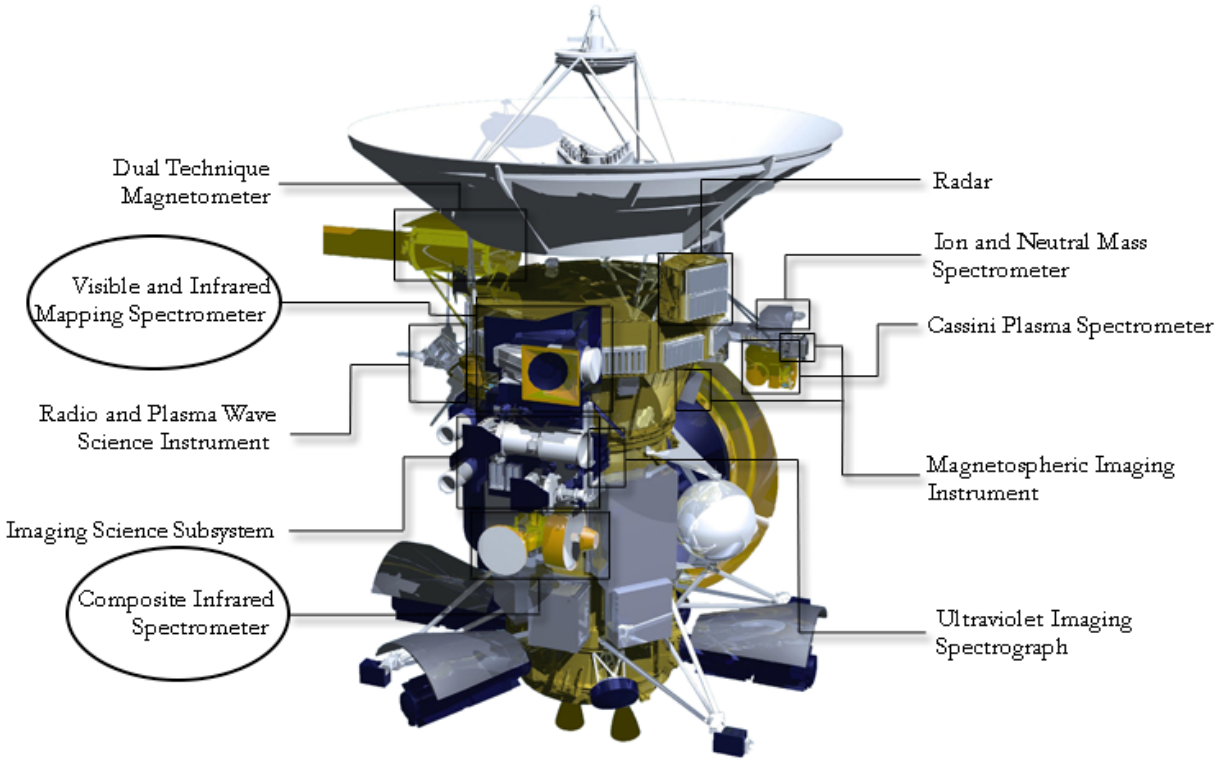

Figure 10: Instrumentation on board the Cassini Lander [25]

Once the images have been collected, the instrument collects all the light and splits it into specific wavelengths. Then, the amount of infrared energy at each wavelength can be plotted and conclusions about which material gives off that amount of infrared energy at that determined wavelength. Figure 11a shows how spectra from the VIMS instrument can look like. This spectrum is from the south polar region of Enceladus and absorption's at 1.04, 1.25, 1.5, and 2.0 micrometers indicate that almost pure water ice is present in that region on the surface of Enceladus [26]. The data from VIMS can be used to form mosaics of objects by color correcting where combined materials are found. This was used to form images such as the one in Figure 8 of Titan.

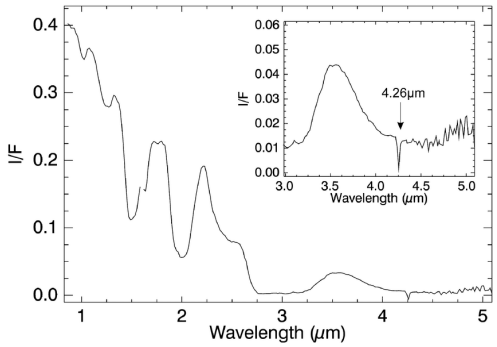

(a) VIMS spectrum of Enceladus' south polar region [26]

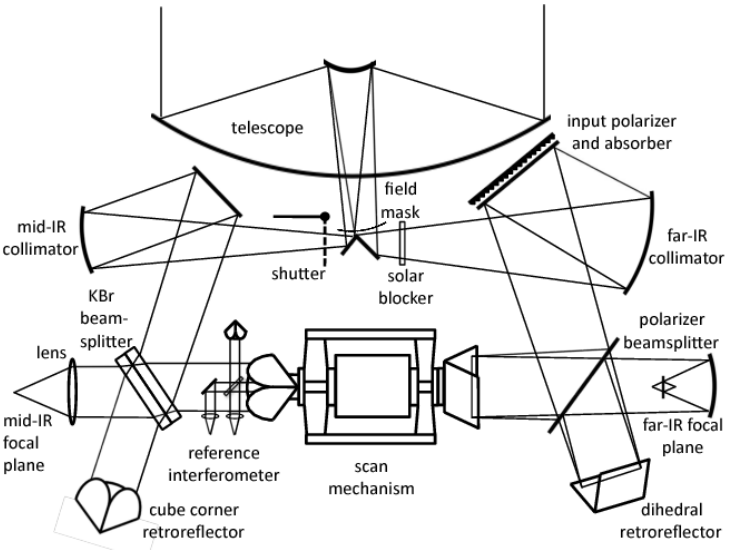

(b) CIRS Conceptual Design Layout [27]

Figure 11: Output data spectra from the VIMS instrument and the layout of how the CIRS instruments is assembled.

The CIRS consists of dual interferometers that measure IR emissions from the surfaces over wavelengths from 1400 to 10 cm^{-1} [28]. An interferometer is an instrument designed to make precise measurements of wavelengths within some range of the electromagnetic spectrum. The two interferometers mentioned above consist of a mid-IR (600 to 1500 cm^{-1}) and a far-IR (10 to 600 cm^{-1}) interferometer [28]. Both of these interferometers share a single Cassegrain telescope. Light from the primary mirror of the telescope passes to the secondary mirror above it and then reflects down the interior tube towards the focal plane to the telescope. At the focal plane behind the primary mirror of the telescope, the light is then divided by a roof-shaped mirror that directs the separated light toward both the infrared and far-infrared portions of the spectrometer [27]. This allows the entire spectrum to be sampled at one time. Figure 11b shows the overlay of the positioning of the components inside the CIRS.

3.2 Spectroscopy

3.2.1 Infrared Radiation

Infrared radiation is a form of electromagnetic radiation that has a wavelength longer than the wavelengths of visible light. Since it is not within the range of wavelengths capable of being seen by the human eye, infrared radiation is invisible to humans. Infrared wavelengths range from 700 nm to 1 mm. The electromagnetic scale shown in Figure 12 shows the range of the infrared radiation to the other forms of radiation-based off on the perspective wavelengths.

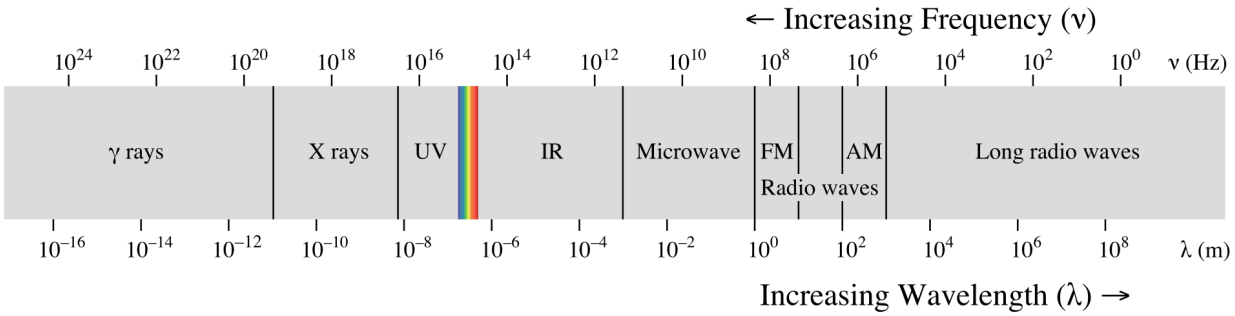

Figure 12: Electromagnetic radiation scale showing the relation of infrared radiation (IR) to the other wavelengths.

The energy created by each form of different electromagnetic radiation is related to the wavelength. The equation for the amount of energy each photon has is $E = hc/\lambda$ [29]. Where E is the energy of the photon, h is Planck's constant, c is the speed of light in vacuum, and λ is the wavelength of the photon. Interaction between matter and infrared radiation can be understood in terms of changes in the molecular structure associated with rotations and vibrations which give off energy. This energy level is unique for each molecule and is based on the specific structure of the molecule. The absorption of energy by a molecule occurs at its resonance frequency. These energies are affected by the shape of the molecule, the size of the atoms, and the vibronic coupling within the molecule. Vibronic coupling is the relationship between how much the bonds within the molecule move when there is a presence of energy [30]. Since these molecules either absorb or emit light at specific wavelengths, it is possible to measure the infrared radiation and determine the molecules present. This is the basis for infrared spectroscopy. Using the readings from infrared instrumentation it is possible to determine what materials emit or absorb radiation at specific wavelengths. This wavelength is the fingerprint of this molecule. When these trends are observed, it is possible to determine the composition of the material.

3.2.2 Molecular Vibration

Molecules have many different ways they can vibrate and each causes different bands in the spectra. Molecular vibrations occur in the near-infrared region [31]. A molecule can be looked at in terms of a system of masses (atoms) joined together by bonds that have spring-like qualities. The atoms can move in relation to each other by bending, stretching, or contracting. Figure 13 shows the different kinds of stretching and bending vibrations that occur during the absorption of radiation.

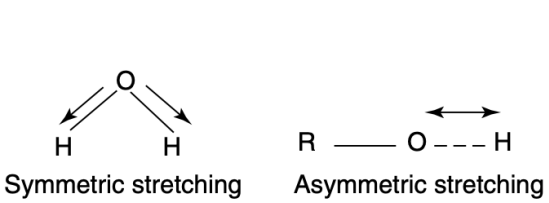

(a) Symmetric and asymmetric stretching vibrations [32].

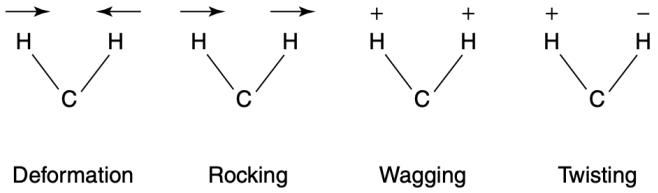

(b) Types of bending vibrations [32]. The plus symbol means the atom is bending out of the page, and the minus symbols measn the atom is bending into the page.

Figure 13: Different types of stretching and bending vibrations that can occur within particles.

Molecules containing N number of atoms will have $3N$ degrees of freedom [32]. The theoretical number of absorption bands a molecule has is limited to the number of degrees of freedom that molecule has. Another limiting factor for the number of bands a molecule can produce is the types of atoms the molecule is composed of. Each type of bond absorbs or emits at a determined wavelength. Therefore, it does not matter how many C-H bonds a molecule has since the molecule will absorb at the same wavelength. Consequently, there is no way to tell the number of C-H bonds a molecule has, only that C-H bonds are present [32].

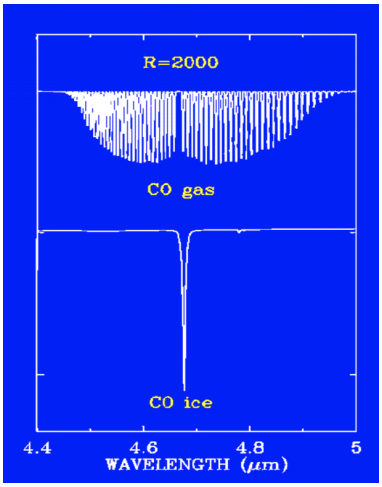

Figure 14: Change in wavelength due to phase of material [33]

Theoretically, the bands caused by these vibrations should be infinitely small and not be noticeable. Several factors play a role in broadening the bands. The first is the Doppler effect which changes the readings since the molecule is either moving towards or away from the instrument [34]. Collisions between the atoms will also cause the band to widen. Also, there is a relationship between the lifetime of the excited state of the molecule and the width of the absorption band [32]. Finally, the state of the molecule affects how the band will appear. There is a change in the band if the molecule is in the solid, liquid, or gaseous state. This is because, compared to the liquid and gaseous states, there is less movement of the atoms in a solid state. Figure 14 illustrates how this appears in the data when comparing CO gas versus CO ice.

4 Data Acquisition

4.1 Cassini Data

To obtain clear data through infrared spectroscopy, a lot has to be known about the spectra being studied. Laboratory experiments must be used to analyze and obtain quantitative results from infrared spectroscopy. Since Cassini observed the surface of Enceladus from space, the data acquired will not result in exact observations from VIMS. Using empirical methods in space, the data from the emitting surface molecules will include a mixture of different species. This means the observed ground composition will not be pure, and the data will also include noise from the surroundings. This noise could potentially obscure certain features or show features in locations where there should be an absence. For VIMS data, wavelengths longer than 3 μm are generally noisier than shorter wavelengths. This is due to an intrinsic low reflectance of the surface of Enceladus, and a lower instrumental sensitivity [11].

The data collected during this mission is archived by the Jet Propulsion Lab of NASA in the Planetary Data System collection. The raw data from Cassini can be found at `https://pds-imaging.jpl.nasa.gov/` and open for anyone to use [35]. The VIMS data is stored in this database as the raw data from the Cassini mission. The data needs to be calibrated to allow for specific parameters to be converted into readable values. During the calibration process, the data is split into two categories: the visible and infrared parts of the spectrum. Once this is complete, the digital count numbers for each pixel are converted into physical radiometric intensity (I/F) values which are used in this study. Lastly, the calibration filters out any random pixel noise within the data sets. Once this is complete, the different parameters of the data can be explored by using specific functions. This calibration has already been completed for all VIMS data from the Cassini mission by the team at the Laboratory of Planetology and Geodynamics (LPG) of Nantes University [36] [37]. The LPG VIMS data portal has previews of the VIMS images and the calibrated data from these specific data sets can be downloaded directly from the website. The downloaded data cubes can then be used to extract the spectra, coordinates on the surface of Enceladus, observation angles, and resolution for the desired locations. Each cube is an observation of the surface comprised of many pixels. The resolution of the pixel is the diagonal distance from one corner of the pixel to the opposite corner of the pixel. The center of each pixel, which determines the latitude and longitude, is the intersection point between two lines that connect the opposite corners of the pixel. To extract information from the downloaded cubes, a Jupyter notebook was published by LPG which explains how to extract specific information from the cubes [38]. A few examples of what can be extracted from the cubes are the incident, emergence, and phase angels, the pixel coordinate location on the surface of Enceladus, and the resolution of the image taken by Cassini. An example spectra can be seen below in Figure 15 from Cube 1711571239_1.

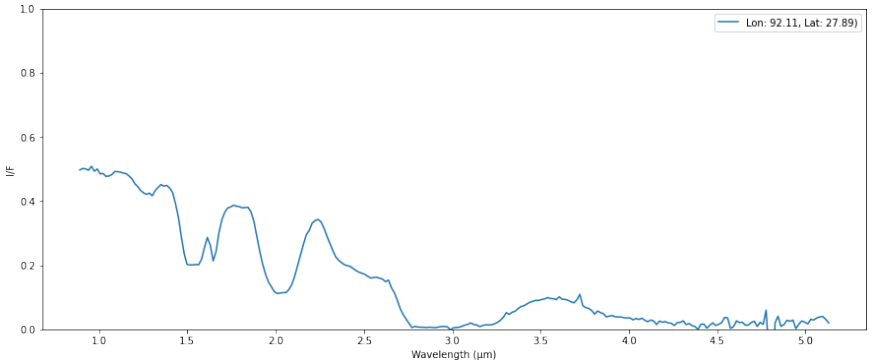

Figure 15: Example of the spectra that can be produced from the notebook described above. Cube 1711571239_1 is shown at the latitude and longitude reported in the inset on the top right corner.

4.2 Photometric Correction

The data that has been acquired in Section 4.1 from the Enceladus surface greatly depends on the angels at which the surface was observed. These different observation angles make it impossible to compare spectra taken at different incidence and emergence angles. To be able to compare and stack different spectra, a correction has to be made to the data to which factors out the viewing parameters. The photometric correction model used in this study was given by Robidel in the paper which studied the surface of Enceladus and created a mosaic to map the moon's surface [11]. The correction is composed of two parts, the disk function D and the phase function f, which includes the equigonal albedo A_{eq}. The equigonal albedo is the corrected data that will be used throughout the study. The correction can be seen below in Equation 1. In Equation 1, the $\frac{I}{F}$ is the uncorrected data that has been collected from the VIMS data in Section 4.1,g is the phase angle which is also collected in Section 4.1 and explained in Section 5.2, the disk function is calculated below, and the equation is rearranged to solve for f.

$$\frac{\mathrm{I}}{\mathrm{F}}(\mathrm{i},\mathrm{e},\mathrm{g},\lambda) = \mathrm{D}(\mathrm{i},\mathrm{e},\mathrm{g}) \times \mathrm{f}(\mathrm{g},\lambda) \tag{1}$$

The disk function describes the brightness distribution over the two-dimensional disk of Enceladus' surface. The disk function can be seen below in Equation 2 which takes into account the photometric longitude and latitude, γ and β respectively, which are defined in Equations 3 and 4 [39]. These photometric longitudes and latitudes relate the incidence, emergence, and phase angles to the corrected model. The relation between the observation angles from the surface of Enceladus and the photometric latitude and longitude can be seen in Figure 16.

$$D(i,e,g) = D(\beta,\gamma,g) = \cos\left(\frac{g}{2}\right)\cos\left[\frac{\pi}{\pi-g}\left(\gamma-\frac{g}{2}\right)\right]\frac{(\cos\beta)^{\frac{g}{\pi-g}}}{\cos\gamma} \tag{2}$$

$$\gamma = \arctan\left(\frac{\cos(i)-\cos(e)\cos(g)}{\cos(e)\sin(g)}\right) \tag{3}$$

$$\beta = \arccos\left(\frac{\cos(e)}{\cos(\gamma)}\right) \tag{4}$$

The phase function can be calculated by performing a linear fit, shown in Equation 5, to the observed data corrected for the disk function [39]. The equigonal albedo is equal to the phase function when the phase angle is equal to zero; therefore, the equigonal albedo is equal to a in Equation 5.

$$\frac{\frac{I}{F}(\lambda)}{D} = \mathrm{f}(\mathrm{g},\lambda) = a + bg \tag{5}$$

The linear fit can be done by observing a plot of the phase function (g) versus $\frac{\frac{I}{F}(\lambda)}{D}$ at a specific wavelength. An example of this plot can be seen in Figure 71a at 1.80μm which has a linear fit to the data of $f(g,\lambda) = 0.698 - 0.25 * g$. This shows that at 1.80μm there is an a value of 0.698 and a b value of -0.25. In Robidel et al. (2020), a test of 8 wavelengths showed there was a correlation between a and b and you could approximate the value for b in relation to a. Figure 17b shows the relation between the values for a and b. This relation was done for the entire data set at 8 wavelengths on Enceladus for $(i,e) < 80°$ and $g < 130°$ [11].

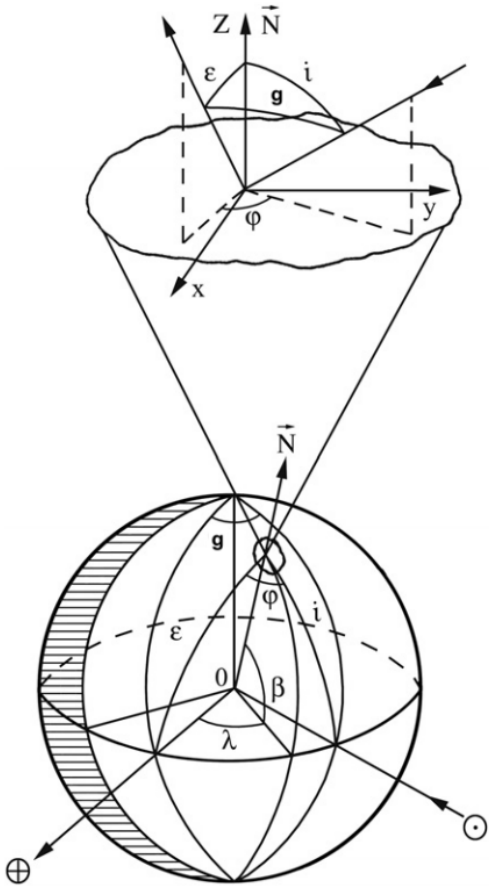

Figure 16: Relation between the incidence (i), emergence (ε), and phase (g) angles to the photometric latitude (β) and longitude (γ) angels. [40]

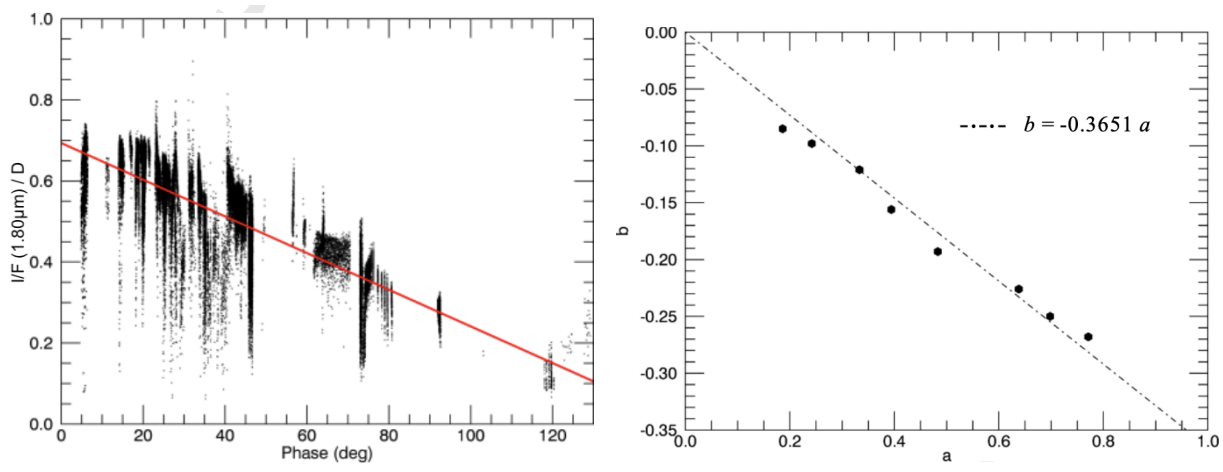

(a) Relation to the phase angle and $\frac{I}{F}\frac{(\lambda)}{D}$ at 1.80μm from many data sets from VIMS performed by Robidel et al. (2020).

(b) Correlation between a and b for 8 different wavelengths on Enceladus's surface performed by Robidel et al. (2020).

Figure 17: Process to compute the linear fit to the phase function. [11]

Equation 1 can be updated using the data found by Robidel et al. in Figure 17b, and shown below in Equation 6. This equation takes this relation between a and b into account.

$$\frac{\mathrm{I}}{\mathrm{F}} = \left[\cos\left(\frac{g}{2}\right)\cos\left[\frac{\pi}{\pi-g}\left(\gamma-\frac{g}{2}\right)\right]\frac{(\cos\beta)\frac{g}{\pi-g}}{\cos g}\right]\times[\mathrm{a}\times(1-0.37g)] \tag{6}$$

Using Equation 6 to solve for a you can find the equigonal albedo A_{eq}. The equigonal albedo is the albedo of the surface at a phase angle of zero. The equigonal albedo allows for comparison and stacking of data sets that have been taken under different viewing angles. Figure 71 shows how the spectra change after the photometric correction has been applied. The two spectra are from different data cubes which have viewed the surface of Enceladus at similar locations on the surface but with different viewing angles. The spectra should not differ much in the intensity of the spectra since they are not located that far apart. The lower $\frac{I}{F}$ values at the edges of the cubes are due to the high observation angles which make the region appear to be reflecting less light. The correction scales each spectra to the equivalent of viewing each location with a phase angle (g) of 0°. When observing each location at the same phase angle, the two spectra are more similar when comparing the equigonal albedo. This correction allows the comparison and stacking of different data sets independently of the illumination and viewing observation conditions.

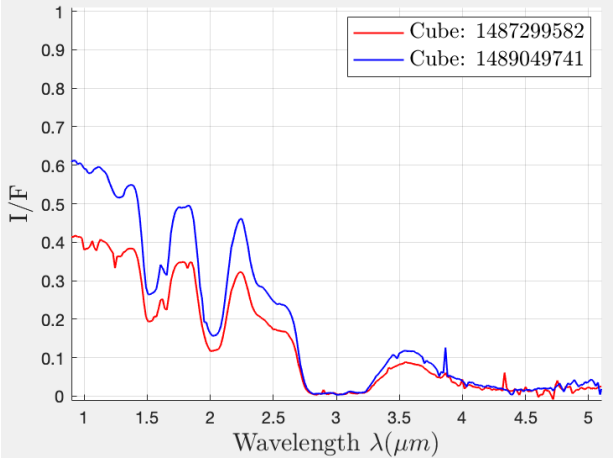

(a) Plot $\frac{I}{F}$ vs. wavelength for the two data cubes using VIMS data.

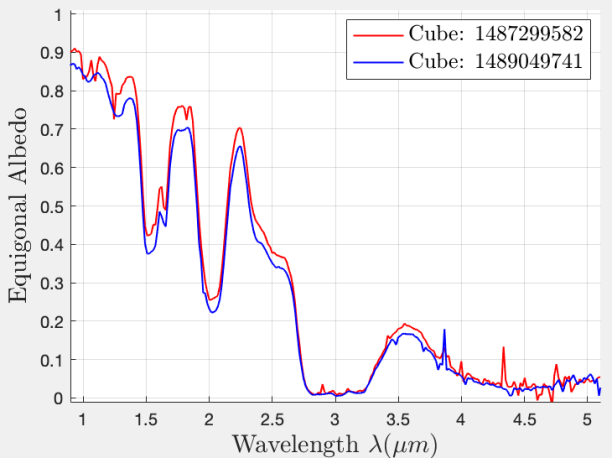

(b) Plot of the equigonal albedo vs. the wavelength for the two data cubes.

Figure 18: The red spectrum corresponds to cube 1487299582_1 located at 20.92°N, 85.74°E ($i = 71°$, $e = 48°$, and $g = 26°$). The blue spectrum corresponds to cube 1489049741_1 located at 24.81°N, 86.80°E ($i = 51°$, $e = 65°$, and $g = 45°$).

This correction can be made for the entire cube to make the two cubes more uniform when comparing them in a mosaic. Figure 19 shows the two cubes before and after the correction has been made. It can be seen that the corrected image appears to be more congruent at the edges of the two cubes. The pixels on the joining edges of the two cubes in Figure 19a have a much greater contrast compared to the joining edges in Figure 19b.

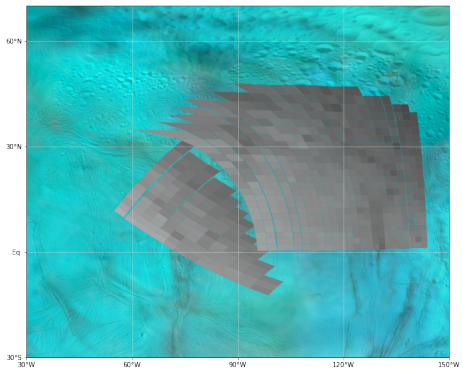

(a) Plot of the two cubes $\frac{I}{F}$ overlaid on the surface mosaic of Enceladus.

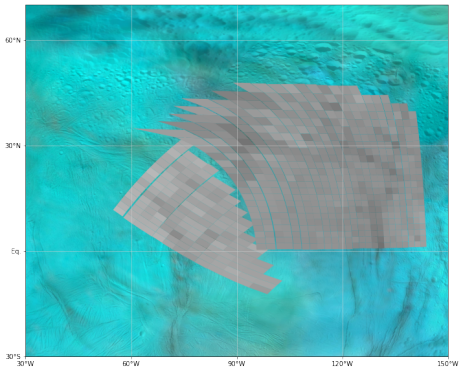

(b) Plot of the two cubes equigonal albedo after the photometric correction has been made overlaid on the surface mosaic of Enceladus.

Figure 19: The two cubes 1487299582_1 and 1489049741_1 overlaid the surface mosaic of Enceladus. The darker regions correspond to a lower value, and the lighter regions correspond to higher values.

4.3 Red Region Data

The first region that will be investigated is the red region. This region is centered at 30°N and 90°W. As mentioned in Section 4.1, the data from the Cassini data base is located within cubes. Each cube is an observation of the surface comprised of many pixels. The resolution of the pixel is the diagonal distance from one corner of the pixel to the opposite corner of the pixel. The center of each pixel,

which determines the latitude and longitude, is the intersection point between two lines that connect the opposite corners of the pixel. 35 pixels with centers closest to this location have been selected. Figure 20a shows each of the 35 pixels overlaying on top of one another. The number of pixels that cover a certain coordinate is shown in this figure. The brighter the location, the more pixels that cover the coordinate. Figure 20b shows the 35 spectra that were obtained from these pixels. Each spectra has been photometrically corrected to compare each pixel. Table 2 shows the specified cube number, latitude, and longitude of the center of each pixel, and the resolution for each pixel.

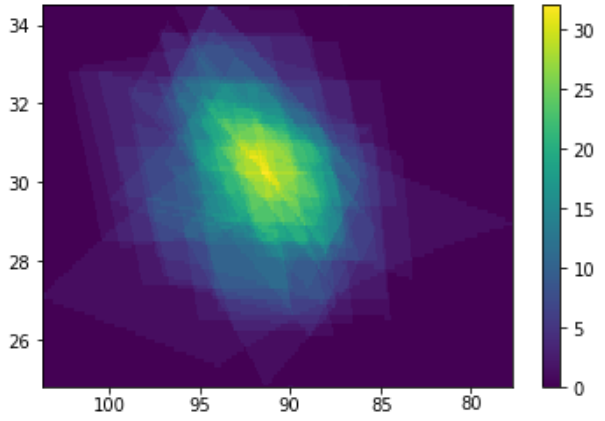

(a) The number of times a location is found in the pixel in the red zone. The x-axis is the longitude west, and the y-axis is the latitude north.

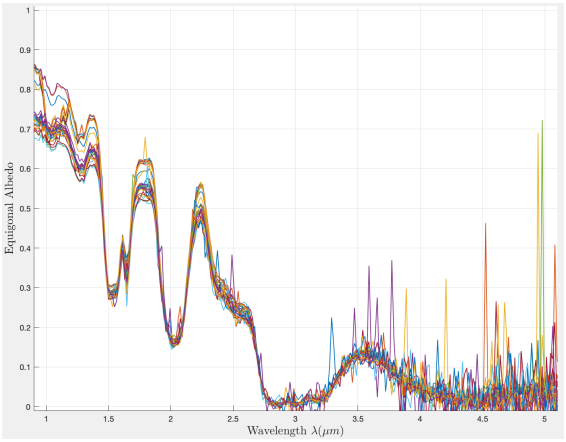

(b) All 35 spectra used to analyze the red region. These spectra have been photometrically corrected.

Figure 20: Figures from Section 4 used to show the size of the pixel used to gather the information from and the different spectra laid on top of one another.

Cube Number	Latitude ($°N$)	Longitude ($°W$)	Resolution (km/pixel)
1652861972_1	27.7842	90.1785	17.6119
1652863281_1	29.4246	87.6200	15.5867
1652862525_1	31.0620	89.6095	19.6106
1652863825_1	30.9417	86.7855	16.8464
1652864797_1	29.0261	93.1663	19.1904
1652865660_1	28.2974	89.8765	21.0959
1652866327_1	30.4942	94.7752	22.6280
1652866994_1	28.7502	88.2614	24.1228
1652867101_1	29.1694	88.5208	24.3640
1652867208_1	30.9219	93.8718	24.6068
1671593633_1	28.3131	92.0751	18.5440
1671591682_1	30.3988	92.6336	12.3925
1713112152_1	30.7380	91.7064	15.3723
1713112124_1	31.3154	89.5287	15.2939
1713112097_1	30.6357	89.5142	15.2172
1713112069_1	30.3109	90.5133	15.1416
1713112041_1	29.0770	90.2515	15.0644
1713112013_1	30.0504	88.4431	14.9867
1711570890_1	30.3650	89.7992	9.8257
1711571239_1	27.8907	92.1073	10.5971
1711571397_1	28.1393	92.3492	11.0609
1711573513_1	30.1343	91.6791	16.7582
1711573639_1	30.5233	92.9858	16.9960
1711573746_1	29.6571	86.4315	17.3834
1711573910_1	31.4437	89.6941	17.8707
1711574088_1	29.0787	91.3103	18.3656
1696174814_1	29.6607	88.3474	12.9196
1696174951_1	30.7256	91.1983	13.4405
1696174985_1	27.8759	89.9676	13.5659
1696175058_1	32.4066	89.8922	14.2026
1696176807_1	30.9967	90.6063	14.7198
1696178116_1	31.8647	89.7107	18.2174
1696174917_1	30.6479	90.6180	13.3105
1696174882_1	30.1635	89.5058	13.1795
1696174848_1	30.0679	88.8444	13.0495

Table 2: Cubes used for the red region. Latitude and longitude of the center of the pixel within the cube that was used are given as well as the resolution of each pixel. The average latitude is $29.9040°N$, the average longitude is $90.2702°W$, and the average resolution is 16.5060 km/pixel.

4.4 Crater Region Data

The second region that will be investigated is the crater region. This region is located at $45°N$ and $160°E$. As mentioned in Section 4.1, the data from the Cassini database is located within the pixels of data cubes. 14 pixels with centers closest to this location have been selected. Figure 21a shows each of the 14 pixels and the surface area they cover. The color of each point corresponds to the color of the box, which represents the pixel. Pixels with the same dot represent pixels that are from the same cube. Figure 21b shows each of the 14 pixels overlaying on top of one another. In this figure, the pixels from the same cube can not be distinguished because they are aligned perfectly and do not overlap. There are small dots noticeable in Figure 21b which are from how the pixels overlap

were counted for the pixels from the same cube. These dots should not be regarded since there is no overlapping taking place in this location. The number of pixels that cover a certain coordinate is shown in this figure. The brighter the location, the more pixels that cover the coordinate. Figure 53b shows the 14 spectra that were obtained from these pixels. Each spectra has been photometrically corrected to compare each pixel. Table 3 shows the specified cube number, latitude, and longitude of the center of each pixel and the resolution for each pixel.

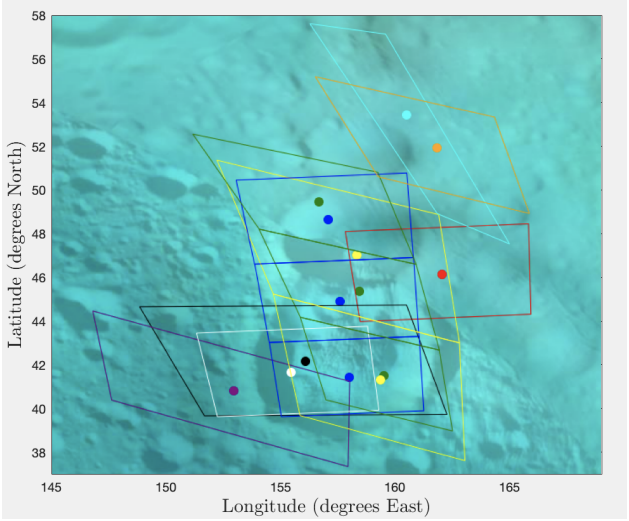

(a) Map of each of the 14 pixels used in the crater region. Each dot represents the location of the center of the pixel and each line represents the outline of the pixel. The color of each dot correlates to the color of the outline of the pixel. Dots with the same color represent pixels from the same flyby.

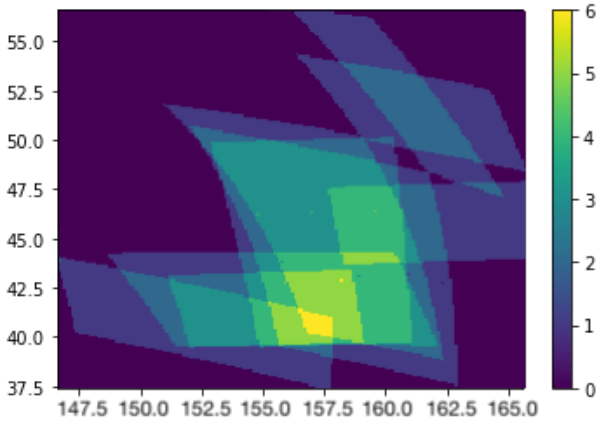

(b) The number of times a location is found in the pixel in the crater region. The x-axis is the longitude, and the y-axis is the latitude.

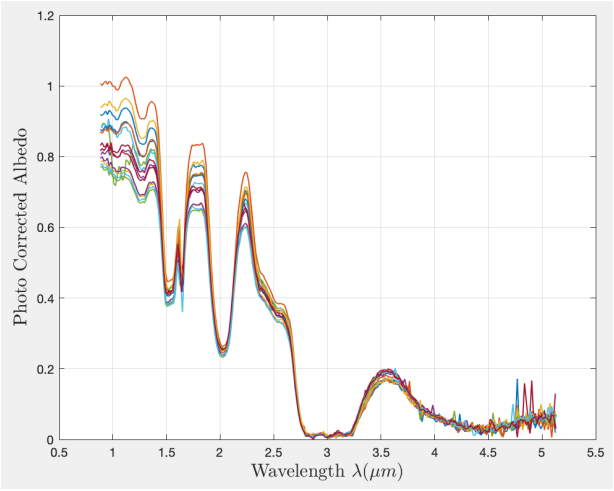

(c) The spectra from the 14 pixels used to find the surface parameters in the crater region.

Figure 21: Shows the location, size, and spectra for each of the 14 pixels used in the crater region.

Cube Number	Latitude (°N)	Longitude (°W)	Resolution (km/pixel)
1489044917_1	45.7266	-162.0318	16.7413
1489045685_1	44.5451	-157.5841	14.8997
1671591682_1	44.9698	-158.4245	12.7219
1671593633_1	46.5441	-158.3172	18.6130
1823506949_1	41.9053	-156.0746	22.6040
1858923675_1	52.6590	-160.4973	9.0248
1671596173_1	40.6193	-152.9635	19.2960
1489044917_1	41.4297	-155.4651	16.7553
1489045685_1	41.2167	-157.9874	14.8963
1489045685_1	48.0872	-161.8153	14.9036
1671591682_1	41.2981	-159.4911	12.7170
1671591682_1	48.8941	-156.6920	12.7279
1671591682_1	51.2379	-161.8153	12.7118
1671593633_1	41.1036	-159.3614	18.6056

Table 3: Cubes used for the crater region. Latitude and longitude of the center of the pixel within the cube that was used are given as well as the resolution of each pixel.

Cube Number	Latitude (°N)	Longitude (°W)	Resolution (km/pixel)
1637466116_1	-66.3310	39.2947	8.0839
1660433230_1	-70.4506	20.0767	1.8730
1660433375_1	-75.0206	30.8684	2.1257
1660433230_1	-70.9262	23.6929	1.8944
1637463583_1	-72.8865	35.6658	1.2576
1637463803_1	-71.0266	37.0960	1.8322
1500059046_1	-60.8580	-85.9883	18.9301
1637463583_1	-67.7972	40.3172	1.3317
1637463583_1	-67.7961	39.0422	1.3142
1637463583_1	-66.2519	36.7818	1.2919
1637463583_1	-71.1704	36.3166	1.2707
1637463583_1	-68.2234	32.5235	1.2321
1637463688_1	-73.9940	31.4050	1.6882
1604167764_1	-66.5456	24.1533	5.7924

Table 4: Cubes used for the tiger stripes region. Latitude and longitude of the center of the pixel within the cube that was used are given as well as the resolution of each pixel.

4.5 Tiger Stripes Region Data

The last region that will be investigated is the tiger stripes region. This region is located at the southern pole of Enceladus. As mentioned in Section 4.1, the data from the Cassini database is located within the pixels of data cubes. 14 pixels with centers closest to this location have been selected. Figure 22a shows each of the 14 pixels and the surface area they cover. The color of each point corresponds to the color of the box, which represents the pixel. Pixels with the same dot represent pixels that are from the same cube. Figure 22b shows each of the 14 pixels overlaying on top of one another. In this figure, the pixels from the same cube can not be distinguished because they are aligned perfectly and do not overlap. The number of pixels that cover a certain coordinate is shown in this figure. The brighter the location, the more pixels that cover the coordinate. Figure 22c shows the 14 spectra that were obtained from these pixels. Each spectra has been photometrically

corrected to compare each pixel. Table 4 shows the specified cube number, latitude, and longitude of the center of each pixel and the resolution for each pixel.

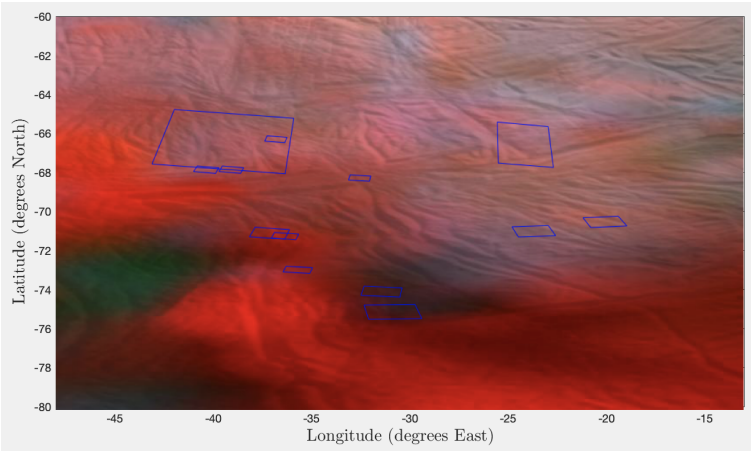

(a) Map of each of the 14 pixels used in the tiger stripes region. The amount of surface each pixel covers is represented by the blue outlines.

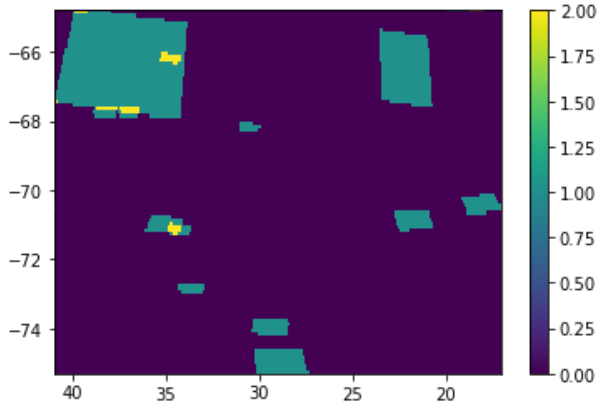

(b) The number of times a location is found in the pixel in the tiger stripes. The x-axis is the longitude, and the y-axis is the latitude.

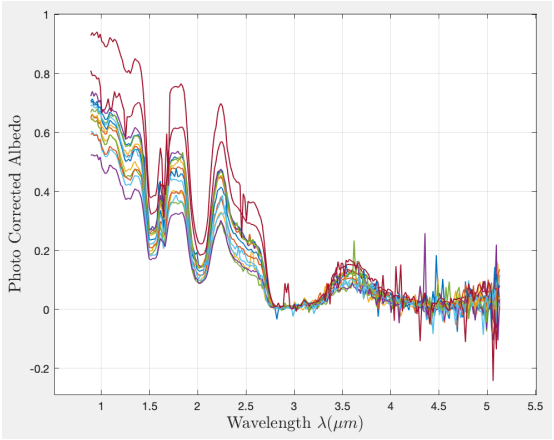

(c) The spectra from the 14 pixels used to find the surface parameters in the tiger stripes region.

Figure 22: Shows the location, size, and spectra for each of the 14 pixels used in the crater region.

4.5.1 1 μ*m* Dip

A repeating feature in cubes located in each region is a notable dip occurring at the lower μ*m* wavelengths. Table 5 shows the cube from where the pixel is found and the latitude, longitude, and resolution of the pixel. There is not a trend based on the location of the pixel which would identify a solution as to why this dip has occurred. A few of the cubes used above in Table 2 are located ckose to cubes located in Table 5 and the dip does not appear in the spectra. The dip found in these 12 cubes is due to the collection of the raw data that VIMS acquired. The raw data is measured in data numbers (DN). The DN value is the number of counts that the detector measures. If the DN value is too high, then the response becomes saturated and is no longer usable. If the DN value is above 3500 counts, then the data becomes saturated and this dip in the reading occurs around the 1 μ*m* range [41]. This affects the spectra in this region and the spectra are not usable. Figure 23 shows the values of DN for spectra which is saturated and spectra that are not saturated. All the

spectra with this feature can be seen below in Figure 24. In the legend, the number from 1 to 12 correlates to the order of the cubes in Table 5. Since the data from these 12 cubes are all saturated, they will not be used in this study.

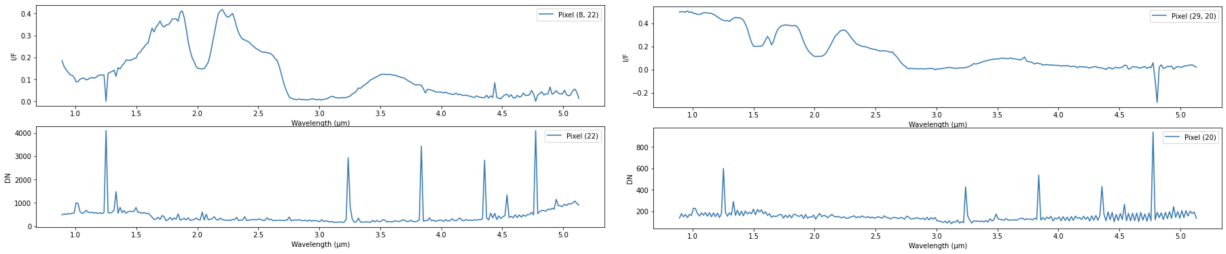

(a) Cube 1652861016_1 which has a peak DN value of 4095 in the lower wavelength region. This spectra has a DN count that is much too high to be used since the spectra is saturated.

(b) Cube 1711571239_1 which has a peak DN value of 938 in the higher wavelength region. This spectra has a much lower DN count that the spectra in 23a

Figure 23: Comparison between cube 1652861016_1 which is saturated which has a dip at 1 micron and cube 1711571239_1 which is not saturated that does not have a dip at 1 micron.

Spectra Number	Cube Number	Latitude ($°N$)	Longitude ($°W$)	Resolution (km/pixel)
1	1652861016_1	28.4466	88.1662	16.0948
2	1652862043_1	29.5492	90.5978	13.2422
3	1652862697_1	27.3019	90.5886	20.2290
4	1652862882_1	27.9019	92.2626	20.7708
5	1652863391_1	31.1787	91.1153	16.3049
6	1652863936_1	30.4770	90.9042	18.2001
7	1652864960_1	30.6458	88.3468	20.2916
8	1652859747_1	30.1669	90.3471	7.3178
9	1637468159_1	29.9927	90.5342	21.1355
10	1637466388_1	30.3153	91.4547	14.8038
11	1696175280_1	31.7205	88.2542	15.4222
12	1702362997_1	29.4369	87.7490	18.8295

Table 5: Cubes with the 1 micron feature that dips. Separated from the rest of the cubes to show the change it makes to the averaged feature. Cubes used for stacking. Latitude and longitude of the center of the pixel within the cube that was used are given as well as the resolution of each pixel.

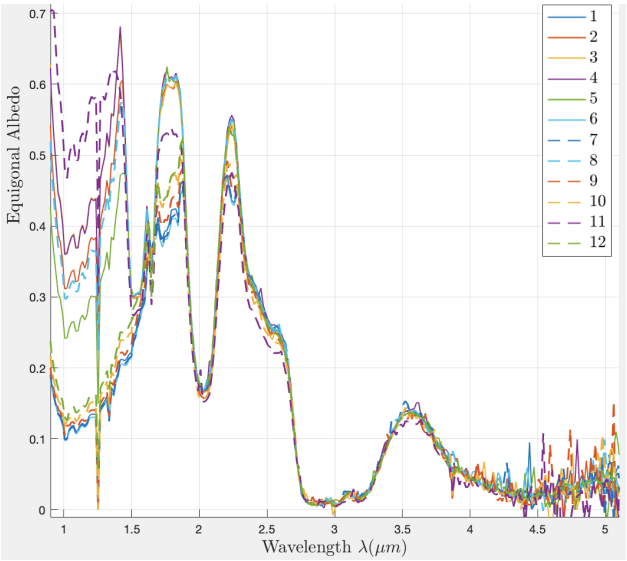

Figure 24: Spectra including the 1 micron dip feature.

4.6 Laboratory Data

After the Cassini data from each region is corrected, the data can be compared to spectra reproduced using data for water ice that has been observed in a laboratory setting using a reflectance model. Data from Enceladus can be benchmarked by models based on laboratory data, such that characteristics of the Enceladian surface can be retrieved, such as the grain diameter, porosity, surface roughness, crystallinity, and surface temperature. This section details which laboratory data is used in our models so that laboratory spectra and Enceladus spectra can be compared.

4.6.1 Mastrapa data

The majority of the laboratory data that will be compared to the data found from the Cassini mission is taken from the paper from Mastrapa in 2009, where the optical constants of amorphous and crystalline water ice are found for the wavelength 1.5 to 22 μm [42] [43]. This wavelength region is the location of the main absorption bands of water ice and is used to compare spectra from objects in our solar system. The main bands which determine the temperature or phase of the water ice are located near 3μm for the phase of the ice, 4.5μm which is a combination mode of molecular and lattice vibrations, 6μm which are all molecular vibrations, and near the 12μm which are all lattice vibrations [43]. The absorption bands of water found within the range taken by Cassini are 1.04, 1.25, 1.5, 1.65, 2.0, and 3.1 μm. Figure 25 below shows the spectra, wavelength, and shape of each of these absorption bands using the optical constants for crystalline ice. The data has been made public and the files for each of the optical constants are available to download at `https://iopscience.iop.org/article/10.1088/0004-637X/701/2/1347#references`. The constants have been found for amorphous and crystalline ice samples. The samples are deposited at 150K and then cooled to the desired temperature [42]. Once the sample was cooled to the desired temperature it was left to stabilize at the temperature for 5 minutes. From here, the optical constants are derived from the measurements taken. The n values, the real part of the index of refraction, and the k values, imaginary part of the index of refraction, can be seen for all crystalline and amorphous water ice temperatures below in Figures 26 and 27. The imaginary part of the refractive index

explains the absorption features of the material. If the observed material is transparent, k will be zero. The wavelength region of interest will be minimized to the same wavelength region that the Cassini data is measured in.

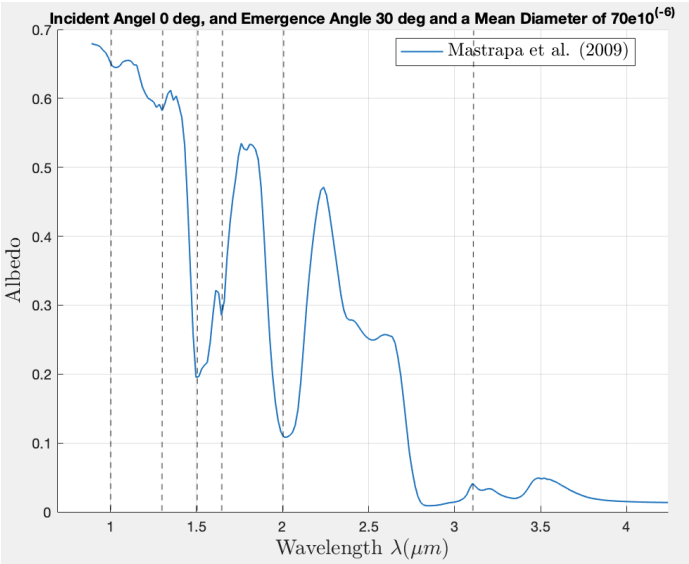

(a) Showing which wavelength absorption's are found in water.

Figure 25: Spectra of water ice to show which wavelength absorption's are common in water ice.

After the optical constants have been found, it is possible to include them through the Hapke model of reflectance, which will be discussed in Section 5, to output the reflectance for each temperature. Figure 28a shows the different reflectance spectra for the different temperatures of the crystalline ice and Figure 28b shows the spectra for all the amorphous ice for the different temperatures reported in the inset of the figures. The ice features have a slight dependence on temperature which causes the reflectance to increase as you increase the temperature of the ice [42]. Also, the 3.6 μm peak change to larger wavelengths as the temperature increases for crystalline ice which can be seen in Figure 28a [13]. This occurs because at the 3.6 μm the imaginary index changes with temperature. Figures 30 and 29 focus on this region and makes the shift in wavelength more visible. These peaks occur for crystalline ice at 3.37689, 3.37689, 3.38682, 3.39459, 3.41697, 3.44194, 3.45572, 3.46844, 3.48477, 3.50244, 3.50599, 3.52387, and 3.54558 in order of temperature. This trend is found in crystalline ice and not in amorphous ice. Figure 31 plots the peak value versus the temperature. This figure shows how the relationship between each parameter is a linear trend.

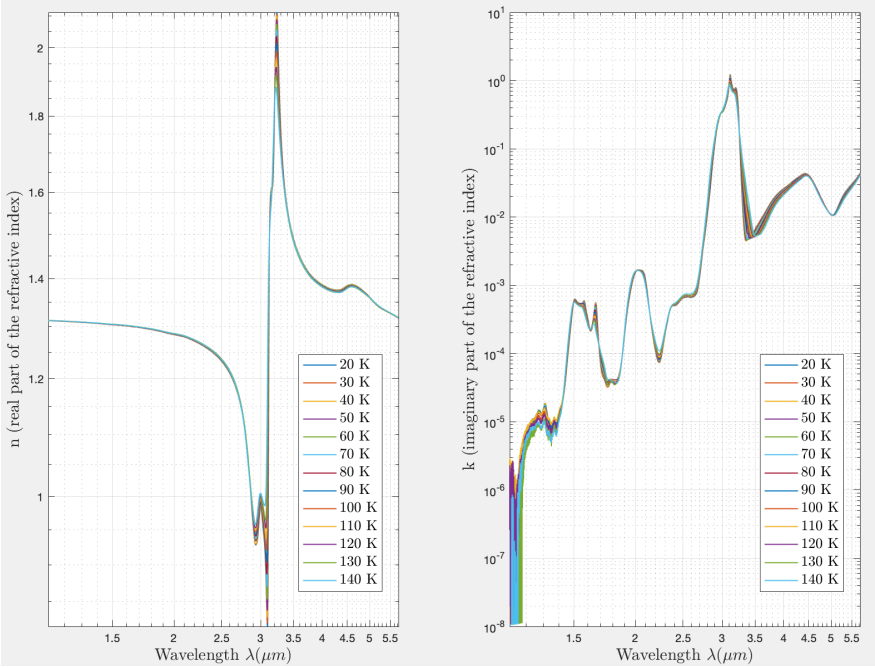

Figure 26: The real and imaginary parts of refraction collected from Mastrapa (2009) for crystalline water ice ranging from temperatures from 20 Kelvin to 140 Kelvin [43].

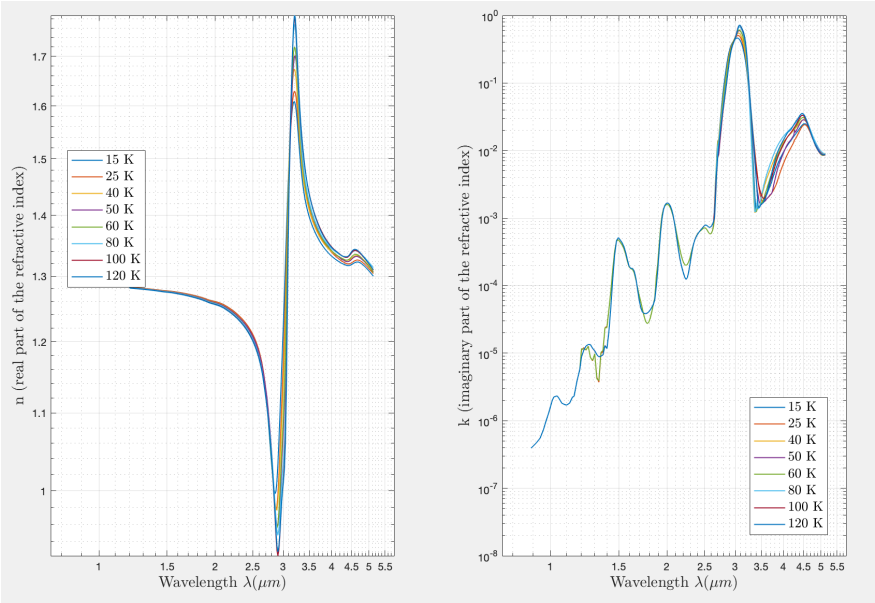

Figure 27: The real and imaginary parts of refraction collected from Mastrapa (2009) for amorphous water ice ranging from temperatures from 20 Kelvin to 140 Kelvin [43].

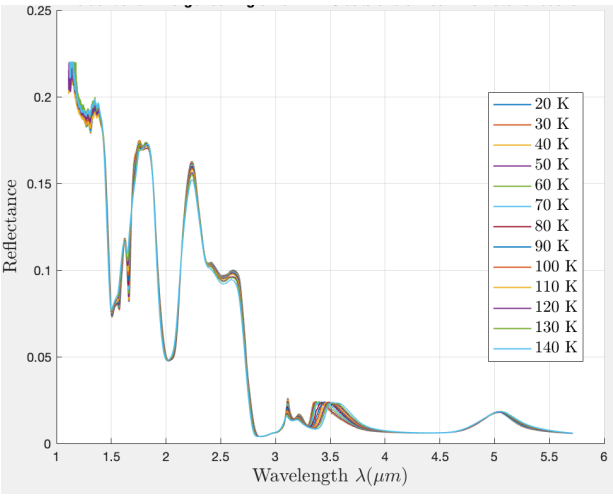

(a) The reflectance spectra determined from the Hapke model using Mastrapa (2009) for water crystalline ice ranging from temperatures from 20 Kelvin to 140 Kelvin [43].

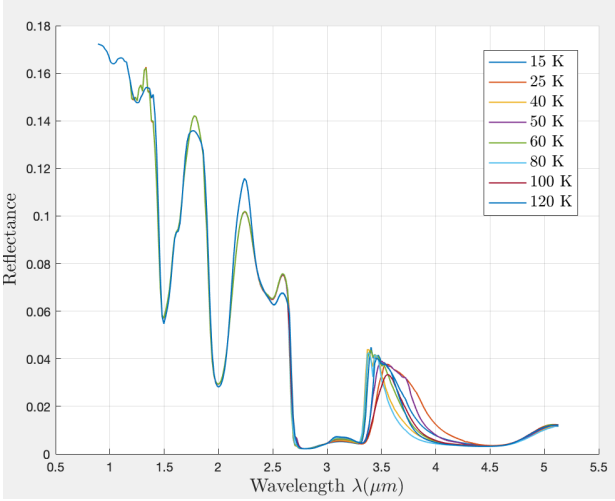

(b) The reflectance spectra determined from the Hapke model using Mastrapa (2009) for water amorphous ice ranging from temperatures from 20 Kelvin to 120 Kelvin [43].

Figure 28: Reflectance spectra of laboratory data from Mastrapa (2009) data.

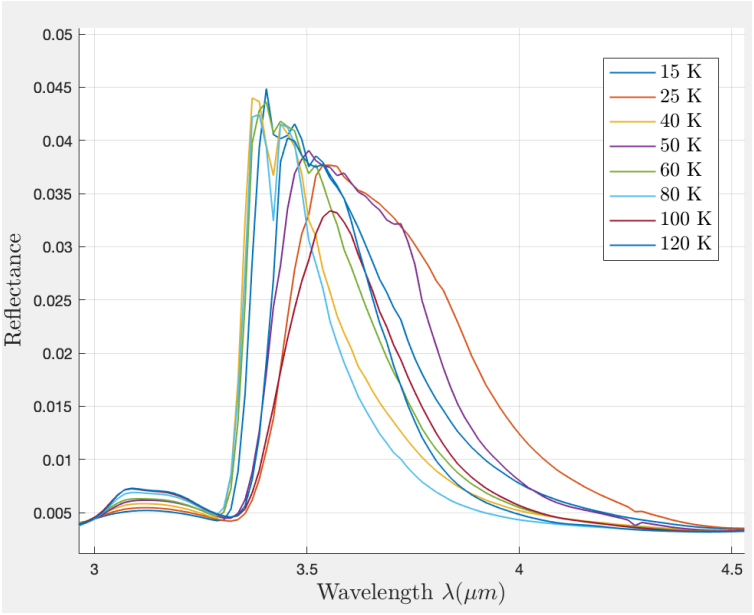

Figure 29: Zoom of Figure 28b highlighting the changes of the 3.6μm with respect to temperature [43].

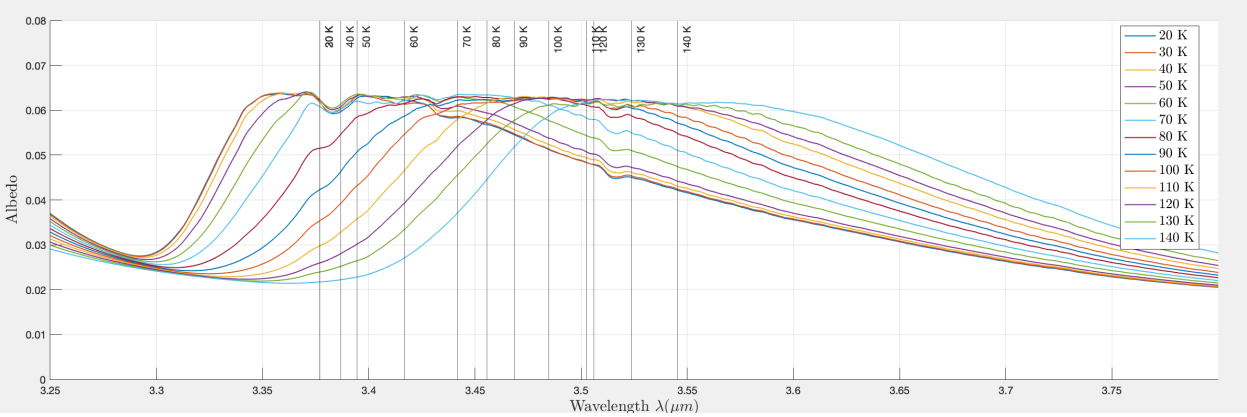

Figure 30: Zoom of Figure 28a highlighting the changes of the 3.6μ*m* with respect to temperature [43]. The peaks occur at the vertical lines and the temperature is given at the top of each vertical line.

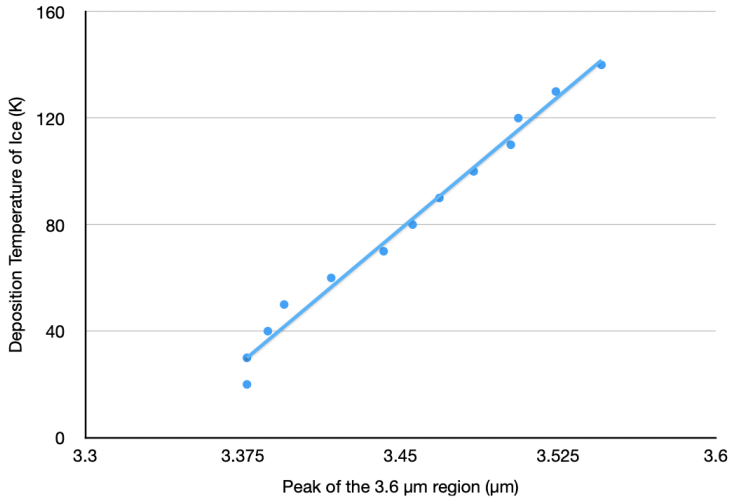

Figure 31: Shows the trend of peak positions around 3.6 μ*m* of Figure 30. This trend is a linear increase as the deposition temperature increases.

4.6.2 Clark Correction

The water ice constants that were published in 2009 by Mastrapa characterized the dependence on the temperature at the 3.6 μ*m* peak. The relation between peak location and temperature that was found was correct; however, the optical constants that were found in this region were incorrect. A study done by Clark et al. in 2012 found that the ice optical constants did not produce a match to observed laboratory reflectance data in the 3.2 to 5 μ*m* range [44]. The optical constants for the rest of the wavelengths were exceptionally fit and able to be used, only the constants found within this region were unusable. The study in Clark et al. (2012) took the laboratory data in this problematic region and inverted the Hapke model to match the Mastrapa coefficients at other wavelengths to find the correct absorption coefficients [44]. The same trend was found for the different temperatures, but the peaks were found at higher wavelengths. Figure 32a below shows the peaks for seven temperatures around the 3.6 μ*m* region. Figure 32b shows the trend of the peak at 3.6 μ*m* as the deposition temperature increases. From this linear trend that is seen in Figure 32b, the deposition

temperature can be extrapolated using Equation 7. This equation was found by fitting the data where X is the 3.6 μm peak of the spectra and Y is the deposition temperature of the ice.

$$Y = 819.95 * X - 2846.1 \tag{7}$$

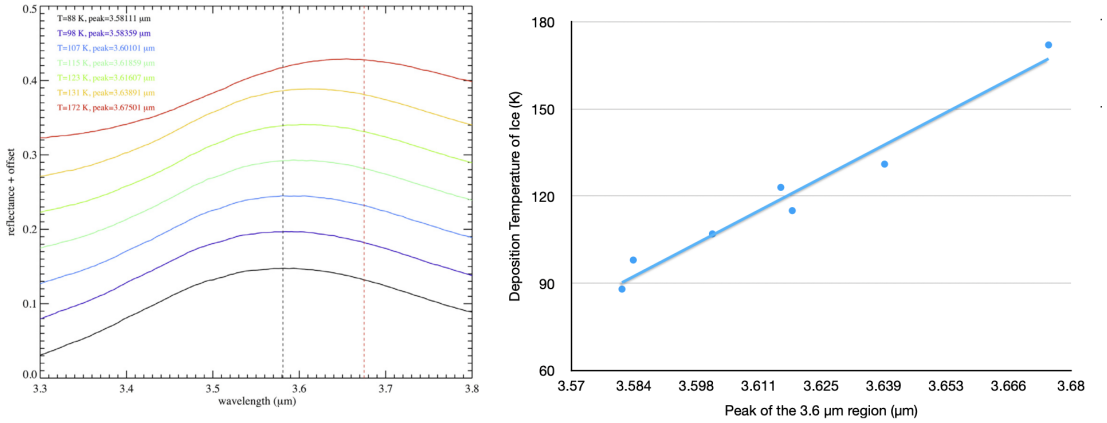

(a) Plot showing the 3.6 μm peaks for crystalline water ice using the corrected absorption coefficients found by Clark et al. (2012) [44][13].

(b) Relationship between the deposition temperature of the crystalline ice and the wavelength at the 3.6 μm peak.

Figure 32: Corrected relationship between the deposition temperature and the wavelength at the 3.6 μm peak.

4.6.3 Warren data

Another data set of the refractive indices of water ice is found in the study completed by Warren in 1984 [45]. This study was only conducted at one temperature and only for crystalline ice. Figure 33 shows the real and imaginary refractive indices n and k. The ice was formed at a temperature of $-7°C$ and left to stabilize before the measurements were taken [45]. This data was collected to compare results found by other studies to validate the Hapke model.

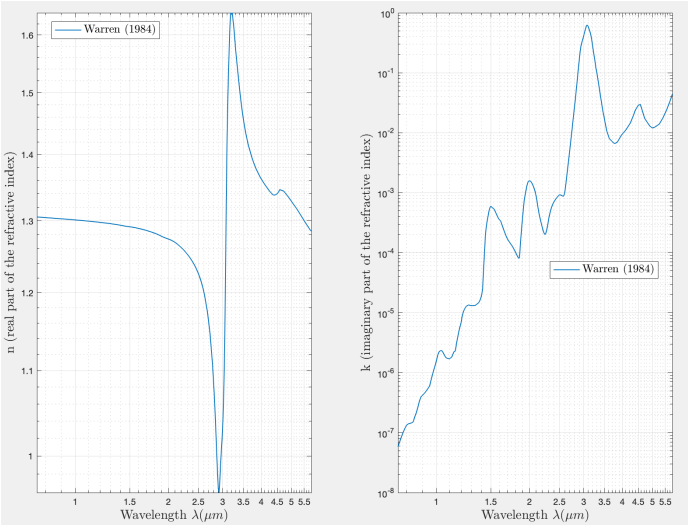

Figure 33: The real and imaginary parts of refraction collected from Warren (1984) for water crystalline ice at $-7°C$ [45].

5 Hapke Model

Hapke's reflectance model was formulated in 1993 by Bruce Hapke. There were updates in the model that were made in 2002, 2008, and 2012. This section will go into some of the parameters in his model and how they relate to the data acquired by the VIMS on Cassini. In this section, there will be a parameter study for the input variables which are fed into the Hapke model. Each parameter will be able to help explain the presence, abundance, and size of the particles found from the VIMS instrument. When given spectra from VIMS it is possible to work with this information to help better explain how the surface of Enceladus is comprised.

5.1 Reflectance and Reflectance Factor, r and $REFF$

The bidirectional reflectance r is the ratio of the scattered radiance to the incident irradiance. If we make the radiance I in $(Wm^{-2}sr^{-1})$ and the irradiance J in (Wm^{-2}) and $\mu_0 = cos(i)$ (where i is the incidence angle explained in Section 5.2), then Equation 8 below is how to obtain the reflectance. The equation is multiplied by μ_0 to only account for the irradiance that is normalized to the surface.

$$r = \frac{I \cdot \mu_0}{J} \tag{8}$$

The reflectance factor REFF is a dimensionless factor of reflectance which is the ratio of the reflectance of a surface to that of a perfect Lambertian surface which is illuminated at an incident angle i. The geometries of observing each surface should be identical. The REFF is related to the bidirectional reflectance by:

$$\text{REFF} = \frac{\pi \cdot r}{\mu_0} \tag{9}$$

The radiance factor is known as $\frac{I}{F}$. The difference between $\frac{I}{F}$ and REFF is that $\frac{I}{F}$ compares the reflectance to a Lambertian surface that is illuminated under an incidence of 0 degrees. The makes $\mu_0 = cos(i) = 1$, and the equation for $\frac{I}{F}$ is shown below in Equation 10.

$$\frac{\text{I}}{\text{F}} = \pi * r \tag{10}$$

Found by using the Hapke radiative transfer model in Equation 11, the bidirectional reflectance can be found using the optical constants of the surface [46]. In this equation, r is the bidirectional reflectance, K is the porosity parameter, $\bar{w}$ is the single scattering albedo, P is the single particle phase function, B_{SH} is the shadow hiding opposition effect, B_{CB} is the coherent back-scattering opposition effect, H is the Ambartsumian–Chandrasekhar functions describing the multiple scattering components, S is the shadowing function, and μ_{0e} and μ_e are the effective incidence and emergence angles. These terms will be explained in more detail in the sections below.

$$r(i,e,g) = K * \frac{\bar{w}(\lambda)}{4\pi} \frac{\mu_{0e}}{\mu_{0e} + \mu_e} \left[B_{\text{SH}} P(g,\lambda) + H(\bar{w},\mu_{0e}) H(\bar{w},\mu_e) - 1\right] \times S(i,e,g,\theta) B_{\text{CB}}(g,\lambda) \tag{11}$$

5.2 Geometric Angles

Before discussing the parameters of the Hapke model, the geometric angels which have a large influence on the outcome of the model will be explained first. Four angles are taken into account while measuring the reflectance: incidence angle (i), emergence angle (e), phase angle (g), and the azimuth angle (Ψ).

The angle of incidence is the angle of the light hitting the surface about a perpendicular line from the surface at that point. The angle of emergence is the angle of the light reflecting off of the surface about a perpendicular line from the surface at that point. These angles can be seen in Figure 34 below when the azimuth angle, which will be explained later in this section, is set to 180 degrees.

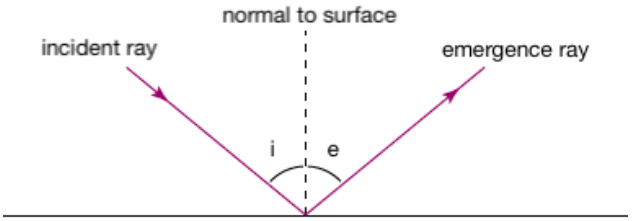

Figure 34: Explanation of incidence and emergence angle for the Hapke model. [11]

The phase angle is the angle between the incident light on an observed object and the reflected light off of the object to the observer. Formula 12 shows how the phase angle is affected by the angle of incidence and emergence and the azimuth angle. The azimuth angle, Ψ, is the angle between the light plane from the Sun to the object and the plane from the object to the observer. These relationships can be found in Figure 35. Therefore, when the two planes are co-linear (the azimuth angle is either 0 ° or 180 °) the phase angle is just the absolute value of the incident angle minus the emergent angle, or $|i-e|$. Keeping the incident and emergence angles constant and changing the azimuth angle is plotted below in Figure 36.

$$g = \text{acos}(\cos(e) * \cos(i) + \sin(e) * \sin(i) * \cos(\Psi)) \tag{12}$$

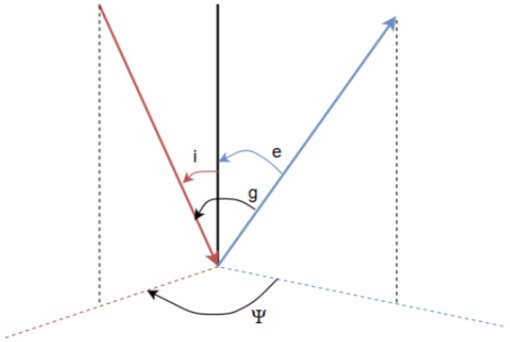

Figure 35: Explanation of phase angle for the Hapke model.

Below in Figure 36, the effect on the reflectance by changing the incident, emergence, and azimuth angles can be seen. Figure 36a, shows how the reflectance changes as the incidence angle changes over a 180 degrees span from -90 to 90 degrees with a maximum occurring at 20 degrees and

minimum at -90 and 90 degrees. The maximum value occurring at 20 degrees is because the emergence angle is set to 20 degrees. The reflectance is maximized when the light hits the surface at a perpendicular angle and is reflected in the same direction that it came from. Figure 36b shows how the reflectance changes as the emergence angle changes over a 180-degree span. The maximum of this graph is at -90, and 90 degrees, and a local maximum occur at 20 degrees. Just as with the plot that changes the incidence angle, the local maximum at 20 degrees is because the light will be reflected in the same direction it came from which yields a higher I/F value. Changing the azimuth angle, Ψ, can change the reflectance of the spectra. Figure 36c below shows how the reflectance will change based on changing the azimuth angle and keeping all other input parameters constant. The maximum of this plot is when the azimuth angle is at 0 degrees, and the minimum value is located at 180 degrees. The smaller the azimuth angle, the less the light is affected by the surface it is reflected off of which makes the reflectance higher.

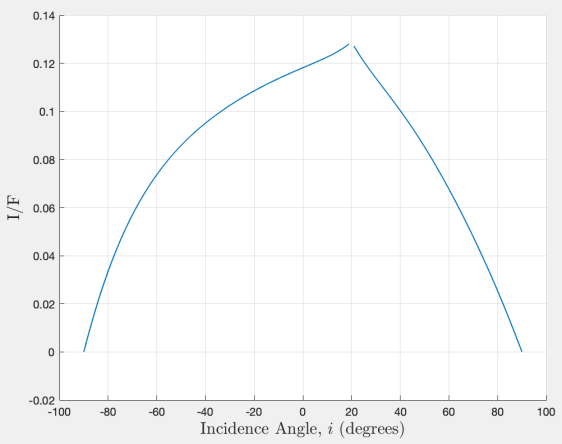

(a) Emergence Angle 20 degrees; Incidence Angle varies from -90 to 90 degrees. Azimuth angle 0 degrees.

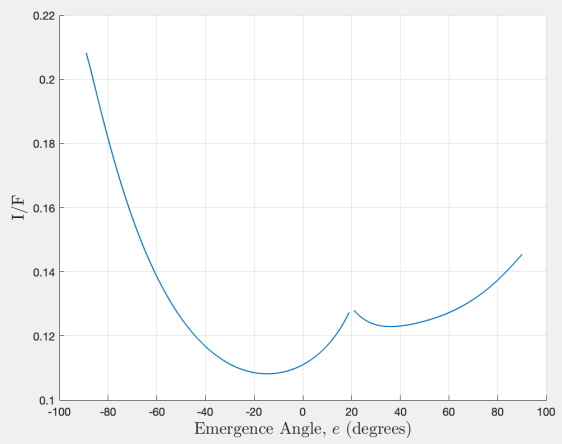

(b) Incident Angle 20 degrees; Emergence Angle varies from -90 to 90 degrees. Azimuth angle 0 degrees.

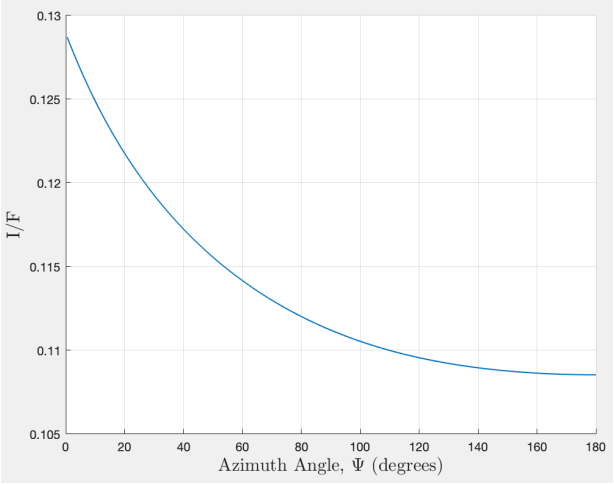

(c) Relation between the azimuth angle and the reflectance. The wavelength is 2 μm and the incidence and emergence angles are both 20 degrees.

Figure 36: Plots showing how varying the incidence, emergence, and azimuth angles changes the I/F values at the 2 μm wavelength for crystalline water ice.

5.3 Single Scattering Albedo, $\bar{w}$

The first parameter is the particle single scattering albedo, $\bar{w}$. This is the ratio of the scattering efficiency to the total extinction efficiency and is expressed as follows:

$$\bar{w} = Q_S/Q_E$$

where $Q_E = 1$

$$Q_S = S_e + (1 - S_e)\frac{1 - S_i}{1 - S_i\Theta}\Theta$$

$$S_e = \frac{(n-1)^2 + k^2}{(n+1)^2 + k^2} + 0.05 \tag{13}$$

$$S_i = 1 - \frac{4}{n(n+1)^2}$$

$$\alpha = \frac{4\pi k}{\lambda}$$

$$\Theta = e^{-\alpha < D >}$$

$$< D >= \frac{2}{3}\left[n^2 - \frac{1}{n}\left(n^2 - 1\right)^{3/2}\right]D$$

where Q_S is the volume-average scattering efficiency including diffraction, Q_E is the volume-average extinction efficiency, S_e is the external surface reflection coefficient, S_i is the internal surface reflection coefficient, Θ is the particle internal transmission factor, n is the real refractive index ($n = n_r + in_i$), k is the solid state thermal conductivity (or the imaginary refractive index explained in Section 4.6), α is the absorption coefficient, D is the particles mean diameter (explained in Section that $D = 2a$), and $< D >$ is the mean ray path length through particle [46]. Q_E is assumed to be 1 since the particles are larger in diameter than the wavelength [46].

5.3.1 Mean Particle Size, D

The mean particle size is the average diameter of the particles you are observing. As shown in Figure 74, as the mean diameter of the particles being observed increases, the depth of the absorption decreases. The spectral contrast between the peaks and valleys becomes more intense as the mean particle size increases. This is intuitive since as the grain size increases, then there is more material to absorb energy, and the reflectance will be reduced, causing a deeper valley. In Figure 37, the trend is shown for the same range of wavelengths as the VIMS data. It can be seen that the larger mean diameters have lower REFF values and have more pronounced peaks and valleys. Also, as the grain size increases, the surface will become less smooth. The smaller grain size allows for the particles to fit together in an efficient arrangement. The smoother surface of materials with smaller grains reflects more light back which is why the reflectance in Figure 37 for smaller grains is larger.

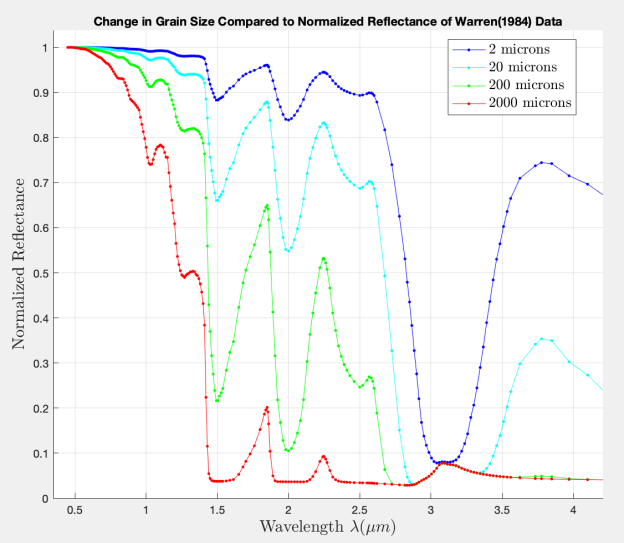

Figure 37: Change in REFF using Warren (1984) based on different grain sizes over the wavelengths 0.75 to 5.714 μ*m* [45].

5.4 Single Particle Phase Function, P

The phase function $P(g,\lambda)$ is modeled by the Henyey-Greenstein functions. These functions are divided into groups depending on the number of scattering lobes they present (1 or 2) and depending on their asymmetrical parameters. Hapke uses the two lobes function which is more representative of the data if the phase angle covers a larger scale. The phase function is described by the following function [46].

$$P(g) = \frac{1+c}{2}\frac{1-b^2}{(1-2b\cos g+b^2)^{3/2}} + \frac{1-c}{2}\frac{1-b^2}{(1+2b\cos g+b^2)^{3/2}} \tag{14}$$

In this function, b is the width parameter and is constrained between $0 \leq b < 1$. The phase function has to be positive which can be tuned by changing the values of c, and g is the phase angle. Since P has extremes when g is equal to 0 and 180 degrees, that requires c to be limited to $|c| \leq \frac{1+3b^2}{b(3+b^2)}$ [47]. The first term in Equation 14 represents the backscatter lobe and the second term represents the forward-scattering lobe [46]. It can be seen in the equation that the sign of c determines which directional scattering is favored in the equation. Negative c values mean that the particle is mostly forward scattering, and positive values mean that the particle is mostly backward scattering. b affects the width and height of the lobe. Small values of b mean that the lobes are low and wide, and large values means the lobes are high and narrow [47]. An increase in a particle's internal density, grain roughness, and internal absorption causes the particle to have a higher c value and lower b value. Inversely, a decrease in a particle's surface roughness and differences in the internal composition (i.e., a more clear particle) tends to reduce c and increase b [48]. Figure 38c shows how changing the value of b affects the change in albedo. The trend in this figure shows that at low phase angles, the albedo gets greatly affected by changes in b. The values of b have been found for each of the three regions. For the red region, b is equal to 0.22, for the crater region, b is equal to 0.2, and for the tiger stripe region, b is equal to 0.18 [49]. Using the Hockey Stick function in Equation 15, using the value of b, c can be obtained [46]. Figure 38a shows the relation between b

and c and Figure 38b shows how changing b effects the phase function P.

$$c = 3.29 * e^{-17.4*b} - 0.908 \tag{15}$$

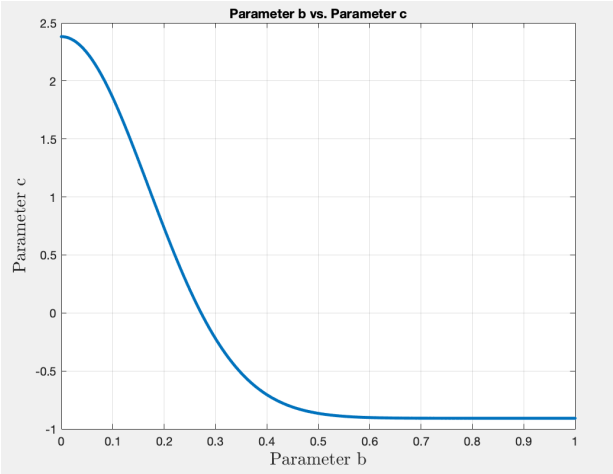

(a) Relation between the parameters b and c using the Hockey Stick Equation in Equation 15. The limit of c is equal to -0.908 which is what is subtracted in Equation 15.

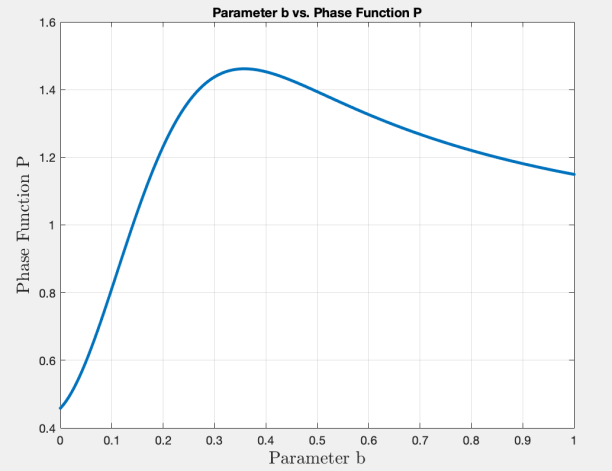

(b) Relation between parameter b and the Phase Function P using Equation 14 with the phase angle equal to 40°.

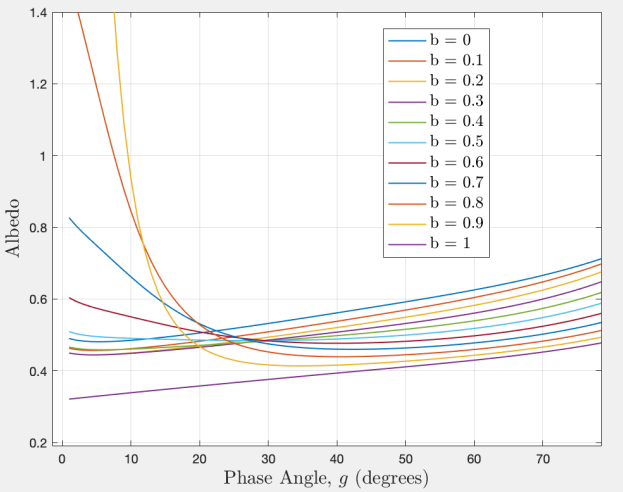

(c) Visual description of how changing the single particle scattering function amplitude, b, affects the albedo when looking at different phase angles for crystalline ice.

Figure 38: Showing the different affects on the Phase Function from b.

5.5 Filling Factor, ϕ

The filling factor parameter describes the volume fraction within the material which is occupied by grains. The filling factor ϕ is equal to one minus the porosity. By calculating the filling factor, the porosity of the surface materials can be concluded. The range of the filling factor can be from zero to one [50]. However, by observing Figure 39, the albedo increases as the filling factor increases until 0.75. After the filling factor reaches 0.75, the albedo values begin to decrease again. This is because when ϕ becomes 0.752, the material would become opaque [49]. At ϕ equalling 0.752, h_s

in Section 32 would become indefinitely wide and no longer have a shadow hiding effect [49]. In Equation 16, this is the value that would make the numerator undefined. Because of this, the range of values used in this study will be from 0 to 0.75 to allow for increased efficiency while running the Hapke model.

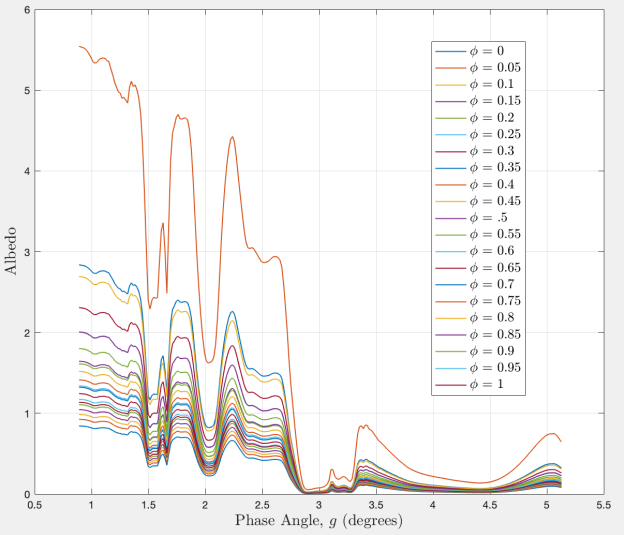

Figure 39: Visual description of how changing the filling factor, ϕ, affects the albedo.

5.5.1 Compaction Correction, K

The compaction correction in the Hapke model is referred to as K. This parameter corrects for the grain packing in the uppermost regolith layer which is affected by the macro-porosity [49]. Macro-porosity describes the amount of space taken up by the pores in the ice that are much larger than the grains. K is dependent on the filling factor, ϕ, and can be calculated using the following equation [50].

$$K = \frac{-\ln\left(1 - 1.209\phi^{2/3}\right)}{1.209\phi^{2/3}} \tag{16}$$

5.6 Surface Roughness, $\bar{\theta}$

The surface roughness is the mean slope angle of the surface averaged over a size range [50]. These surface elements that can affect the surface roughness can be as large as mountains or craters and can be as small as millimeter-sized clumps of grains on the surface. The lower the surface roughness, the smoother the surface which correlates with a higher albedo. Figure 40 below shows how changing the surface roughness affects how the albedo will change. As the surface roughness increases, the albedo values decrease. This is due to less light being reflected as the surface angle is increased. The less of an angle that the surface is, the more light that is reflected.

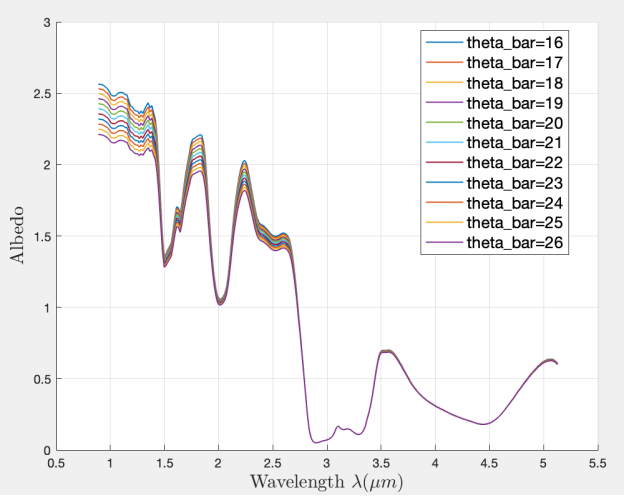

Figure 40: Visual description of how changing the surface roughness, $\bar{\theta}$, affects the albedo.

5.7 Shadowing Function, S

The shadowing function $S(i,e,g)$ accounts for the roughness of the surface. Its impact of the reflectance requires the following previous intermediate functions:

$$\bar{\theta}_p = (1 - r_0)\,\bar{\theta} \tag{17}$$

$$\chi(\bar{\theta}_p) = \frac{1}{\sqrt{1 + \pi \tan^2(\bar{\theta}_p)}} \tag{18}$$

$$E_1(y) = \exp\left(-\frac{2}{\pi \tan(\bar{\theta}_p)\tan(y)}\right) \tag{19}$$

$$E_2(y) = \exp\left(-\frac{1}{\pi \tan^2(\bar{\theta}_p)\tan^2(y)}\right) \tag{20}$$

$$f(\psi) = \exp\left(-2\tan\left(\frac{\psi}{2}\right)\right) \tag{21}$$

$$\eta(y) = \chi(\bar{\theta}_p)\left(\cos(y) + \sin(y)\tan(\bar{\theta}_p)\frac{E_2(y)}{2 - E_1(y)}\right) \tag{22}$$

where r_0 is the diffusive reflectance, $\bar{\theta}$ is the mean roughness angle, $\bar{\theta}_p$ is the effective value of the roughness that is measured photometrically, χ is the average cosine of the surface tilt angle, E_1 is the volume-average extinction coefficient for the first medium the particle is traveling in, E_2 is the volume-average extinction coefficient for the second medium the particle is traveling in, y is either the angle of incidence, i, or the angle of emergence, e (explained in Section **??**), $f(\psi)$ is the fraction of the illumination shadow that is hidden in the visible shadow, ψ is the particle scattering difference factor, η is the amplitude of complex specular reflection coefficient at normal incidence, thermal beaming factor.

x can be either the emergent of the incident angle [46].

Two different cases are depending on the relation between the emergent and incident angle [46]. Where i_e and e_e are the effective angles of incident and emergence.

If $e \geq i$:

$$\mu_{0e} = \cos(i_e) = \chi(\bar{\theta}_p)\left(\cos(i) + \sin(i)\tan(\bar{\theta}_p)\frac{\cos(\psi)E_2(e) - \sin^2(\psi/2)E_2(i)}{2 - E_1(e) - (\psi/\pi)E_1(i)}\right) \tag{23}$$

$$\mu_e = \cos(e_e) = \chi(\bar{\theta}_p)\left(\cos(e) + \sin(e)\tan(\bar{\theta}_p)\frac{E_2(e) + \sin^2(\psi/2)E_2(i)}{2 - E_1(e) - (\psi/\pi)E_1(i)}\right) \tag{24}$$

$$S(i,e,\psi) = \frac{\mu_e}{\eta(e)}\frac{\mu_0}{\eta(i)}\frac{\chi(\bar{\theta}_p)}{1 - f(\psi) + f(\psi)\chi(\bar{\theta}_p)(\mu_0/\eta(i))} \tag{25}$$

If $e \leq i$:

$$\mu_{0e} = \cos(i_e) = \chi(\bar{\theta}_p)\left(\cos(i) + \sin(i)\tan(\bar{\theta}_p)\frac{E_2(i) + \sin^2(\psi/2)E_2(e)}{2 - E_1(i) - (\psi/\pi)E_1(e)}\right) \tag{26}$$

$$\mu_e = \cos(e_e) = \chi(\bar{\theta}_p)\left(\cos(e) + \sin(e)\tan(\bar{\theta}_p)\frac{\cos(\psi)E_2(i) - \sin^2(\psi/2)E_2(e)}{2 - E_1(i) - (\psi/\pi)E_1(e)}\right) \tag{27}$$

$$S(i,e,\psi) = \frac{\mu_e}{\eta(e)}\frac{\mu_0}{\eta(i)}\frac{\chi(\bar{\theta}_p)}{1 - f(\psi) + f(\psi)\chi(\bar{\theta}_p)(\mu_0/\eta(e))} \tag{28}$$

5.7.1 Ambartsumian–Chandrasekhar Functions, H

The Ambartsumian–Chandrasekhar functions H($\bar{w}$, x) are found using the following equations:

$$\gamma = \sqrt{1 - \bar{w}} \tag{29}$$

$$r_0 = \frac{1 - \gamma}{1 + \gamma} \tag{30}$$

$$H = \frac{1}{1 - \bar{w} * x * (r_0 + \frac{2 * r_0 * x}{2} * \log\frac{1+x}{x})} \tag{31}$$

Equation 31 represent the multiple scattering effect using the angles μ_{0e} and μ_e found in Section 5.7 [46].

5.8 Shadow Hiding opposition effect (SHOE), B_{SH}

The shadow hiding opposition effect (SHOE) occurs when the grains at the surface cast a shadow on the grains below them. This effect is dependent on the phase angle since the shadows that are cast are most effective at large phase angles. When the phase angle is low, the shadow is not as large and directly below the particle. The shadow being below the particle means that the view is unable to detect the shadow [46]. This dependence can be seen in Figure 41, as the phase angle increases, the albedo increases.

5.8.1 Shadow Hiding opposition effect (SHOE) amplitude, B_{S0}

The shadow hiding opposition effect (SHOE) amplitude measures the grain transparency within a medium. B_{S0} has a range from zero to one, with numbers closer to zero being the most transparent and numbers closer to one being more opaque [51]. Figure 41 below shows how changing B_{S0} and the phase angle affects how the albedo will change. As the values of B_{S0} become closer to 1, the albedo becomes larger. This is because the more transparent the grain is, the less light will be reflected. The change in albedo from B_{S0} values of 1 and 0 become less apparent as the phase angle increases. At large phase angles, the transparency of the grain has a lower effect on how much light is reflected.

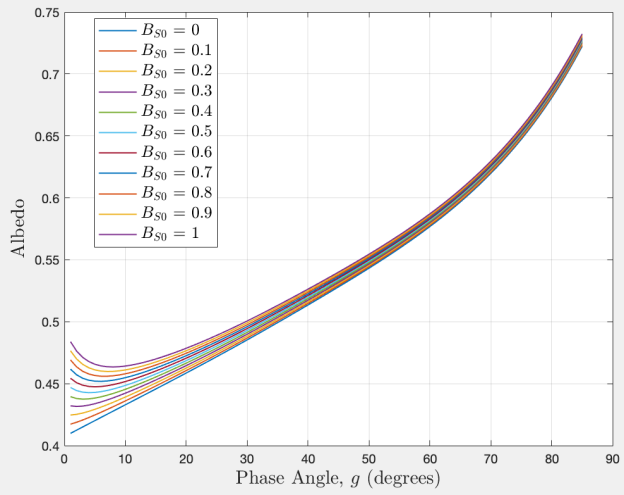

Figure 41: Visual description of how changing the Shadow Hiding opposition effect (SHOE) amplitude, B_{S0}, affects the albedo. The albedo values are taken at 2.5 μm.

5.8.2 Angular Width of SHOE, h_S

The angular width, h_S, is the width of the opposition effect due to shadow hiding (SHOE) [50]. This width is related to the grain size and the filling factor within the scattering material. The equation to solve for the angular width can be seen below. Equation 32 shows that h_S changes as the filling factor and compact correction changes. Since the compact correction is dependent on the filling factor, h_s can be simplified to an equation only depending on the filling factor. As the filling factor, ϕ, increases, the porosity of the surface decreases, and the surface becomes denser. The more dense the surface is, the more light gets reflected by the surface, and more light is absorbed.

$$h_S = \frac{3}{8} K\phi = -\frac{3}{8}\frac{\phi \ln\left(1 - 1.209\phi^{2/3}\right)}{1.209\phi^{2/3}} \tag{32}$$

5.9 Coherent Back Scattering Effect (CBOE), B_{CB}

The coherent back scattering effect occurs when particles reflect light below the surface and then back out again at the observer. Figure 42 shows how the effect takes place. The light gets reflected by at least two particles before it gets reflected out of the surface. Since it is possible for the light to travel one way through this path, the reverse is also possible. The additional light leaving Point A in the figure from the light entering from Point B creates this effect. This effect is dependent on the phase angle as well. The effect is most effective at low phase angles [46].

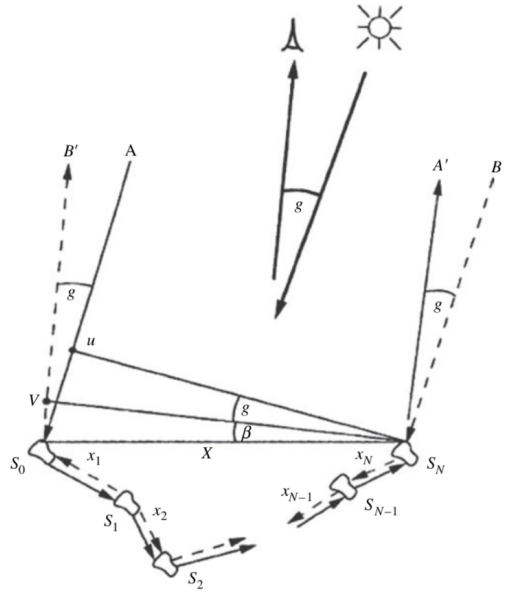

Figure 42: Visual representation of how the coherent back scattering effect (CBOE) takes place on the surface [46].

5.9.1 Coherent Back Scattering amplitude, B_{C0}

The coherent back scattering (CBOE) amplitude is the amplitude of the opposition effect due to the coherent backscatter [50]. This value is from zero to one. As can be seen in Figure 43, the change in albedo as B_{C0} changes in value, the albedo does not change. Therefore, this parameter will not be taken into account and assumed to be equal to one to save time while running the Hapke model.

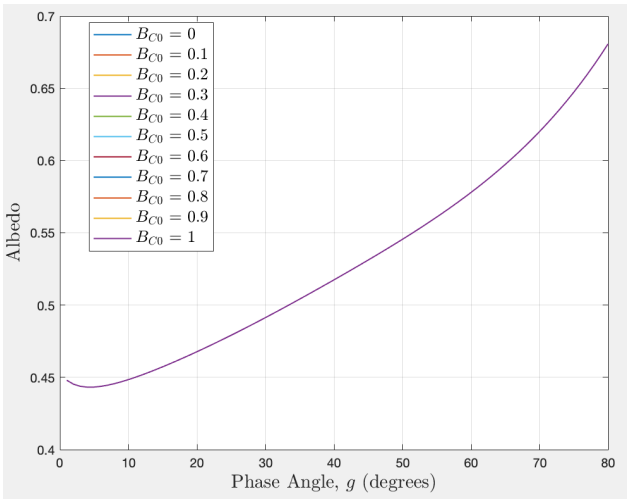

Figure 43: Visual description of how changing $B_{c)}$ affects the albedo. This was performed at 2.5 μm for crystalline water ice.

5.9.2 Transport Mean Free Path

The transport mean free path is the average distance a wave can travel through a medium before its direction is randomized. This value can be calculated by using the grain size, single scattering albedo, and the filling factor [51]. This value is used to calculate B_{CB} used to find the reflectance. However, by looking at Figure 44, changing the transport mean free path does not have an effect on changing the albedo, therefore, this parameter will not be optimized and considered to be 33. This will save time while running the Hapke model since there will be one less free parameter. The value of 33 comes from Verbiscer et. al (2018) which found the transport mean free path on the surface of Enceladus to be 33 [51].

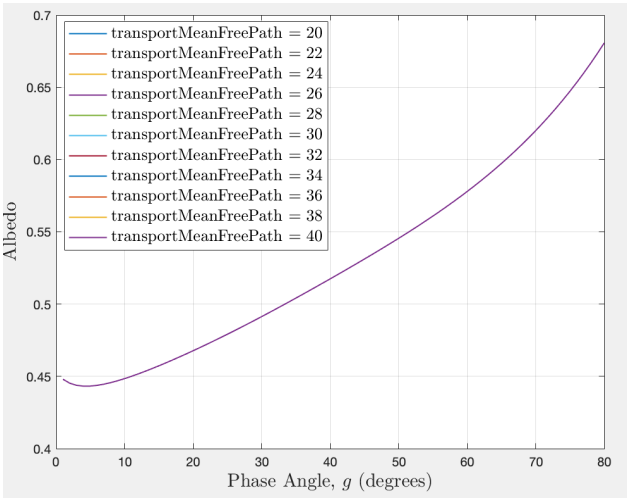

Figure 44: Visual description of how changing the mean free path affects the albedo. This was performed at 2.5 μm for crystalline water ice.

6 Results

In this section, the method for acquiring the results will be explained. Next, the results will be shown for each region and broken down into the four different parameters of the Hapke model: the grain size, filling factor, surface roughness, and crystallinity. Each region can be seen below in Figure 45. The temperature of the ice in each region will also be discussed in this section. In contrast to the parameters of the Hapke model being found numerically, the temperature is found analytically by looking at the 3.6 μm peak.

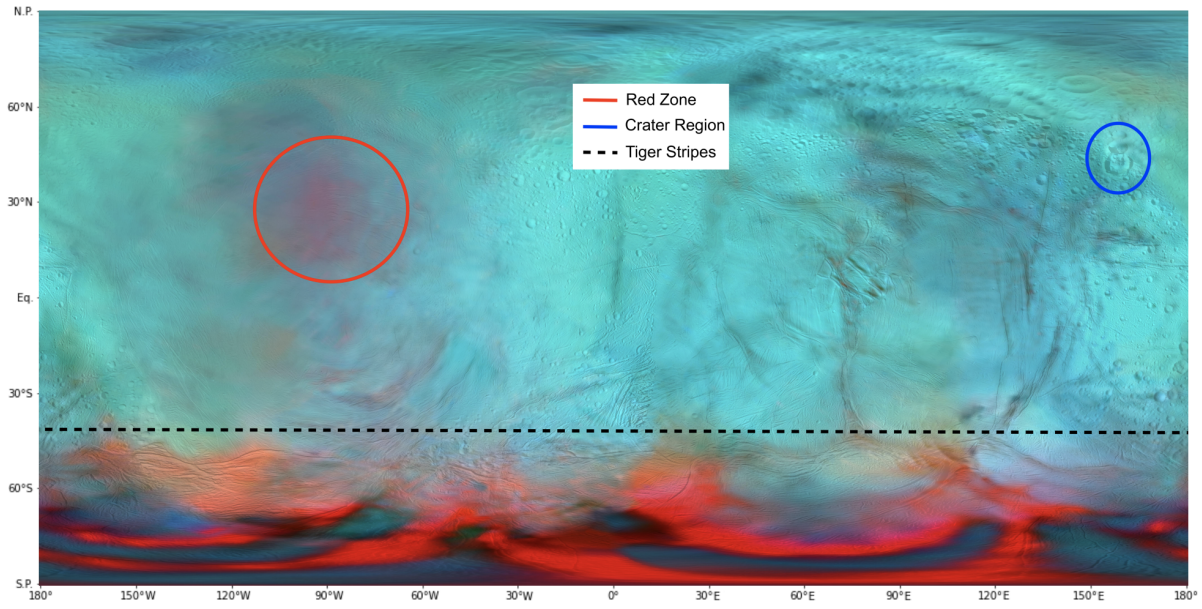

Figure 45: The mosaic of Enceladus shows each of the three regions that have been examined. The red zone is located around $30°N$ and $90°W$. The crater region on the side of Enceladus with uneven terrain. Lastly, the tiger stripes in the southern hemisphere of Enceladus. The tiger stripes region is below the dashed black line focusing on the deep red regions where the plumes and faults are located. [11]

6.1 Spectral Fitting

The Hapke model of reflectance in Section 5 can now be used to analyze the spectra taken from the Cassini data in Section 4. To be able to fit the output spectra from the Hapke model to the spectra acquired from Cassini, four parameters will be changed to find the best fit. The four parameters that are considered in this study are the diameter of the grains, the filling factor which determines the porosity, the surface roughness, and the percentage of crystalline ice that the surface materials are comprised of. The fit will be done by performing a grid search style technique to find the values of the parameters which reproduce the observed data the best. The grid search technique is done by evaluating every combination of values for the parameters and finding which combination yields the smallest difference. For example, if there are four parameters and each one is given ten possible values, then there are 10,000 possible combinations. The model will be run 10,000 times and the combination with the smallest difference will be outputted. The grid search is an efficient method to use because the input parameters can be manually selected within a specified range. Since the approximate values for the parameters on the surface of Enceladus are known, this will reduce the range of values that need to be tested.

The grid search will be performed on each of the 63 locations on the surface of Enceladus that were specified in Section 4. This will provide the best fit of the spectra and values for the four surface parameters mentioned above. These parameters will show how the different regions on the surface of Enceladus differ and will give insight as to why the red region has different surface qualities compared to the surrounding areas. The spectra produced using the Hapke model will be compared to the spectra from the VIMS data by using a chi-squared test. Equation 33 below shows how the chi-squared value is calculated. With O_i being the observed albedo value from the Hapke model spectra, and E_i being the expected albedo value from the VIMS spectra. The equation is summed for each wavelength position, and the total is the chi-squared value for that specific combination of parameters. The lowest chi-squared value corresponds to the spectra that have the closest fit with the VIMS data.

$$\chi^2 = \sum \frac{(O_i - E_i)^2}{E_i} \tag{33}$$

The spectra will be analyzed between the wavelength range from 0.89 to 2.74 μm. The lowest value of this range is due to the starting range at which the VIMS instrumentation begins to collect data. The high value of the range is due to the low albedo intensity around the 3 μm area. The low albedo values in this region have intensities near zero. If there are slight errors when the albedo values are close to zero, the chi-squared value for the fit produces enormously high values. So to prevent this error in calculation, the fit is only performed on albedo values that are not close to zero. Figure 46 shows an example of the resulting spectra fit to position 10 from the Tiger Stripe region. As mentioned earlier in Section 4.6.2, larger wavelengths, such as the peak at 3.6 μm, are difficult to fit using the optical constants from Mastrapa [44]. Since this region is mostly used to find the temperature of the ice, this wavelength region will be evaluated separately to find the wavelength location of the peak at 3.6 μm. This fit will be done by manually determining the location of the peaks at 3.6 μm and comparing the values to the water constants found in Section 4.6.2 to determine the temperature of the ice. In the following sections, the different regions studied and their characteristics obtained by the Hapke model are discussed.

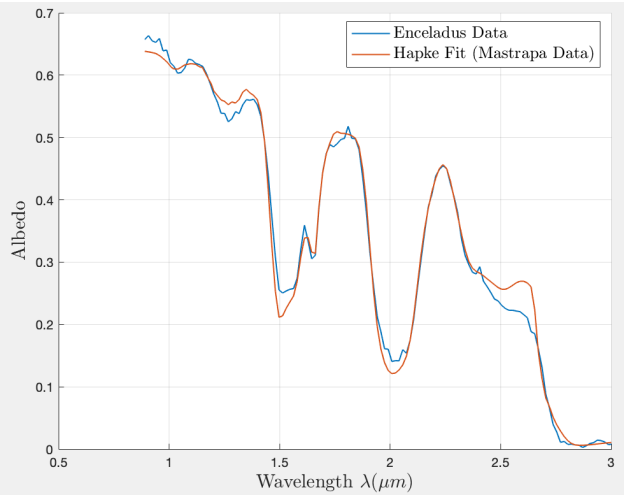

Figure 46: Example of a fit done on a VIMS spectra taken from the Cassini data. This is spectra 10 taken from the Tiger Stripes. The fit is only determined from 0.89 to 2.74 μm due to the low values of the albedo above this range. This fit yields a grain diameter of 48 μm, surface roughness of 56 degrees, a porosity of 72%, and 49% of the ice being crystalline.

6.2 Red Zone

The region in the northern hemisphere of Enceladus that is centered at 30°N and 90°W is referred to as the red zone. This region is circled on the map in Figure 45 to give a clear representation. This area was of interest because it has larger grain sizes and percentages of crystalline ice than the surrounding areas of the moon [11]. Figure 45 shows that the red region closely resembles that of the tiger stripe region in grain size and crystallinity. This section will provide the results from fitting the Hapke model to the 35 locations specified in Section 4. The location, size, and spectra of each of the 35 pixels used are found in Figure 47. The parameters found from studying the individual spectra in this region are an average value over the surface within each pixel. Figure 47a shows the size and location of each pixel that is being observed. Figure 47b shows each photometrically corrected spectra present on Figure 47a. The differences in each spectra will provide an insight into how the surface parameters in this region change.

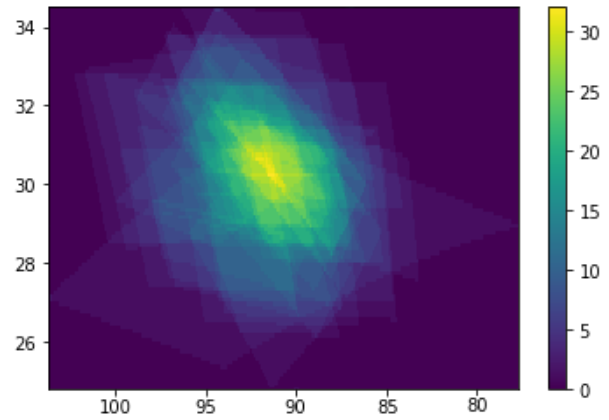

(a) The number of times a location is found in the pixel in the red zone. The x-axis is the longitude west, and the y-axis is the latitude north.

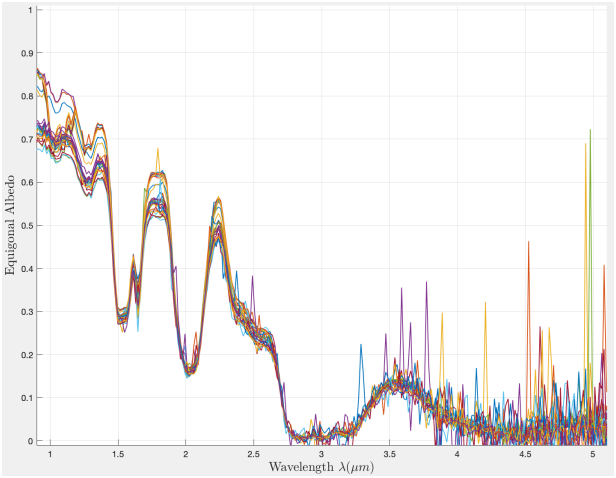

(b) All 35 spectra used to analyze the red region. These spectra have been photometrically corrected.

Figure 47: Figures from Section 4 used to show the size of the pixel used to gather the information from and the different spectra laid on top of one another.

6.2.1 Grain Size

The diameter of the grain sizes in the red region range from 43 μm to 60 μm. In Figure 45 the red zone has the deepest red coloration at 30°N and 90°W. The red coloration represents the areas with larger grain sizes and higher percentages of crystallinity. The points on the plot in Figure 48 represent the average diameter of the grains within the pixel observed. Figure 48 shows that the pixels that have centers closest to 30°N and 90°W has the largest grain sizes. The findings in this study correlate to the findings of Robidel et al. (2020), which were used to make the mosaic in Figure 45 and the background image for Figure 48 [11]. As the center of the pixel goes further from 30°N and 90°W, the grain size diameter becomes smaller.

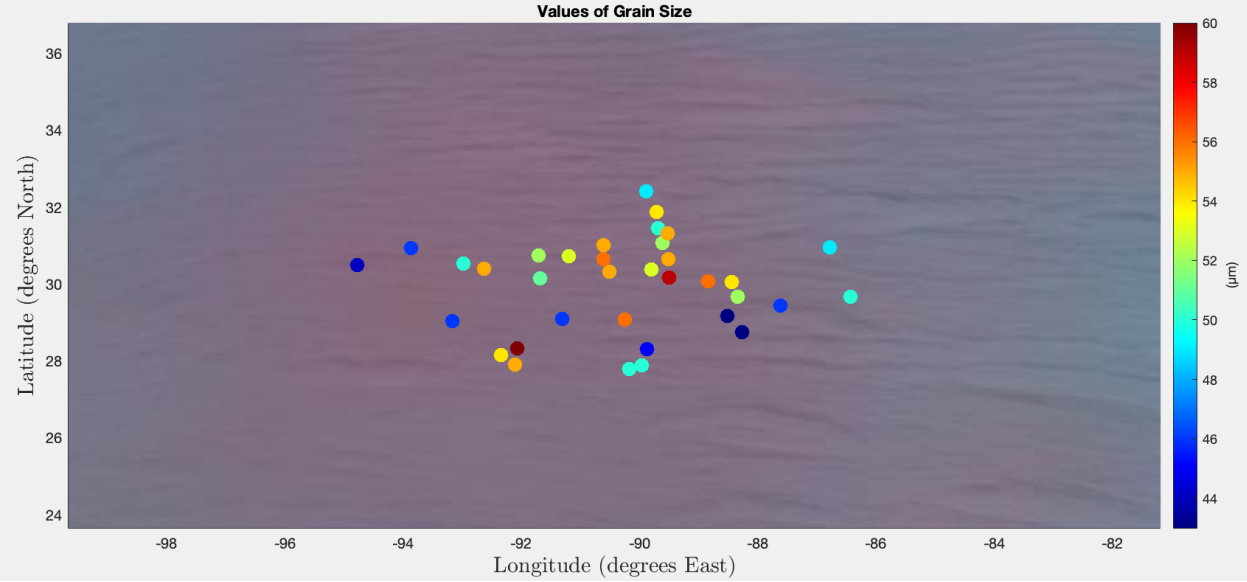

Figure 48: Map of the red region which shows the different grain sizes in the region. The diameters of the grain sizes are shown in μm.

6.2.2 Filling Factor, ϕ

The filling factor of the surface represents the density of the surface particles. In the red region, the filling factor values range from 9 to 39 % with the maximum percentages being centered around $30°N$ and $90°W$. As the center of the pixel goes further from this location, the filling factor becomes smaller and the surface becomes less dense. The pixel size is large enough to extend far away from $30°N$ and $90°W$ for the pixels which centers are on the outside of the cluster in Figure 49. Those pixels include grains on the edge of the red region which is why the trend can be seen.

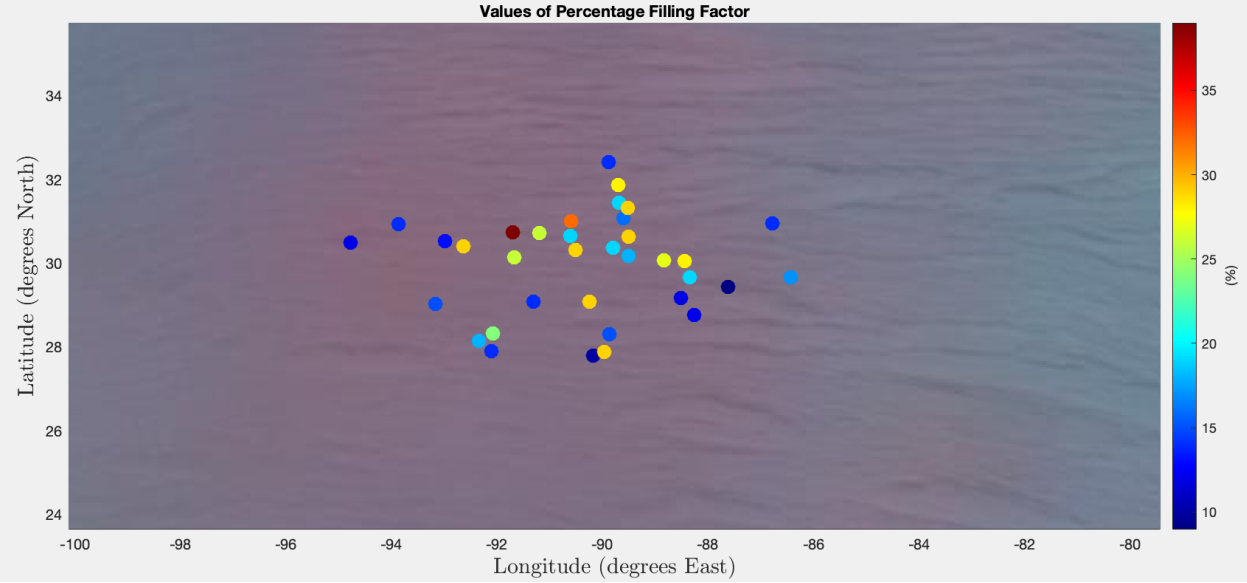

Figure 49: Map of the red region that shows the different filling factor percentages in the region. The filling factor is a value between 1 and 0 which correlates to the percentage of space in a given volume that is taken up by the material.

6.2.3 Surface Roughness, $\bar{\theta}$

The surface roughness of the red region ranges from 27° to 49°. This represents the average slope of the surface within the pixel. It is noticeable that the steepest surfaces are located closer to the $30°N$ and $90°W$ location. Within this region, there is a trend of higher values the further north and the further west the pixel is. From the map below, there do appear to be more uneven surfaces north and west of the $30°N$ and $90°W$ center location. However, these values are very large considering that the values are the average surface roughness over the entire pixel. It is noticeable in Figure 50 that there are cracks in the ice surface. These cracks could be caused by resurfacing which would make the surface uneven. The lack of craters in this region also points to resurfacing occurring in this region recently. The trend appears to be correct, but the values are surprisingly high.

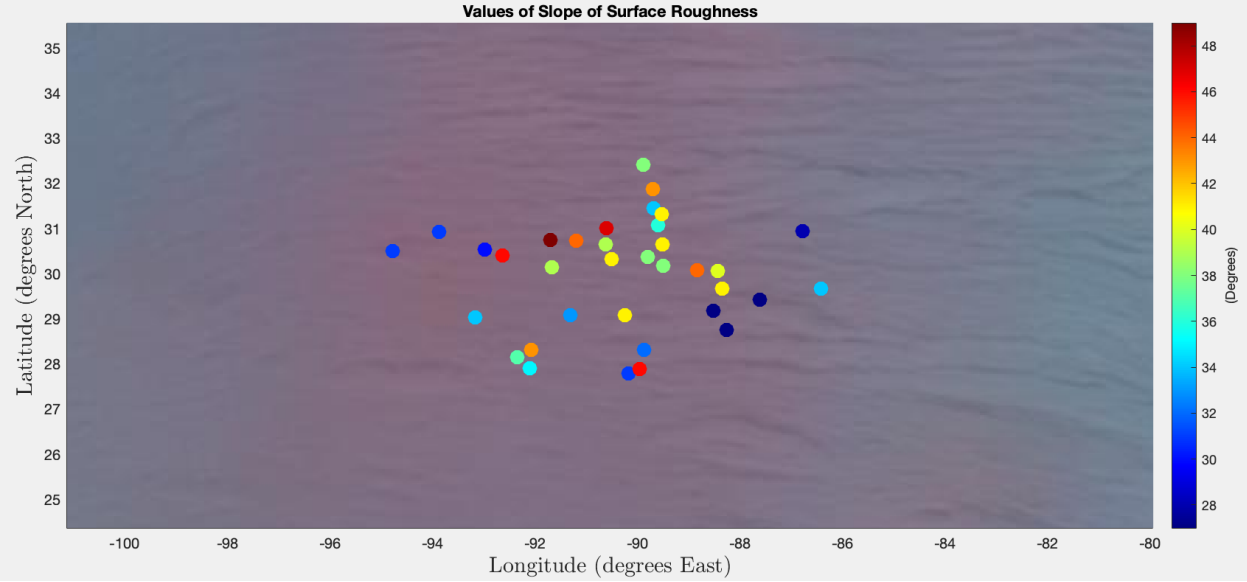

Figure 50: Map of the red region that shows the different surface roughness's. Theta bar is measured in degrees and is the slope angle of the surface.

6.2.4 Percentage of Crystalline Ice

Figure 51 shows the average percentage of crystalline ice in the region for each pixel found in the red region. The difference in percentages of crystalline ice in this region does not differ much, but the higher percentages can be found closest to $30°N$ and $90°W$. Again, this correlates to the results found by Robidel et al. (2020) that $30°N$ and $90°W$ has a higher percentage of crystalline ice than the surrounding regions [11].

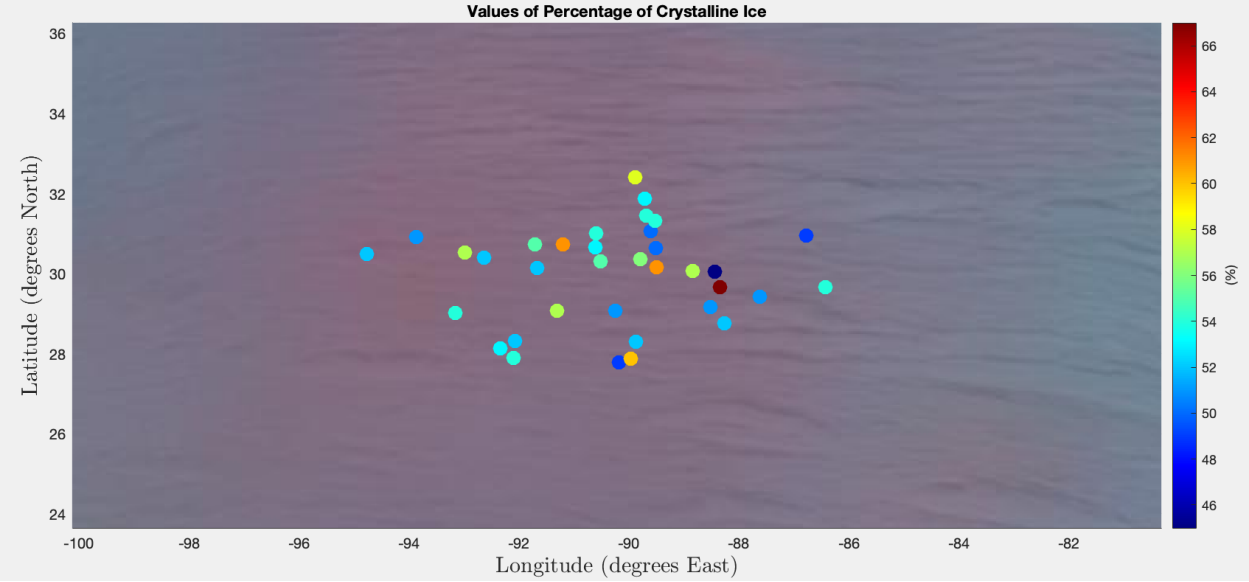

Figure 51: Map of the red region that shows the different percentages of crystalline ice.

6.2.5 Surface Temperature

Figure 60 shows each of the photometrically corrected spectra overlaid on top of one another and the average of all of the spectra in the 3.2 to 4 μm range. The average spectra are used to allow for the peak of the 35 spectra to be visualized. For the red zone region, the 3.6 μm peak is located at 3.5708 μm. Using Equation 7, the approximated deposition temperature of the ice in this region is found to be 82 degrees Kelvin.

The temperature was also found while using optical constants dependent on the temperature in the Hapke model. Figure 52c shows the corresponding temperature used in the Hapke model to produce the best fit for each spectra. The results correlate to the temperature of the ice in the laboratory that was used to find the optical constants [43]. The optical constants were found in increments of 20 degrees Kelvin, so the values are not as precise as the linear method used in Equation 7. The majority of the points used the optical constants from 80 degrees Kelvin to find the best fit. These values are similar to the results found using the peak of the 3.6 μm value.

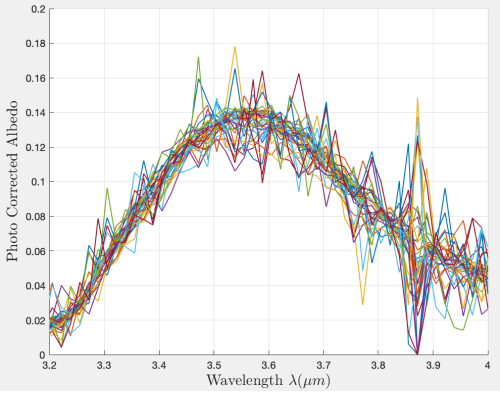

(a) The 35 photometrically corrected spectra from the red zone all plotted on the same plot focusing on the 3.6 μm region.

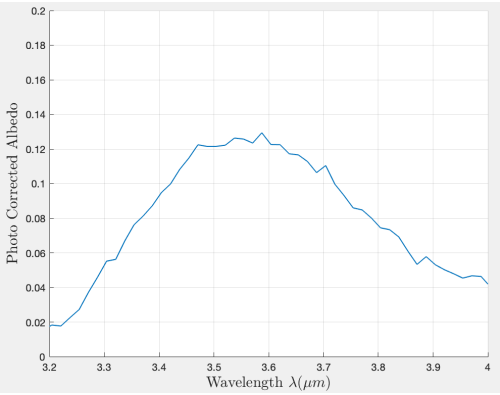

(b) The mean spectra produced from the plot in Figure 52a.

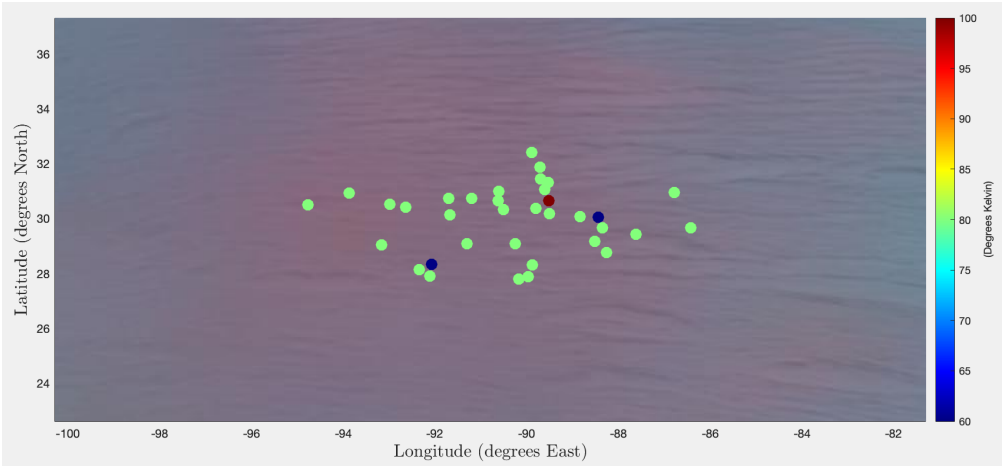

(c) Map of the red region that shows the temperature of the optical constants used to achieve the best fit with the Hapke model.

Figure 52: Surface temperature findings for each of the pixels used in the red region. Figures 52a and 52b show the 3.6 μm peaks used to calculate the temperature from the spectra. Figure 52c shows the temperature of the optical constants used during the Hapke model to acquire the best fit.

6.3 Crater Region

The region in the northern hemisphere of Enceladus is showing a large crater region around $45°N$ and $165°E$. This region is circled on the map in Figure 45 to give a clear representation. This area was of interest because it has had recent resurfacing due to impacts. Craters in this region can be seen. This section will provide the results from fitting the Hapke model to the 14 locations specified in Section 4. Figure 53a shows the location and size of each pixel that has been observed. The color of the outline correlates to the color of the dot, which is located at the center of the pixel. Pixels from the same flyby are represented in the same colored box and dot. Since the pixel resolution in this area is low, the pixels cover a large surface area, making it difficult to acquire the changes occurring on the surface. Due to the large pixel size, the results for each location will be discussed by comparing where the pixels overlap. For example, if two pixels are overlapping within a crater, and one of the pixels extends outside of the crater, the surface properties for the surface outside of the crater can be deduced. Figure 53b shows the 14 photometrically corrected spectra used in this region.

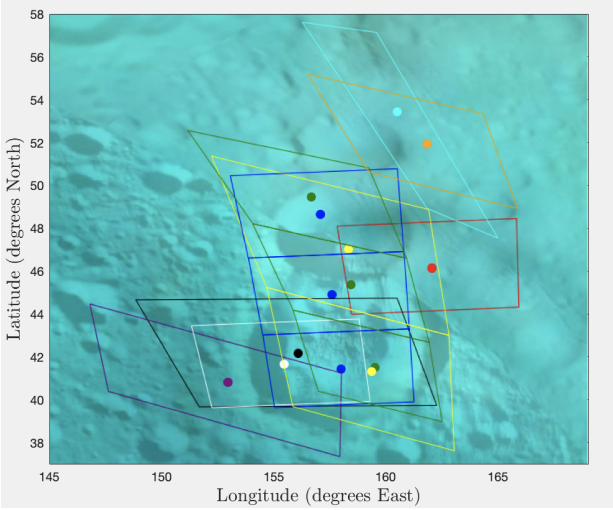

(a) Map of each of the 14 pixels used in the crater region. Each dot represents the location of the center of the pixel and each line represents the outline of the pixel. The color of each dot correlates to the color of the outline of the pixel. Dots with the same color represent pixels from the same flyby.

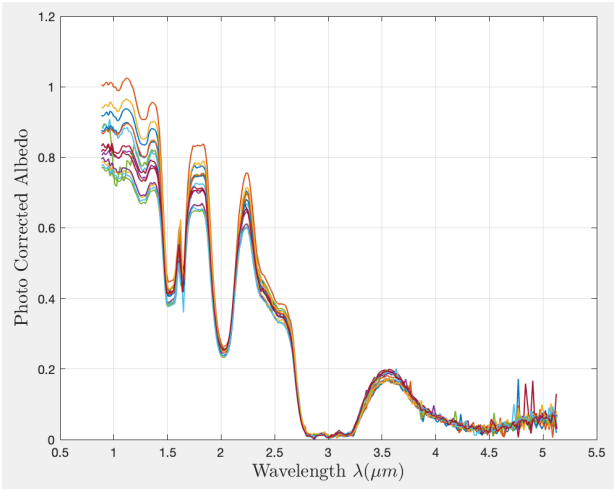

(b) The spectra from the 14 pixels used to find the surface parameters in the crater region.

Figure 53: Shows the location, size, and spectra for each of the 14 pixels used in the crater region.

The process of the formation of the craters on the surface of Enceladus will help explain trends found in the parameters. Figure 54 shows the steps in the formation of a crater. This figure will be referred to throughout the crater section to help explain the processes that occurred and why the parameters show certain trends.

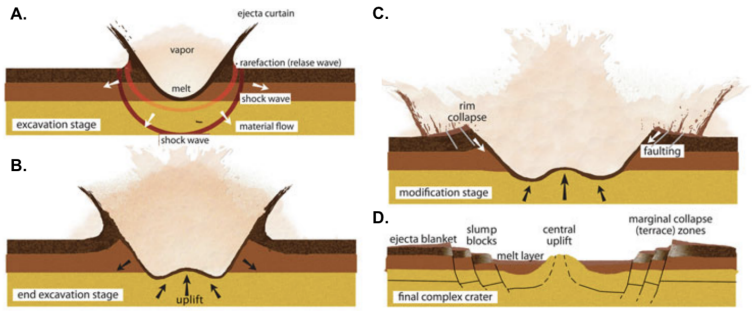

Figure 54: The four major steps in crater formation. Step (A) shows material being thrown from the impact site which is a bowl-shaped indentation in the surface. Step (B) shows the bowl shape progressing into a larger crater shape as the surface below rebounds back upwards. Step (C) shows the ejected materials begin to descend back to the surface and the rebounded materials below begin to form the central peak of the crater. Step (D) shows the final structure with the ejected material returned to the surface, the central peak, melt layer, and collapsed edges of the crater. [52]

6.3.1 Grain Size

Figure 55b shows the average diameter of the grains within the pixel. The center of each pixel is represented with a dot, and the color represents the different average sizes of the grains in that region. The first pair of dots that will be compared are the two dots around $52°N$ and $161°E$. These dots are shown in Figure 55a by the orange and cyan-colored dots. The cyan-colored pixel covers

more surface outside of craters than the orange-colored pixel, and the orange-colored pixel covers a larger region within the crater. The orange-colored pixel has a lower average grain size than the cyan-colored pixel as shown in Figure 55. The red pixel seen in Figure 55a has a grain size diameter in between the orange and cyan-colored pixels. The red pixel has more coverage inside the crater than the cyan pixel but less coverage inside the crater than the orange pixel. This trend can also be seen when comparing pixel colors white and black in Figure 55a. The majority of the black pixel coverage is within the largest crater. The black pixel has a low average grain size compared to the white pixel. The coverage of the white pixel is divided between being in and out of the large crater. The larger grain size of the white pixel is due to having more of its coverage outside of the crater and in the undisturbed surface region. The pixels with more coverage inside the craters have a lower average grain diameter size than the pixels with more coverage outside the craters. The lower grain size is caused by the extreme events that occurred during the impact which formed the crater shown in Figure 54. The grains are smaller because, during the impact when the plume of debris is formed, the flash freezing at low temperatures forms smaller grain sizes [53]. The plume debris mostly falls within the crater which is why the grain sizes here have a smaller diameter.

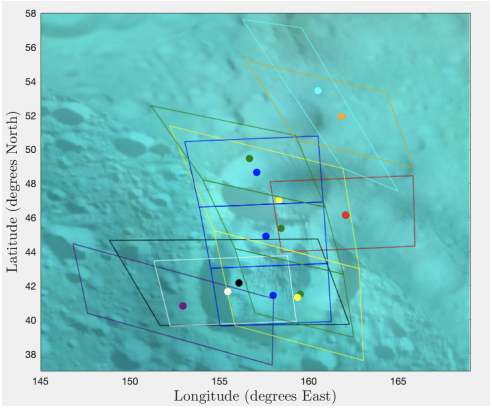

(a) Map of the 14 pixels used in the crater region. Each dot represents the center of the pixel, and each box represents the surface covered by the pixel.

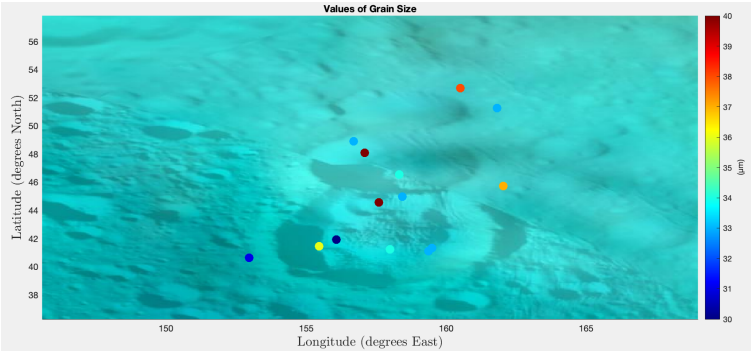

(b) Map of the crater region which shows the different grain sizes in the region. The diameters of the grain sizes are shown in μm.

Figure 55: Showing the grain size and pixel location for the crater region.

6.3.2 Filling Factor, ϕ

As previously stated, the larger the filling factor value, the less porous the surface is. It is expected that regions with smaller grain sizes to be less porous. This relationship between grain size and porosity is intuitive since particles with smaller diameters would be able to pack closer together and become denser than particles with larger grain sizes. Figure 56a shows an example as to why materials with larger grain diameters have more empty space than materials with smaller grain diameters. Therefore, it is expected that the region within the crater would have a larger filling factor value than regions outside of the craters. This trend can be seen in Figure 56c. Again, comparing the orange, cyan, and red pixels from Figure 56b, the filling factor trends can be seen. The orange pixel has the most coverage inside the crater followed by the red and then cyan-colored pixels. The orange pixel has the highest filling factor value of the three pixels, followed by the red and then by the cyan-colored pixels. When comparing the black and white-colored pixels, the black pixel has a higher filling factor than the white pixel. This is because the black pixel has more coverage within

the crater than the white pixel, therefore, has a higher average surface density. The cause of the high surface density within the craters is the reduction of grain size that occurred during the impact. The smaller diameters of the grains allow for them to be closer together and form a denser surface.

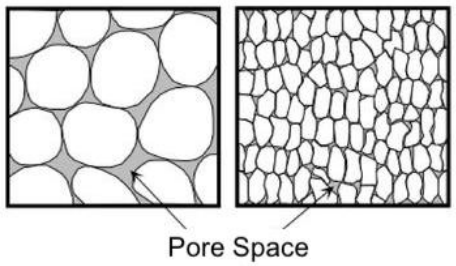

(a) Shows why larger grain sizes have a lower filling factor than small grain sizes. Larger grains can not fit together as efficiently and they leave more gaps in the material.

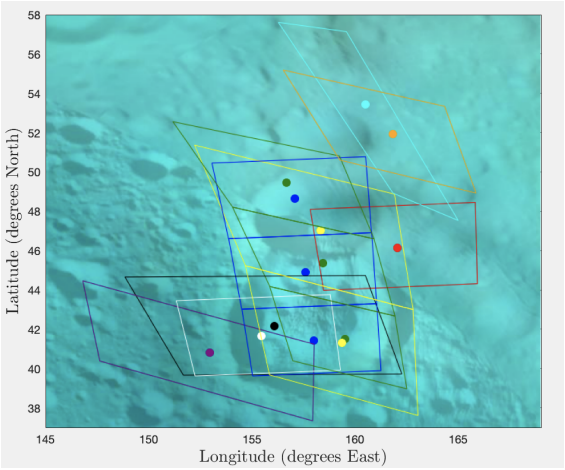

(b) Map of the 14 pixels used in the crater region. Each dot represents the center of the pixel, and each box represents the surface covered by the pixel.

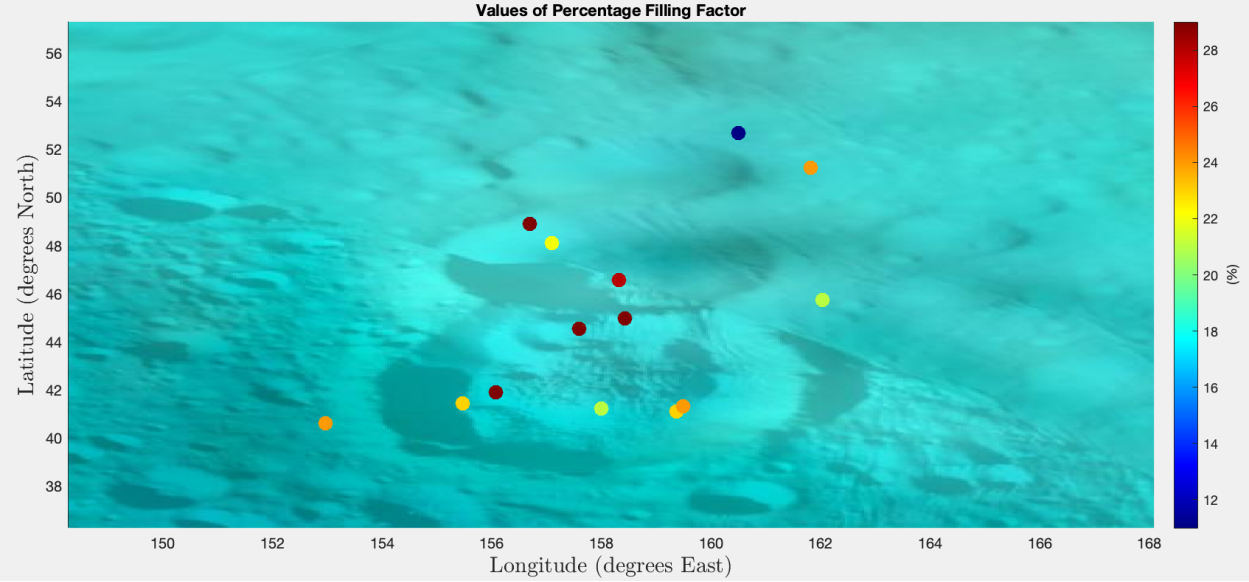

(c) Map of the crater region that shows the different filling factor percentages in the region. The filling factor is a value between 1 and 0 which correlates to the percentage of space in a given volume that is taken up by the material.

Figure 56: Showing the filling factor and pixel location for the crater region.

6.3.3 Surface Roughness, $\bar{\theta}$

The surface roughness values for the crater region range from 28° to 37°. These values are expected in this region due to the uneven slopes in the surface created by the craters. Due to the low resolution and large surface coverage of the pixels in this region, it is difficult to show trends when looking at the surface roughness. Since the value obtained is the average surface roughness in the pixel region, the low resolution does not allow for precise roughness values. However, it can be seen

that the purple pixel in Figure 57a has a lower average surface roughness than both the black and white pixels. This corroborates that the surface roughness within the crater is larger than in the surrounding regions.

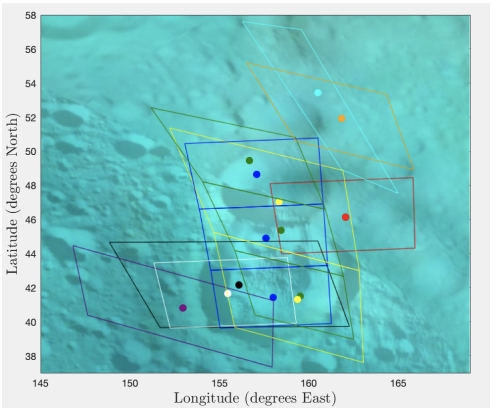

(a) Map of the 14 pixels used in the crater region. Each dot represents the center of the pixel, and each box represents the surface covered by the pixel.

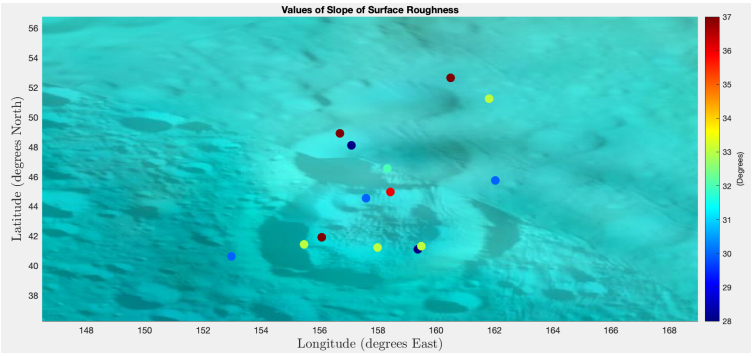

(b) Map of the crater region that shows the different surface roughness's. Theta bar is measured in degrees and is the slope angle of the surface.

Figure 57: Showing the surface roughness and pixel location for the crater region.

6.3.4 Percentage of Crystalline Ice

The crater formation process is crucial in explaining the crystalline variations in and around the crater. In Figure 54 it can be seen that once the crater hits the surface, the heat from the impact causes the ice on the surface to melt and then refreeze. This process will create crystalline ice which will be inside and ejected from the crater [53]. The vapor gas ejected upon impact will flash freeze in the atmosphere and form smaller amorphous grains [53]. Then, the amorphous ice will fall back to the surface of Enceladus. As seen in Figure 54, most of the debris that is ejected from the impact will be hanging over the center of the crater. This allows for the amorphous ice to fall in the center of the crater and the crystalline ice debris to remain outside the crater predominately on the rim.

When comparing the black, white, and purple-colored pixels from Figure 58a, the white-colored pixel covers more of the center of the crater, the black-colored pixel covers more of the rim and surrounding regions than the white-colored pixel, and the purple-colored pixel covers the rim and further surrounding regions. Since the white-colored pixel covers more of the center of the crater, its crystallinity percentage is the lowest of all three. The black-colored pixel covers the most area that is on the rim of the crater which is why its crystallinity percentage is the highest. Lastly, the purple-colored pixel covers a large portion of the rim, but a majority of the pixel is in the region outside the crater which is why the crystallinity percentage is lower than that of the black-colored pixel. When comparing the blue pixels to the green and yellow pixels, the blue pixels have a majority of the pixel surface within the center of the crater. The green and yellow pixels include much more of the rim and outside the region of the crater which is why the percentage of crystalline ice in this region is much higher.

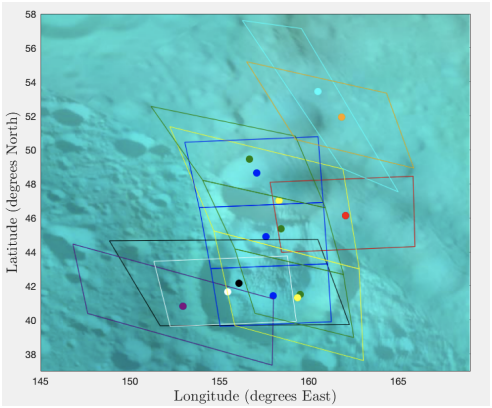

(a) Map of the 14 pixels used in the crater region. Each dot represents the center of the pixel, and each box represents the surface covered by the pixel.

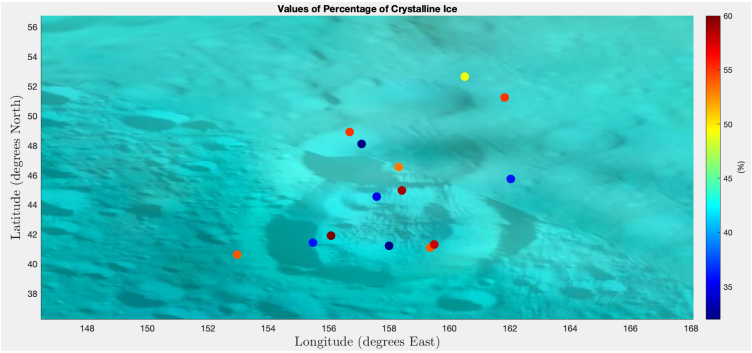

(b) Map of the crater region that shows the different percentages of crystalline ice.

Figure 58: Showing the surface roughness and pixel location for the crater region.

6.3.5 Surface Temperature

Figures 59a and 59b show each of the photometrically corrected spectra overlaid on top of one another and the average of all of the spectra in the 3.2 to 4 μm range. The average spectra are used to allow for the peak of the 14 spectra to be visualized easier. For the crater region, the average 3.6 μm peak for all the locations is 3.5486 μm. Using Equation 7, the approximated deposition temperature of the ice in this region is found to be 64 degrees Kelvin.

The temperature was also found while fitting the spectra with the Hapke model. Figure 59d shows the temperature that produced the best fit for the spectra. The resulting temperature correlates to the temperature of the ice in the laboratory that was used to find the optical constants [43]. The optical constants were found in increments of 20 degrees Kelvin, so the values are not as precise as the linear method used in Equation 7. Half of the points used the optical constants from 60 degrees Kelvin and the other half used the optical constants from 80 degrees Kelvin to find the best fit for the spectra. This implies that the average temperature of this region is between 60 and 80 Kelvin. These values are similar to the results found using the peak of the 3.6 μm value of 64 K.

To summarize the process that occurred during the formation of the crater, the impact melts and ejects debris from the impact location. The ice that is ejected freezes at higher temperatures, and forms large-grained crystalline ice. The impact creates a plume of debris above the crater. The vapor in the plume flash freezes in the cold atmospheric temperature and forms into small-grained amorphous ice. The amorphous ice then falls back to the center of the crater.

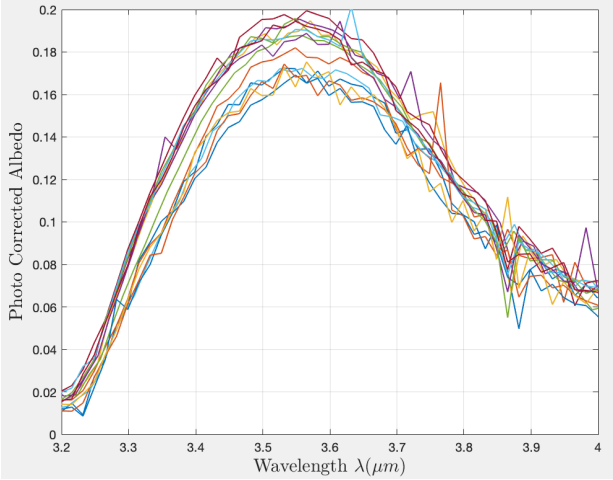

(a) The 14 photometrically corrected spectra from the crater region all plotted on the same plot.

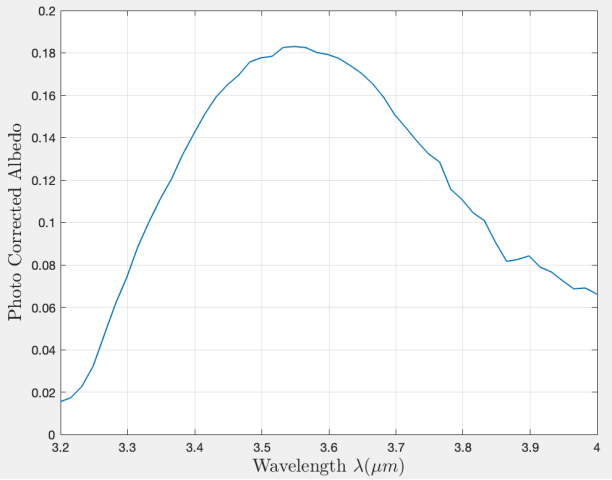

(b) The mean spectra produced from the plot in Figure 59a

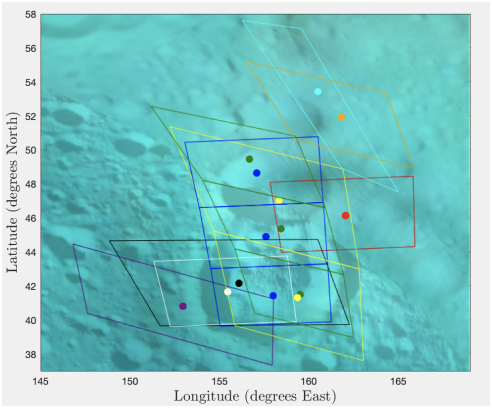

(c) Map of the 14 pixels used in the crater region. Each dot represents the center of the pixel, and each box represents the surface covered by the pixel.

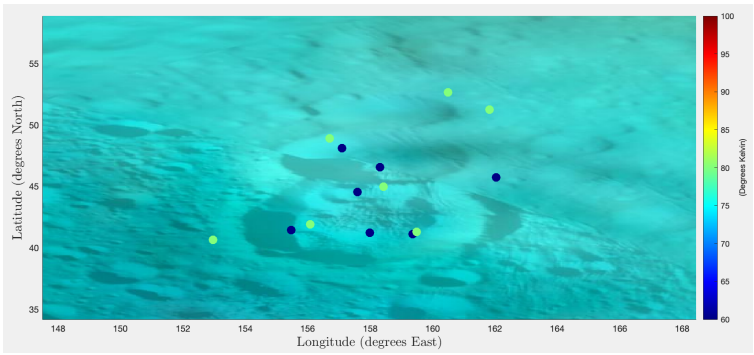

(d) Map of the crater region that shows the temperature of the optical constants used to achieve the best fit.

Figure 59: Surface temperature findings for each of the pixels used in the crater region. Figures 59a and 59b show the 3.6 μm peaks used to calculate the temperature from the spectra. Figure 59c shows the location and surface covered by each pixel. Figure 59d shows the temperature of the optical constants used during the Hapke model to acquire the best fit.

6.4 Tiger Stripes

The region in the southern hemisphere of Enceladus that is located around the pole is known as the tiger stripes. This region is south of the black dashed line on the map in Figure 45 to give a clear representation. This area is of interest since the plumes and large faults are located here. The plumes eject water vapor and cause this region to be covered in fresh ice debris with large grain sizes, and a high percentage of crystalline ice than the surrounding regions [11]. This section will provide the results from fitting the Hapke model to the 14 locations specified in Section 4. Figure 60a shows the locations and the sizes of the pixels used in this region. The average parameters from within these pixels will be found to best fit the spectra from the VIMS data to the spectra produced from the Hapke model. The pixel resolution in this region is much higher than the resolutions from the pixels in other regions. This allows for more precise observations to be taken and discussed.

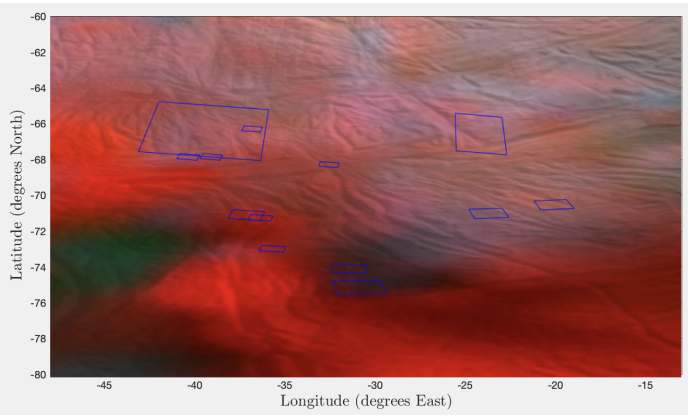

(a) Map of each of the 14 pixels used in the tiger stripes region. The amount of surface each pixel covers is represented by the blue outlines.

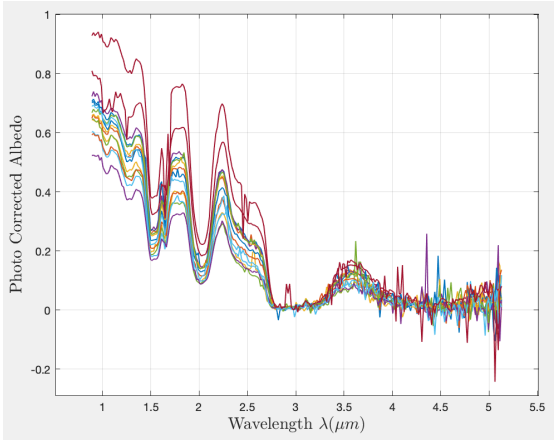

(b) The spectra from the 14 pixels used to find the surface parameters in the tiger stripes region.

Figure 60: Shows the location, size, and spectra for each of the 14 pixels used in the tiger stripes region.

6.4.1 Grain Size

The plumes in the tiger stripe region come from within the large cracks in the surface. The large cracks can be seen at the bottom Figure 61. The closer the position to these cracks, the larger the average grain diameter. The further away from the plumes, the grain size decreases at a rapid rate. The ejected material from the plumes can only travel until a certain distance before reaching the surface; therefore, the further away from the plumes, less debris will fall and the grains will be smaller in size. The larger-sized particles are heavier and will fall to the surface earlier than the smaller particles. The ice on the surface of Enceladus is subjected to collisions from charged particles from space which breaks down the size of the grains over time [54]. This weathering happens at a constant rate, but since the locations closer to the plumes receive more fresh ice debris from the plumes, the ice particles do not spend as much time getting hit by the charged particles. The slower the rate of debris falling in a region means the particles spend more time getting weathered into smaller diameters. Figure 61 shows the grain diameter size in μm. It can be seen that the pixels that overlap show similar grain sizes which proves that the model is working correctly. Pixels close together, but slightly further away from the plumes show a decrease in grain diameter which is expected. The further from the plumes, the smaller the grains are.

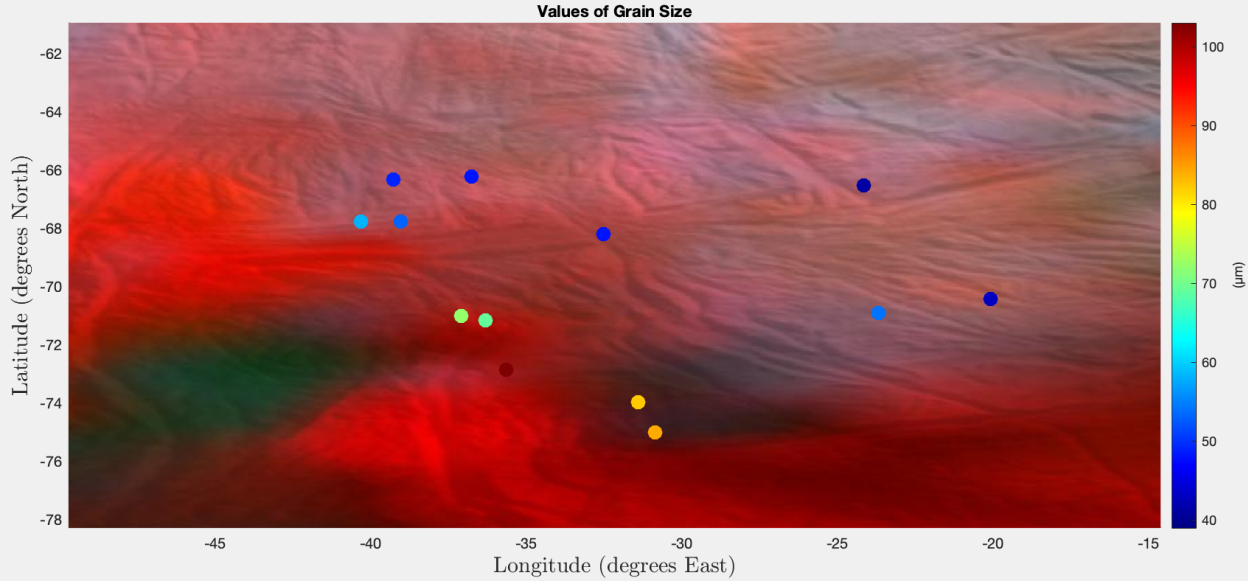

Figure 61: Map of the tiger stripes which shows the different grain sizes in the region. The diameters of the grain sizes are shown in μm.

6.4.2 Surface Roughness, $\bar{\theta}$

Figure 62 shows the surface roughness for the tiger stripes region. This region has very uneven surfaces and cracks in the ice which can be seen in the figure. It can be seen that on locations close to the tiger stripes and other large cracks in the ice, the average surface roughness increases. The uneven surfaces and steep slopes created from these cracks give this region higher surface roughness than the other two regions.

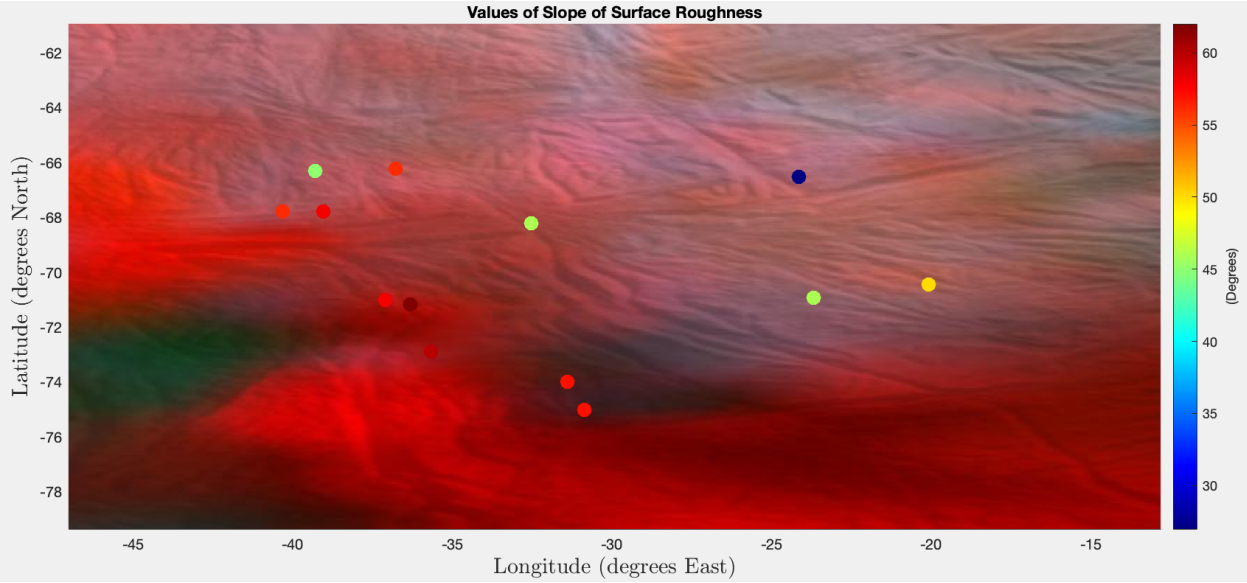

Figure 62: Map of the crater region that shows the different surface roughness's. Theta bar is measured in degrees and is the slope angle of the surface.

6.4.3 Percentage of Crystalline Ice

The plumes in the tiger stripe region come from within the large cracks in the surface. The large cracks can be seen at the bottom Figure 63. The closer the position to these cracks, the higher the percentage of crystalline ice because the icy grains in the plumes are formed at temperatures higher than 140K. The further away from the plumes, the percentage of crystalline ice decreases at a rapid rate. The ejected material from the plumes reaches the surface; therefore, the further away from the plumes, the less debris will fall. Ice on the surface of Enceladus is subjected to collisions from charged particles from space which breaks down the crystalline ice structure and makes the ice more amorphous over time [54]. This weathering happens at a constant rate, but since the locations closer to the plumes receive more crystalline ice debris from the plumes, the ice particles do not spend as much time getting hit by the charged particles. The slower the rate of debris falling in a region means the particles spend more time getting weathered into amorphous ice.

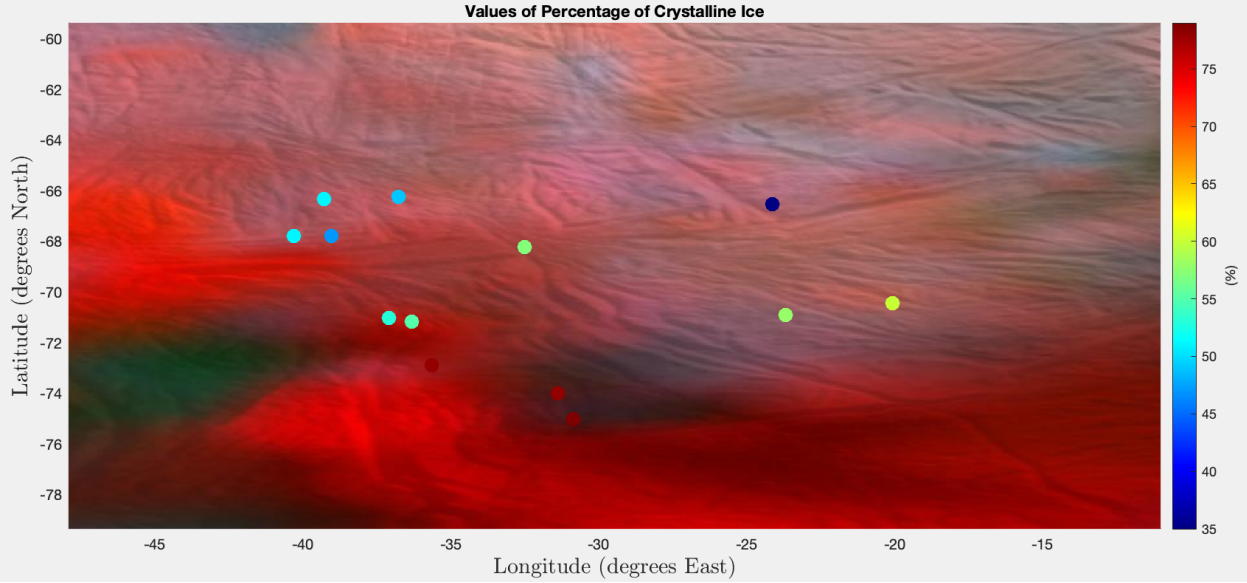

Figure 63: Map of the tiger stripes that shows the different percentages of crystalline ice in the region.

6.4.4 Filling Factor, ϕ

Figure 64a shows the average percentage of the filling factor for each pixel in the tiger stripes region. The higher filling factor percentages are closer to the location of the plumes in the tiger stripes. The filling factor percentages decrease as the location of the pixel gets further away from the plumes. This trend shows that the surface becomes less dense as the distance from the plume increases, with the maximum surface density located closest to the plumes. A reason for this trend could be related to the large change in the percentage of crystalline ice in the region. Figure 64b shows how crystalline ice has a more structured arrangement of the particles than amorphous ice. The structure of crystalline ice could affect the filling factor by allowing denser particles compared to amorphous grains. This could then balance the fact that there should be more porosity for larger grains, and another trend should be observed if the icy grains would have the same characteristics (crystalline or amorphous).

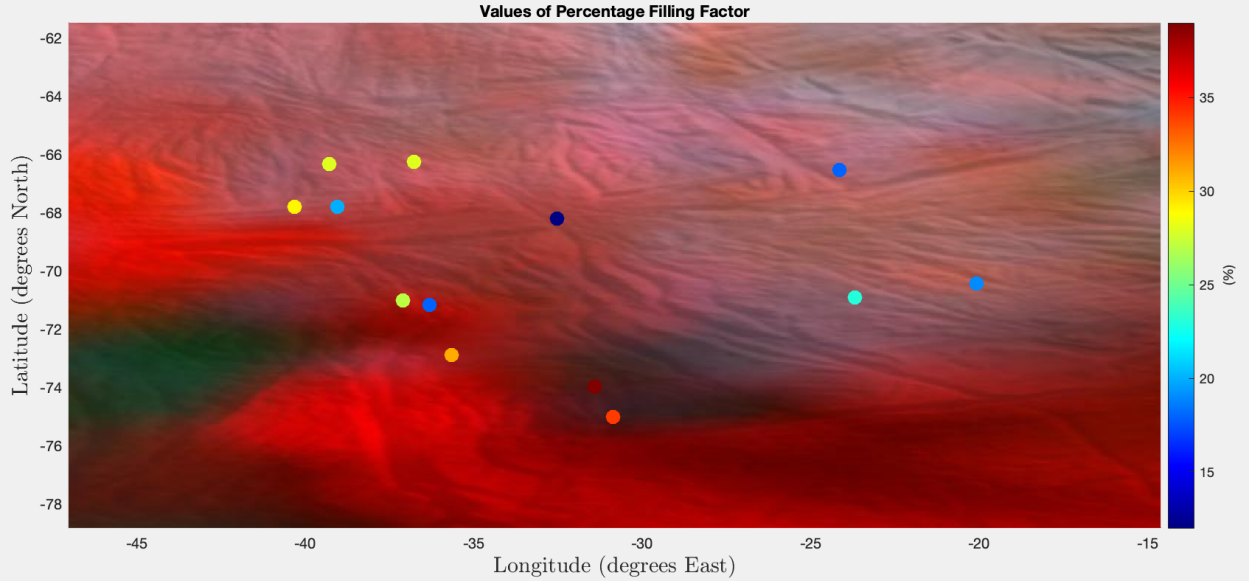

(a) Map of the tiger stripes that shows the different filling factor percentages in the region. The filling factor is a value between 1 and 0 which correlates to the percentage of space in a given volume that is taken up by the material.

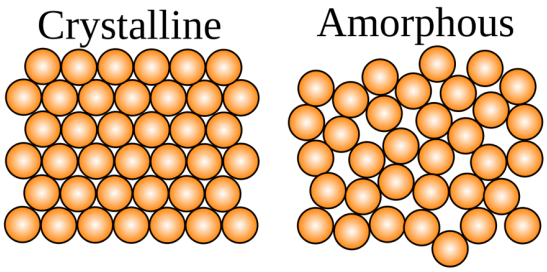

(b) Shows the structure of crystalline ice versus amorphous ice.

Figure 64: Shows the particle arrangement of crystalline and amorphous ice to help explain the trend shown in the values of filling factor found.

6.4.5 Deposition Temperature

Figure 65 shows each of the photometrically corrected spectra overlaid on top of one another and the average of all of the spectra in the 3.2 to 4 μm range. The average spectra are used to allow for the peak of the 14 spectra to be visualized easier. For the tiger stripe region, the 3.6 μm peak is located at 3.5875 μm. Using Equation 7, the approximated deposition temperature of the ice in this region is found to be 95 degrees Kelvin. Figure 65c shows the temperature that produced the best fit for the spectra. The temperature correlates to the temperature of the ice in the laboratory that was used to find the optical constants [43]. The optical constants were found in increments of 20 degrees Kelvin, so the values are not as precise as the linear method used in Equation 7. Nearly all of the points in these regions used the optical constants from 80 degrees Kelvin to find the best fit for the spectra. These values do not match as well to the results found using the peak of the 3.6 μm value as from the red and crater regions. In Figure 65 it is shown that the spectra from this region have much more noise than from the other two regions. This could be a possible reason as to why the temperature does not match as well with the linear method as in the other two regions.

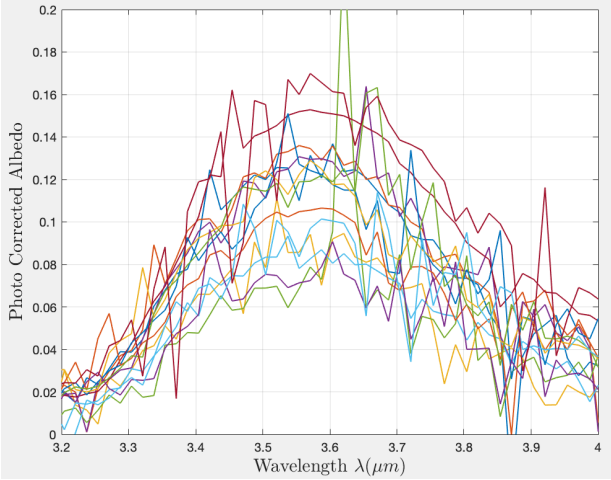

(a) The 14 photometrically corrected spectra from the tiger stripe region all plotted on the same plot.

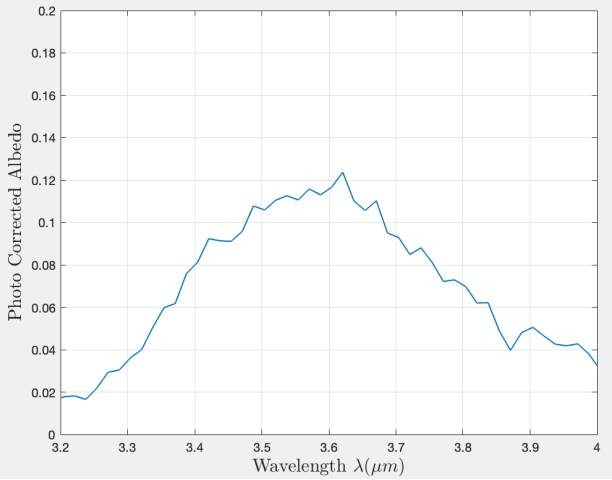

(b) The mean spectra produced from the plot in Figure 65a.

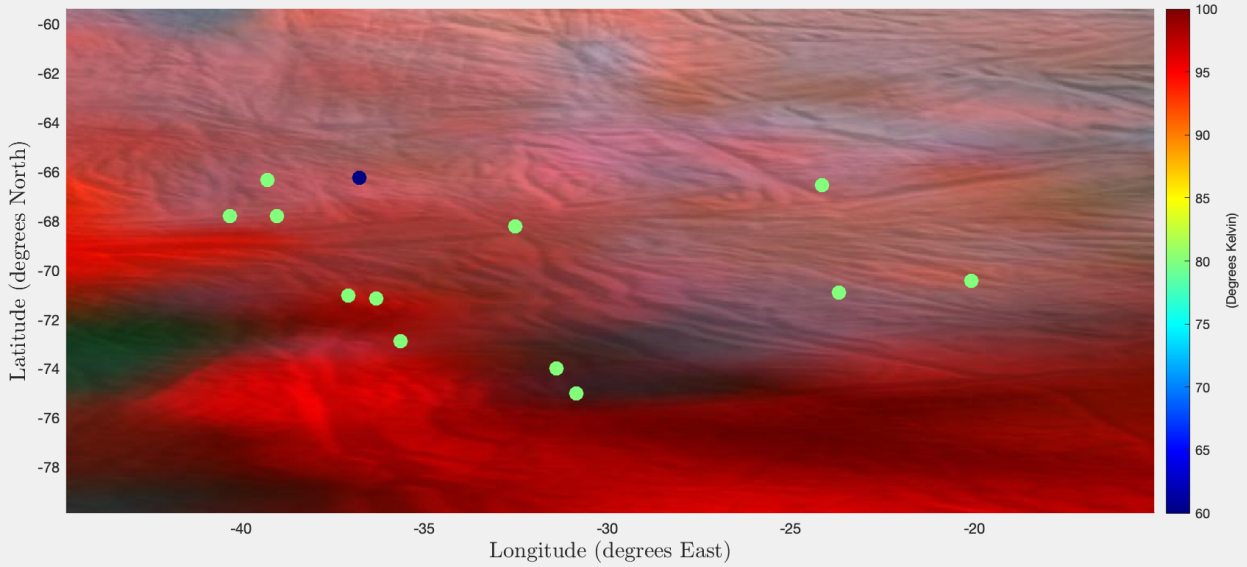

(c) Map of the tiger stripes region that shows the temperature of the optical constants used to achieve the best fit.

Figure 65: Surface temperature findings for each of the pixels used in the crater region. Figures 65a and 65b show the 3.6 μm peaks used to calculate the temperature from the spectra. Figure 65c shows the temperature of the optical constants used during the Hapke model to acquire the best fit.

7 Discussion, Conclusion, and Recommendation

This section will discuss how the results tie together to answer the research question posed in this report and then give recommendations on how to continue this research. The results of the study will be evaluated by comparing each parameter from the different regions of Enceladus. The parameters will give insight into the similarities and differences between each region. These similarities and differences will help conclude why the region around $30°N$ and $90°W$ has different characteristics than the surrounding areas.

7.1 Discussion

7.1.1 Grain Size

The diameter of the grain size greatly affects the reflectance spectra produced from the Hapke model. The size of the grain has such an effect on the reflectance since each it is used to calculate the single scattering albedo. The single scattering albedo is multiplied by every other parameter in Equation 11 to solve for the reflectance. The smaller the grain size, the more compact the grains can fit together in a certain volume. This allows for the surface to be smooth and reflect more light when compared to a surface with larger grains. A surface with larger grain sizes has a more uneven surface which scatters more light resulting in a lower reflectance measurement. This is explained in Section 5.3.1, and is due to the larger grains' capability to absorb more of the light than the smaller grains [55]. It is notable from the results and in Figure 61 that the closer to the plumes, the larger the size of the grains is. This is due to weathering from charged particles breaking down the size of the grains over time [56]. The red zone region has grain sizes that are similar to the region just outside the plume region and much larger than the grains in the crater region. The grains in the red region must have been deposited more recently than the grains in the crater region since the rate of decay from weathering occurs at a constant rate. To deposit new grains, a form of resurfacing must have been occurring within the red zone recently. Convectional currents in the ice bring up warmer ice from below and push down the colder ice from the surface. Figure 67 shows the fracturing and convection of the ice that is believed to be occurring currently in the tiger stripes region. The cracks in the ice are formed from the convectional currents in the ice pulling the ice apart [57]. These phenomena could have also been taking place in the red region, or something at a much slower pace could still be occurring. If this process was happening recently, the ice would have large grains that could have been as large as the ones in the tiger stripes. Over time, these large grains would have been reduced in size by weathering to the size they are today. Another possibility would be that the convection process is still occurring today, just producing grains with smaller sizes than in the tiger stripes region. The slower process would allow the ice to weather away before new ice was cycled up to the surface by the convection process. Both hypotheses would explain the increased grain size in the red region in this study.

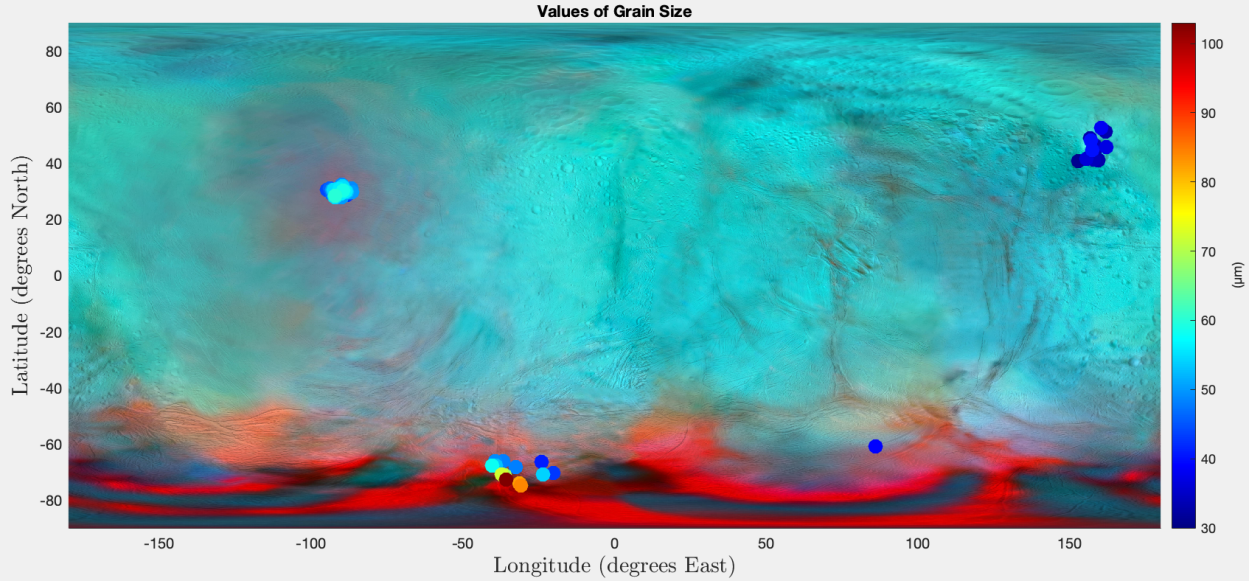

Figure 66: Map showing the grain size diameter in μm for each region.

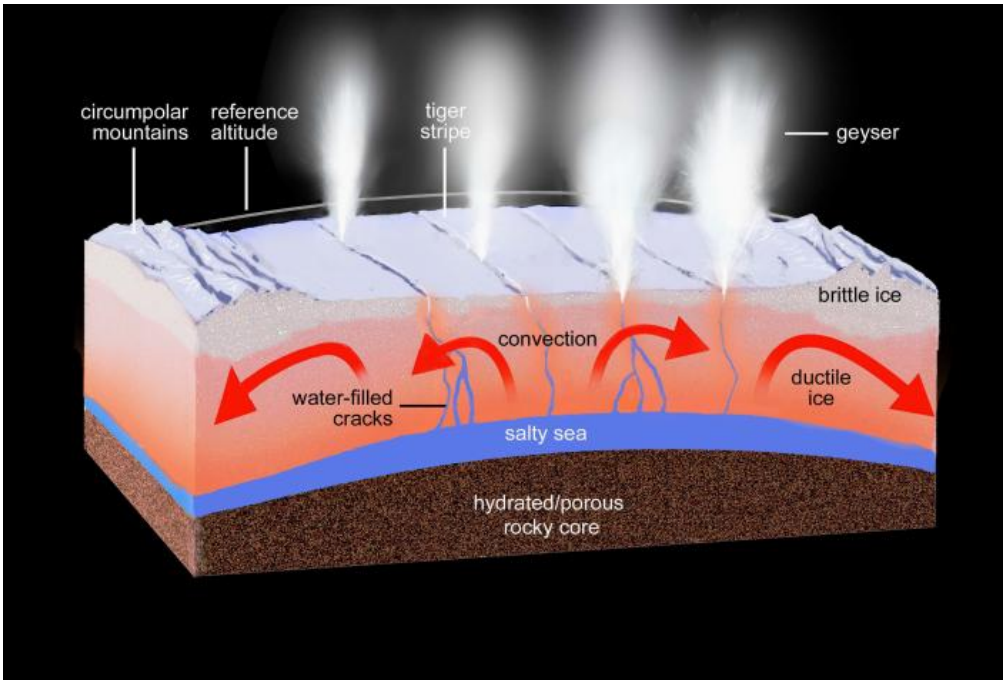

Figure 67: Explaining the convection process that is believed to be the force behind the plumes in the tiger stripes region [57].

7.1.2 Filling Factor, ϕ

The filling factor is related to the porosity of the surface. The filling factor is from zero to one and is related to the porosity, which equals one minus the filling factor. Therefore, the higher the percentage of filling factor, the denser the surface is. The region with the largest range of surface density was the tiger stripe region. It is difficult to see in Figure 68 since the largest value is the dot

in red is placed over all the other points. However, in Figure 49, it can be seen that the majority of the filling factor percentages are lower in the red region than in the tiger stripes region. The filling factor values in the red region and crater region are similar. The large filling factor values in the tiger stripes region could be from the increased density for crystalline ice. Since the structure of the crystalline ice leaves less space between molecules than amorphous ice, the crystalline ice could be the cause for the large filling factor values in the tiger stripes region.

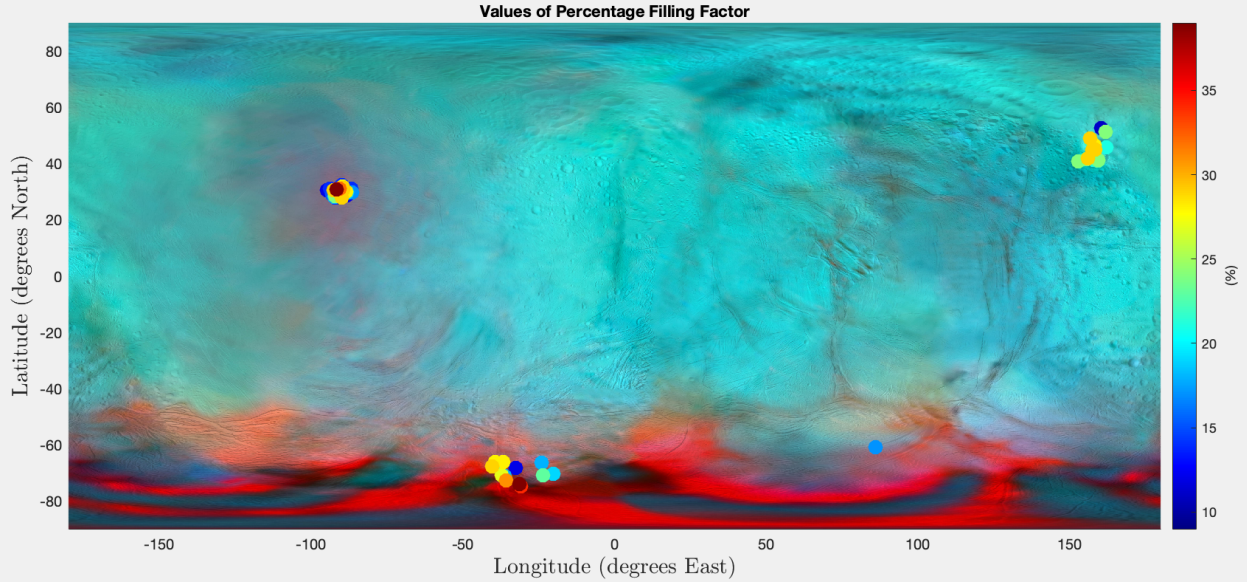

Figure 68: Map showing the filling factor in % for each region.

7.1.3 Surface Roughness, $\bar{\theta}$

The macroscopic slope of the surface is measured by $\bar{\theta}$. The roughness of the surface can drastically change within a couple of meters. The surface could be completely smooth and then a large fault in the ice could appear. For this parameter, the higher the resolution of the observation, the more accurate the results will be. Since the spectra are an average over the entire pixel, unless the pixel has a high resolution, it is difficult to see detailed results. As seen in Section **??**, the crater and red regions only have pixel resolutions of over 10 km/pixel. The tiger stripe region had much higher pixel resolutions due to the increased interest in the region after the plumes were discovered. After the plumes were discovered by the Cassini mission, more flybys of the tiger stripe region which were much closer than previous flybys were performed. The high resolution allows for small changes in the surface roughness to be detected in this region. The values in this region range from 38° to 61°. Another reason for such a large range in roughness in this region is due to the presence of large faults in the unique surface. These large trenches produce high slope angles which allow average surface roughness within the pixel to be larger. Both of these reasons account for why it is clear to see such an important change in surface roughness in the tiger stripe region. The other regions have changes in surface roughness, but since the pixel size is so large and the value is the average over the entire pixel, the values do not change as much as the tiger stripes region from pixel to pixel.

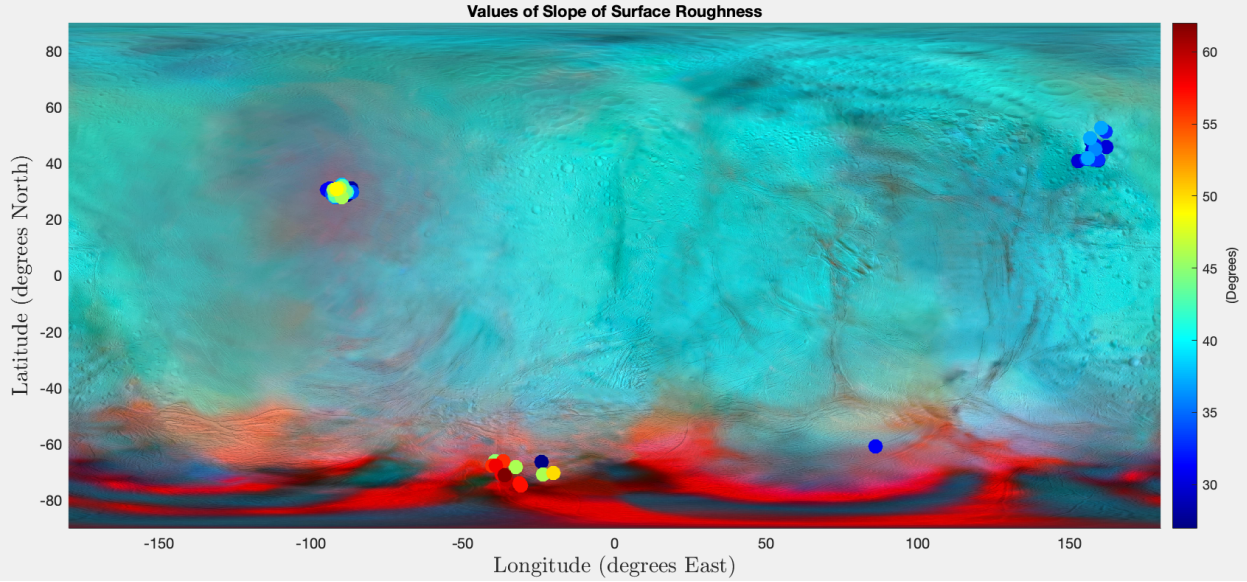

Figure 69: Map showing the surface roughness in °'s for each region.

7.1.4 Percentage of Crystalline Ice

The presence of crystalline ice can easily show a connection between different regions. If the same type of ice is found in specific regions of Enceladus, there must be a connection between the two regions. Crystalline ice is formed at higher temperatures than amorphous ice. Amorphous ice is more commonly found in space due to ice being frozen at such low temperatures. The presence of such high percentages of crystalline ice on the surface of Enceladus means that there is a heat source on the moon that is allowing the ice to freeze at temperatures higher than 140K. The ice that is being ejected from the plumes has been frozen at higher temperatures allowing for the molecules to arrange in a structured order and become crystalline ice. The range of percentages of crystalline ice is 45% to 67% in the red region, 33% to 59% in the crater region, and 35% to 77% in the tiger stripe region. The plumes scatter the crystalline ice near the base of the plumes in the south pole of Enceladus in the tiger stripes region. Since there is a presence of crystalline ice in the red region, there is a process that is allowing for the ice on the surface in this region to have frozen at higher temperatures to form the crystalline ice. Over time, irradiation from charged particles can damage the crystalline ice structure and transform the crystalline ice into amorphous ice [58]. The crystalline ice is detectable on the surface which implies that the ice was formed in this region recently since weathering occurs at a constant rate [54]. The presence of this ice in the red region strengthens the hypothesis in Section 7.1 that resurfacing had either happened or is currently happening in the red region.

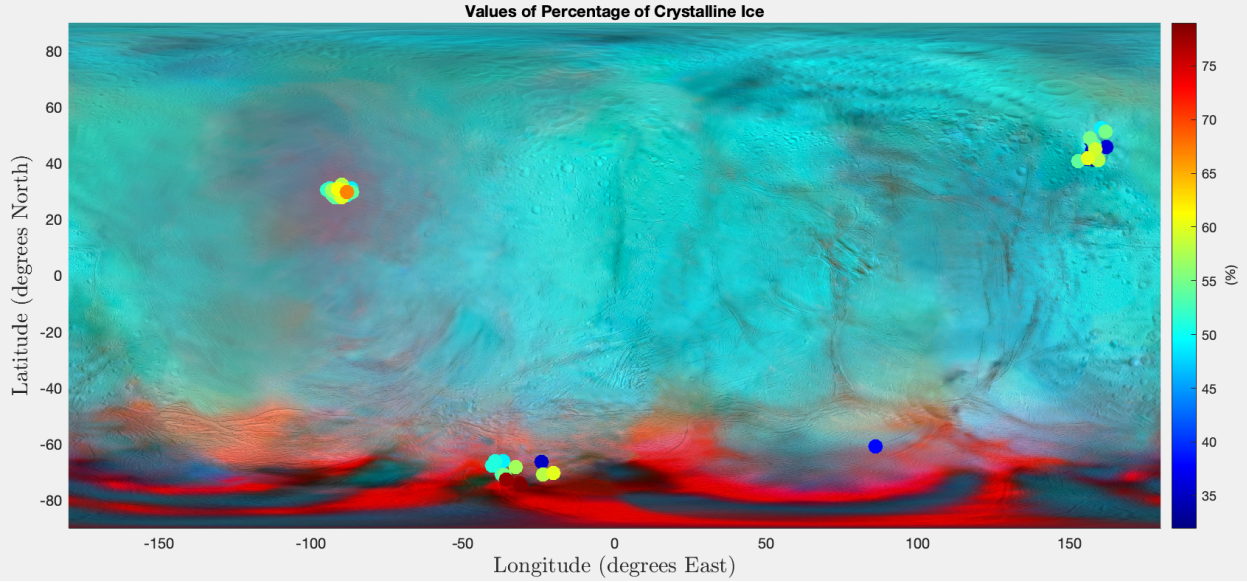

Figure 70: Map showing the percentage of crystallinity in % of crystalline ice for each region.

7.1.5 Surface Temperature

From Section 6, the approximate 3.6μm peaks were 3.5708, 3.5486, and 3.5875 for the red, crater, and tiger stripe regions. These peaks correlate to an approximate temperature of 82, 64, and 95 degrees Kelvin respectively. The crater region has a much lower temperature than the red zone and tiger stripe region. The discovery of plumes in the tiger stripe region proved that Enceladus is an active moon, and there must be internal processes occurring underneath the ice crust that creates heat [57]. This means that the sub-layer underneath the ice must be warmer than the ice on the surface of the moon. Models have shown that the ice layer in the tiger stripes region is thinner compared to the ice layer in other regions of Enceladus [7]. This is the reason that the cracks are able to reach the surface and eject ice particles shown in Figure 67. The combination of a thin ice layer and the warmer crystalline ice depositing on the southern surface of Enceladus could be the reason why this region has a higher surface temperature than the rest of the moon. The red region has a higher surface temperature than the crater region, but not as high as the tiger stripes region. No plumes are depositing the warmer ice on the surface of the red region, so there must be another process heating this region. Resurfacing in the red region from the convection of warm ice would cause the surface to warm slightly. The elevated temperature in the red region could be a result of the resurfacing that took place in this region recently.

7.2 Conclusion

This study has gathered VIMS data from various locations around Enceladus to observe how the surface properties differ at each location. The selection of data was refined to show 63 locations in three different regions: the red region around 30°N and 90°W, the crater region around 45°N and 165°E, and the tiger stripe region located around the southern pole. In previous studies, it was found that high degrees of crystallinity and grain size have been discovered in the tiger stripe region which is attributed to the debris ejecting out of the plumes in the area. The same surface qualities were found in the red region which could not be explained. The purpose of this study was to find an

explanation as to why this trend is found in this region and not in other areas of Enceladus. The results of this study were found by reproducing the spectra found by VIMS data collected during the Cassini mission. This would be accomplished by using the Hapke model of reflectance to change the surface parameters to best fit the spectra found from Cassini. A photometric correction was performed on each spectra to allow comparison between spectra observed at different observation angles. This correction allows for direct comparison between different spectra which allows for more information to be compared. The research questions for this study are repeated as follows:

- What regions on Enceladus have enough VIMS data to make the comparisons?
- What does the infrared spectra of each location tell us about the ice (grain size, density, roughness, crystallinity, temperature)?
- When comparing the regions, what similarities and differences are found, and what does this reveal about the process occurring beneath the ice?
- What trends can be observed locally in the different regions and what can that reveal about the surface?
- Is the anomaly in the northern hemisphere due to plume debris or resurfacing?

The tiger stripe region had a more precise pixel resolution than the other two regions. This allowed for a more detailed analysis of the region. The red and crater region had enough VIMS data to be able to draw conclusions from, but pixels with higher resolution would further advance the study. The results of the infrared spectroscopy for each region are stated again below. The ice grains can be used to understand the icy surface. The grains' size shows a temporal evolution of the surface as well as the evolution from crystalline to amorphous ice. The evolution of the surface could also be explained through the surface temperature of the ice. From the trends found in the parameters of each region, it can be seen that the anomaly in the northern hemisphere known as the red region has undergone resurfacing recently. The exact process occurring in this region is still unknown and would need to be further studied to understand how and why this region of Enceladus is changing.

- Red Region:
  - Show large crystalline grains at the center of the region and smaller amorphous grains further from the center.
  - Has a surface temperature that is closest to the tiger stripes.
- Crater Region:
  - Show small grains of amorphous water ice in the crater and large grains of crystalline water ice on the rim.
  - Has the lowest surface temperature of the three regions.
- Tiger Stripes Region:
  - Show large crystalline grains closest to the plumes and smaller amorphous grains further from the plumes.
  - Has the highest surface temperature of the three regions.

7.3 Recommendation

To further advance this study, a few recommendations and modifications need to be made to improve the study. First, the water optical constants used in this study were composed of only pure crystalline or amorphous water ice. The surface of Enceladus contains impurities that will affect the spectra in ways that the pure ice constants will not be able to fit. Therefore, just using pure water ice optical constants will yield less accurate results. Also, when inputting the parameters into the Hapke model, only the average grain diameter size is taken to make the model easier; however, a model which would allow for a diverse grain size would allow for the fit to be more precise. To improve the photometric correction applied to the data, some of the data points used to derive the equation would need to be filtered out due to their extreme observation conditions. These data points with extreme observation angles affect the phase function derived in Equation 5. This was not done to provide the best resolution and improve the spatial coverage by using more data cubes [11]. However, this has a minor effect on the results of this study when compared to the resolution of the cubes observed. As mentioned previously, the resolution of the pixel that is used to observe a location has a great effect on how detailed the results will be. Pixel resolution was not an issue in the tiger stripe region, as this area was greatly observed with high pixel resolution. To further advance this study, more data would need to be collected at higher resolutions of other areas to enhance the specificity of the results. Since the plumes in the southern hemisphere were of most interest to the Cassini mission, it makes sense that this region had the closest flybys.

8 Validation

In this section, the main methods used to obtain the different results will be validated by comparing them with research that was previously completed. The validation of the major tools and results in this study will help prove that the methods were accurate and allow for a higher degree of confidence. The four parts of this study that will be validated are the photometric correction from Section 4.2, the Hapke model from Section 5, the crystallinity and grain size results, and the deposition temperature results from Section 6.

8.1 Photometric Correction

The photometric correction explained in Section 4.2 was used in this study to be able to compare spectra collected from the Cassini mission taken at different observation angles. Without this correction being applied, the spectra taken from different flybys would not be able to be compared. Figure 71 below shows the example correction that was completed in this study to describe how the correction changes the spectra.

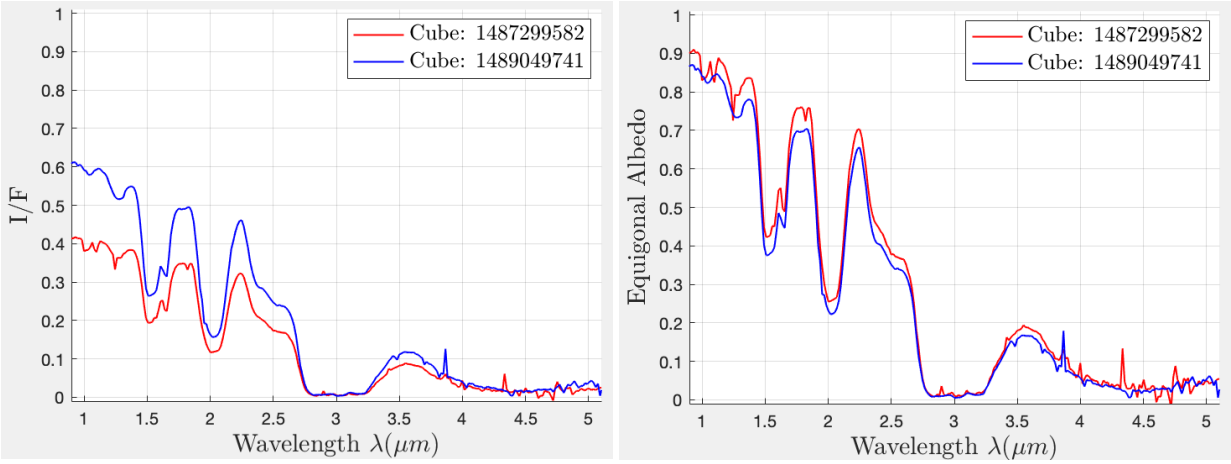

(a) Plot $\frac{I}{F}$ vs. wavelength for the two data cubes using VIMS data.

(b) Plot of the equigonal albedo vs. the wavelength for the two data cubes.

Figure 71: The red spectrum corresponds to cube 1487299582 located at 20.92°N, 85.74°E ($i = 71°$, $e = 48°$, and $g = 26°$). The blue spectrum corresponds to cube 1489049741 located at 24.81°N, 86.80°E ($i = 51°$, $e = 65°$, and $g = 45°$).

The results found in this study matched the findings completed in the study performed by Robidel et al. (2020) [11]. The same photometric correction was used to study the surface of Enceladus. In Figure 72, the corrected spectra and corrected cube data from Robidel's paper are shown. The spectra before and after match closely with the example that was performed in this study. These results validate that the correction being used in this study are accurate.

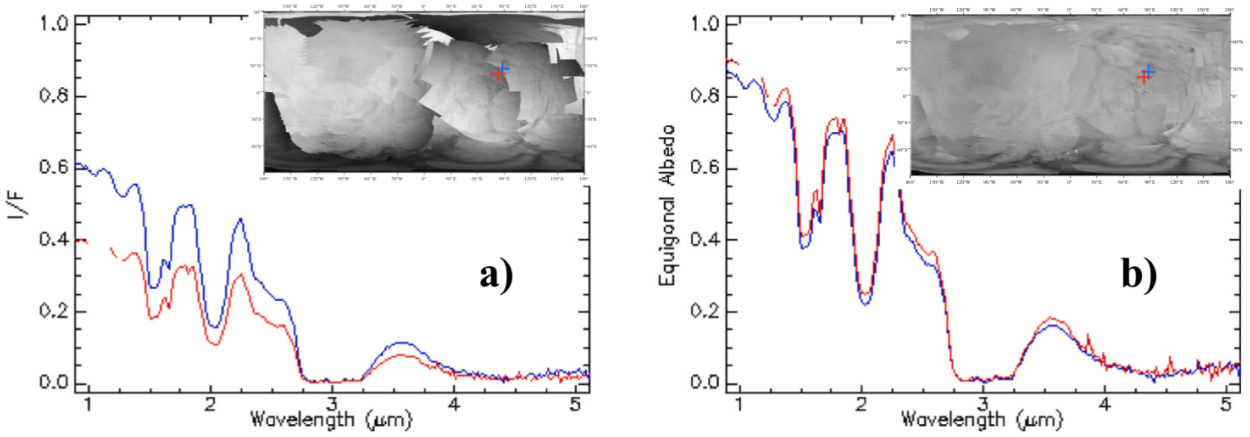

Figure 72: Spectrum comparison before (a) and after (b) the photometric correction performed by Robidel [11]. The red spectrum corresponds to the red cross at 22.5°N and 85°E ($i = 72°$, $e = 49°$, and $\alpha = 26°$) and the blue spectrum corresponds to the blue cross at 23.5°N and 88°E ($i = 50°$, $e = 65°$, and $\alpha = 45°$). [11]

Figure 73 shows the fit from the Hapke model for data that has been corrected (Figure 73a) and data that has not been corrected (Figure 73b). The parameters extracted from the fit of the Hapke model will not change due to the photometric correction applied to the data. Since the correction applies equally to each wavelength, the intensity of each peak and valley will not change relating to the entire spectra.

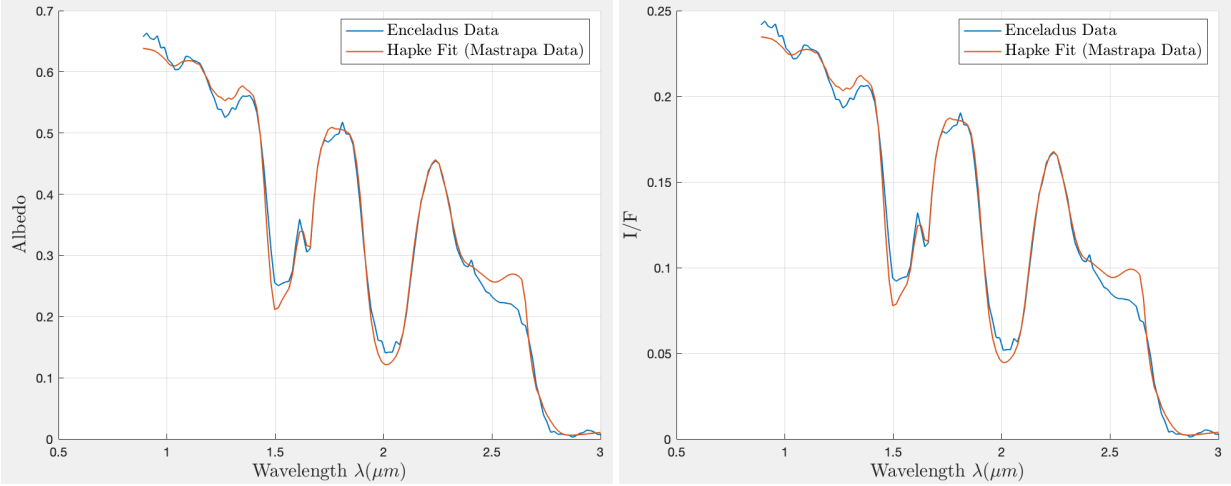

(a) Plot of the equigonal albedo (photometrically corrected) vs. the wavelength for pixel number 10 from the tiger stripes.

(b) Plot of the raw VIMS data ($\frac{I}{F}$) vs. wavelength for pixel number 10 from the tiger stripes.

Figure 73: Figure showing how the photometric correction does not change the fit parameters for the Hapke model.

8.2 Hapke Model

The next model that had a major role in this study was the Hapke model which was described in Section 5. This model was used to calculate the surface parameters in each region observed. Validating this model to previous studies is of high importance because of how crucial the accuracy of this model is. Figure 74a shows the relationship performed in this study between the average

grain diameter and the reflectance. The grain size diameter is an input into the Hapke model and changing this value will change the reflectance intensity at different wavelengths. Figure 74b shows the same trend that changing the grain size has on the reflectance using the Hapke model in a study completed by Raponi [59]. The same model was used in the Raponi study as in this study and the same trends are observed in both plots.

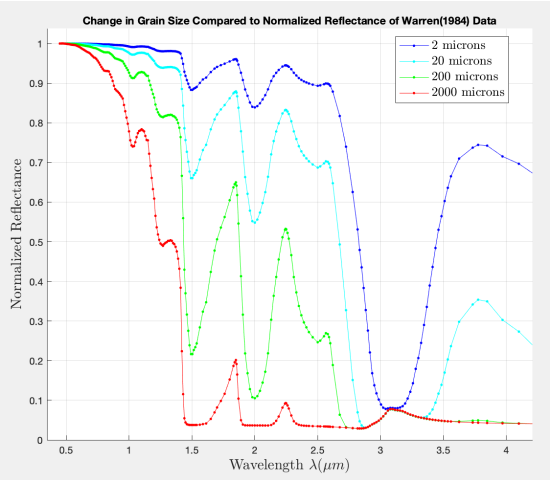

(a) Change in the normalized reflectance based on different grain sizes over the wavelengths below 4.2 μ*m*. This plot was made during this study to test the results found using the Hapke model.

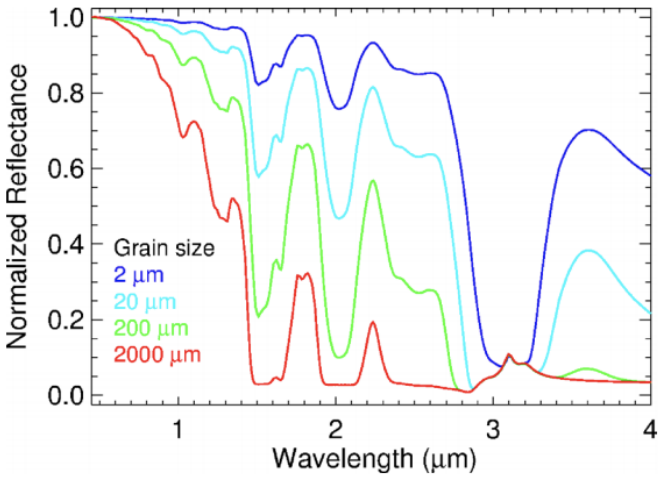

(b) Results from Raponi using the Warren (1984) optical constants to perform the Hapke model for water ice. [59]

Figure 74: Validating the Hapke model results by comparing how changing the mean particle size affects the reflectance by using the optical constants for water ice found in Warren (1984).

8.3 Crystallinity and Grain Size

In the study performed by Robidel, the finalized mosaic of Enceladus showed the locations of high crystallinity and grain size. The results of this study will be compared to the results in the Robidel study to verify that the results show the same trend. Figure 45 below is the mosaic from Robidel's study [11]. The deeper the red colors represent the high values of crystallinity and grain size. The more blue the surface is the lower the crystallinity and grain size. The mosaic shows deep red coloration around the tiger stripes, a medium amount of red coloration in the red zone, and no red visible in the crater region. This trend can be observed in the results of this study as well. The tiger stripes have the highest values of crystallinity and grain size, next to the red zone, and finally, the lowest amount in the crater region. The trend was further discussed in the conclusion in Section 7.1.

In a study conducted by Filacchione in 2010, it was found that ice in a pure amorphous phase has an absorption band exactly at 2.00 μ*m* and ice in a pure crystalline phase has an absorption band at 2.05 μ*m* [60]. This slight shift in the 2.00 μ*m* absorption can confirm the presence of crystalline ice. This shift in absorption band is too slight to find an exact value and was deemed too unreliable to determine a precise value of the percentage of crystalline ice. However, it can confirm an approximation of crystalline ice. Figure 75 below shows the overlaid spectra for each region around the 2.00 μ*m* region. It can be seen that the minimum for each of these regions does not fall at 2.00 μ*m* or 2.05 μ*m*, but somewhere in the middle. This is reflected in the percentages found using the Hapke model since there is a mix of crystalline and amorphous ice.

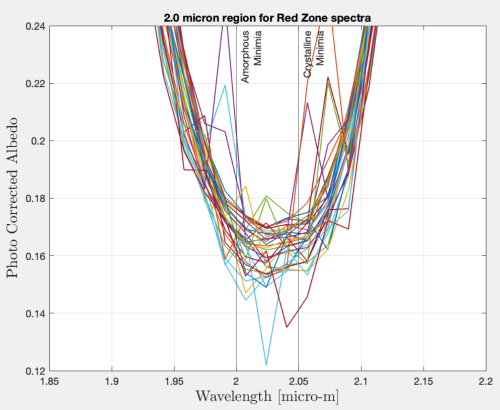

(a) All 35 spectra from the red region focused on the 2 μm wavelength region.

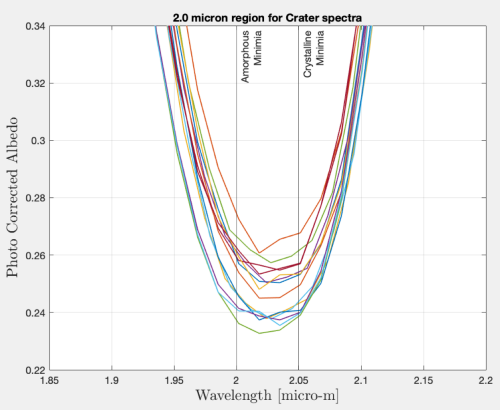

(b) All 14 spectra from the crater region focused on the 2 μm wavelength region.

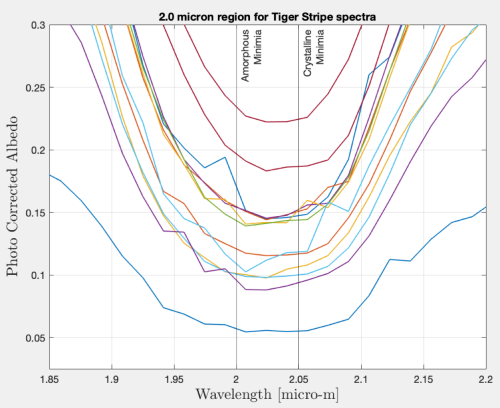

(c) All 14 spectra from the tiger stripe region focused on the 2 μm wavelength region.

Figure 75: Observing the 2 μm region of all the spectra. The slight shift in the absorption minimum at this wavelength can be used to determine the percentage of crystalline ice [60].

8.4 Surface Temperature

The surface temperature results will be compared to similar results concluded by Filacchionne in 2016 [13]. The results of this study showed the 3.6 μm peak from different locations on the surface of Enceladus. Figure 76 shows the plots produced from Filacchionne (2016) which show the calculated 3.6 μm peak positions for locations on Enceladus. For the red zone region around $30°N$ and $90°W$, this study concluded that the 3.6 μm peak was located at 3.5708 μm. The study from Filacchionne also concluded that this region had an approximate peak value of 3.57 μm.

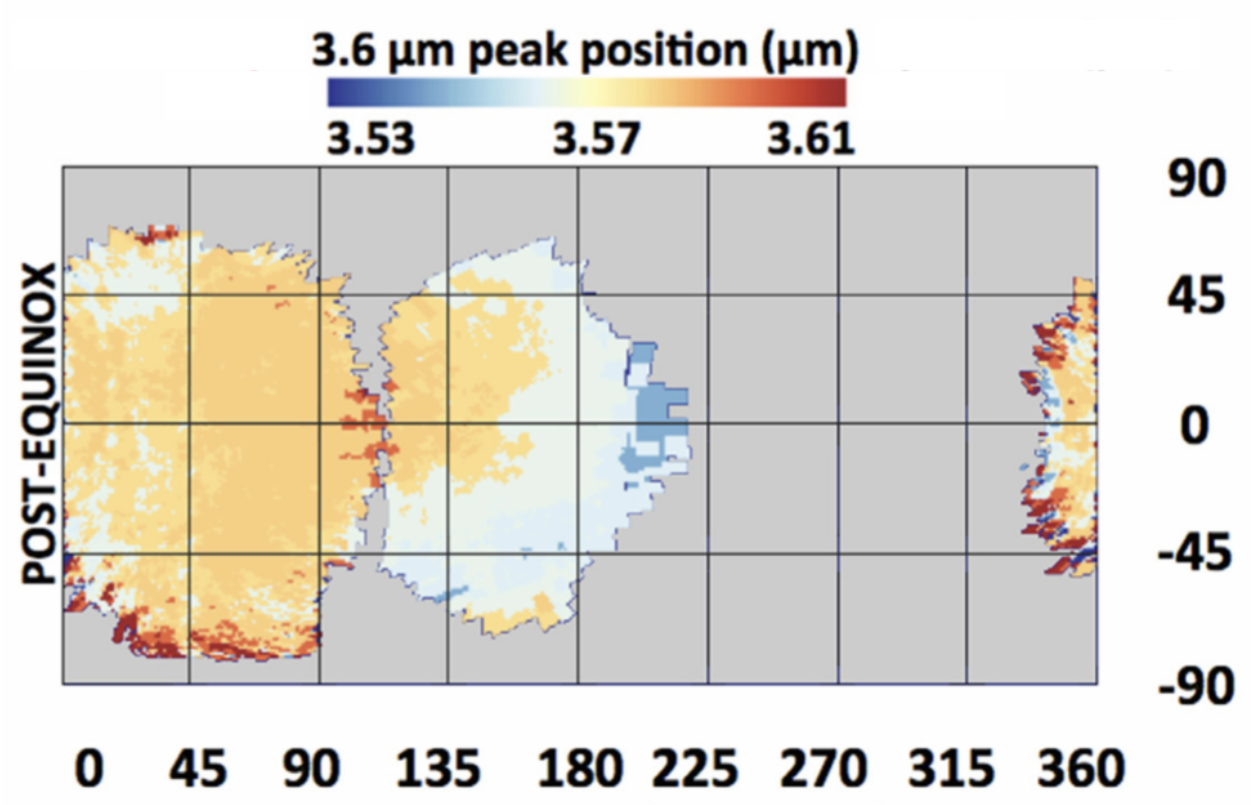

Figure 76: Post-equinox temperature map showing the different deposition temperatures of water ice on the surface of Enceladus. The latitude on this map is the same orientation as the latitude used throughout this study; however, the longitude differs. 0° on this map correlates to 180°W, 180° correlates to 0°, and 360° correlates to 180°E.

References

[1] Canup, R. M., "Origin of Saturn's rings and inner moons by mass removal from a lost Titan-sized satellite," *Nature*, Vol. 468, No. 7326, 2010, pp. 943–946.

[2] Porco, C. C., "Cassini Imaging Science: Initial Results on Saturn's Rings and Small Satellites," *Science*, Vol. 307, No. 5713, 2005, pp. 1226–1236.

[3] Tiscareno, M. S., "Planetary Rings," *Planets, Stars and Stellar Systems*, 2013, pp. 309–375.

[4] Ling, S. J., Sanny, J., and Moebs, W., *University Physics Volume 1*, OpenStax, 2016.

[5] Hubbard, W. and Buratti, B., "The ring system," Apr 2020, https://www.britannica.com/place/Saturn-planet/The-ring-system.

[6] Spencer, J., Nimmo, F., Ingersoll, A. P., Hurford, T. A., Kite, E. S., Rhoden, A. R., Schmidt, J., and Howett, C. J. A., "Plume Origins and Plumbing (Ocean to Surface)," *Enceladus and the Icy Moons of Saturn*, 2018.

[7] Nimmo, F., Barr, A. C., Běhounková, M., and Mckinnon, W. B., "Geophysics and Tidal-Thermal Evolution of Enceladus," *Enceladus and the Icy Moons of Saturn*, 2018.

[8] Postberg, F., Clark, R., Hansen, C., Coates, A., Dalle Ore, C. S., Scipioni, F., Hedman, M., and Waite, J., "Plume and Surface Composition of Enceladus)," *Enceladus and the Icy Moons of Saturn*, 2018.

[9] Nimmo, F. and Pappalardo, R. T., "Ocean worlds in the outer solar system," *Journal of Geophysical Research: Planets*, Vol. 121, No. 8, 2016, pp. 1378–1399.

[10] Patterson, G. W., Kattenhorn, S. A., Helfenstein, P., Collins, G. C., and Pappalardo, R. t., "The Geological History of Enceladus," *Enceladus and the Icy Moons of Saturn*, 2018.

[11] Robidel, R., Mouélic, S. L., Tobie, G., Massé, M., Seignovert, B., Sotin, C., and Rodriguez, S., "Photometrically-corrected global infrared mosaics of Enceladus: New implications for its spectral diversity and geological activity," *Icarus*, Vol. 349, 2020, pp. 113848.

[12] Newman, S. F., Buratti, B., Brown, R., Jaumann, R., Bauer, J., and Momary, T., "Photometric and spectral analysis of the distribution of crystalline and amorphous ices on Enceladus as seen by Cassini," *Icarus*, Vol. 193, No. 2, 2008, pp. 397–406.

[13] Filacchione, G., D'Aversa, E., Capaccioni, F., Clark, R. N., Cruikshank, D. P., Ciarniello, M., Cerroni, P., Bellucci, G., Brown, R. H., Buratti, B. J., and et al., "Saturn's icy satellites investigated by Cassini-VIMS. IV. Daytime temperature maps," *Icarus*, Vol. 271, 2016, pp. 292–313.

[14] ESA, "Navigation," Sep 2019, https://sci.esa.int/web/cassini-huygens/-/34954-instruments?section=vims-visib

[15] ESA, "Navigation," Sep 2019, https://sci.esa.int/web/cassini-huygens/-/33415-summary.

[16] Kohlhase, C. and Peterson, C., Nov 1997, https://www.esa.int/esapub/bulletin/bullet92/b92kohlh.htm.

[17] ESA, "Navigation," Sep 2019, https://sci.esa.int/web/cassini-huygens/-/31240-getting-to-saturn.

[18] Peplow, M., "New moons for Saturn," *Nature*, 2004.

[19] "Catalog Page for PIA21923," Jul 2018, https://photojournal.jpl.nasa.gov/catalog/PIA21923.

[20] NASA, "Cassini at Enceladus: A Decade-Plus of Discovery – NASA Solar System Exploration," Sep 2018, https://solarsystem.nasa.gov/news/12916/cassini-at-enceladus-a-decade-plus-of-discovery/.

[21] NASA, "Overview," Sep 2018, https://solarsystem.nasa.gov/missions/cassini/science/overview/.

[22] Papadopoulos, L., "All Good Things: Countdown Begins Toward Cassini's 'Grand Finale' Around Saturn," Apr 2016, https://www.americaspace.com/2016/04/29/all-good-things-countdown-begins-towards-cassinis-grand-finale-a

[23] ESA, "Navigation," Sep 2019, https://sci.esa.int/web/cassini-huygens/2085-objectives.

[24] Brown, R. H., Baines, K. H., Bellucci, G., Bibring, J.-P., Buratti, B. J., Capaccioni, F., Cerroni, P., Clark, R. N., Coradini, A., Cruikshank, D. P., and et al., "The Cassini Visual And Infrared Mapping Spectrometer (Vims) Investigation," *Space Science Reviews*, Vol. 115, No. 1-4, 2004, pp. 111–168.

[25] Agency, E. S., "Cassini instruments," https://www.esa.int/Science_Exploration/Space_Science/Cassini-Huygen

[26] Spencer, J. R., Barr, A. C., Esposito, L. W., Helfenstein, P., Ingersoll, A. P., Jaumann, R., Mckay, C. P., Nimmo, F., and Waite, J. H., "Enceladus: An Active Cryovolcanic Satellite," *Saturn from Cassini-Huygens*, 2009, pp. 683–724.

[27] Jennings, D. E., Flasar, F. M., Kunde, V. G., Nixon, C. A., Segura, M. E., Romani, P. N., Gorius, N., Albright, S., Brasunas, J. C., Carlson, R. C., and et al., "Composite infrared spectrometer (CIRS) on Cassini," *Applied Optics*, Vol. 56, No. 18, 2017, pp. 5274.

[28] ESA, "Navigation," Sep 2019, https://sci.esa.int/web/cassini-huygens/-/34954-instruments?section=cirs-compo

[29] Liddle, A., *An introduction to modern cosmology*, Wiley, 2015.

[30] Azumi, T. and Matsuzaki, K., "What Does The Term "vibronic Coupling" Mean?" *Photochemistry and Photobiology*, Vol. 25, No. 3, 1977, pp. 315–326.

[31] Sathyanarayana, D. N., *Vibrational spectroscopy: theory and applications*, New Age International, 2004.

[32] Stuart, B. H., "Infrared Spectroscopy: Fundamentals and Applications," *Analytical Techniques in the Sciences*, 2004.

[33] Smith, K. and Newnham, D., "Near-infrared absorption spectroscopy of oxygen and nitrogen gas mixtures," *Chemical Physics Letters*, Vol. 308, No. 1-2, 1999, pp. 1–6.

[34] Morison, I., *Introduction to astronomy and cosmology*, Wiley, 2008.

[35] "PDS Imaging Node Home Page," https://pds-imaging.jpl.nasa.gov/.

[36] "Cassini Vims Data Portal," https://vims.univ-nantes.fr/.

[37] Le Mouélic, S., Cornet, T., Rodriguez, S., Sotin, C., Seignovert, B., Barnes, J., Brown, R., Baines, K., Buratti, B., Clark, R., and et al., "The cassini vims archive of Titan: From browse products to global infrared color maps," *Icarus*, Vol. 319, 2019, pp. 121–132.

[38] Seignovert, B., "Notebook on nbviewer," https://nbviewer.org/github/seignovert/pyvims/blob/master/pyvims.ip

[39] Filacchione, G., Ciarniello, M., D'Aversa, E., Capaccioni, F., Cerroni, P., Buratti, B. J., Clark, R. N., Stephan, K., and Plainaki, C., "Photometric Modeling and VIS-IR Albedo Maps of Dione From Cassini-VIMS," *Geophysical Research Letters*, Vol. 45, No. 5, 2018, pp. 2184–2192.

[40] Shkuratov, Y., Kaydash, V., Korokhin, V., Velikodsky, Y., Opanasenko, N., and Videen, G., "Optical measurements of the Moon as a tool to study its surface," *Planetary and Space Science*, Vol. 59, No. 13, Jun 2011, pp. 1326–1371.

[41] Filacchione, G., Capaccioni, F., Ciarniello, M., Clark, R., Cuzzi, J., Nicholson, P., Cruikshank, D., Hedman, M., Buratti, B., Lunine, J., and et al., "Saturn's icy satellites and rings investigated by Cassini–VIMS: III – Radial compositional variability," *Icarus*, Vol. 220, No. 2, 2012, pp. 1064–1096.

[42] MASTRAPA, R., BERNSTEIN, M., SANDFORD, S., ROUSH, T., CRUIKSHANK, D., and ORE, C., "Optical constants of amorphous and crystalline H2O-ice in the near infrared from 1.1 to 2.6 m," *Icarus*, Vol. 197, No. 1, 2008, pp. 307–320.

[43] Mastrapa, R. M., Sandford, S. A., Roush, T. L., Cruikshank, D. P., and Dalle Ore, C. M., "OPTICAL CONSTANTS OF AMORPHOUS AND CRYSTALLINE H2O-ICE: 2.5-22 m (4000-455 cm–1) OPTICAL CONSTANTS OF H2O-ICE," *The Astrophysical Journal*, Vol. 701, No. 2, 2009, pp. 1347–1356.

[44] Clark, R. N., Cruikshank, D. P., Jaumann, R., Brown, R. H., Stephan, K., Dalle Ore, C. M., Eric Livo, K., Pearson, N., Curchin, J. M., Hoefen, T. M., and et al., "The surface composition of iapetus: Mapping results from cassini VIMS," *Icarus*, Vol. 218, No. 2, Jan 2012, pp. 831–860.

[45] Warren, S. G., "Optical constants of ice from the ultraviolet to the microwave," *Applied Optics*, Vol. 23, No. 8, 1984, pp. 1206.

[46] Hapke, B., *Theory of reflectance and emittance spectroscopy*, Cambridge University Press, 2012.

[47] Hapke, B., "Bidirectional reflectance spectroscopy 7," *Icarus*, Vol. 221, No. 2, 2012, pp. 1079–1083.

[48] Fernando, J., Schmidt, F., and Douté, S., "Martian surface microtexture from orbital CRISM multi-angular observations: A new perspective for the characterization of the geological processes," *Planetary and Space Science*, Vol. 128, 2016, pp. 30–51.

[49] Verbiscer, A. J., Helfenstein, P., Buratti, B. J., and Royer, E., "Surface properties of Saturn's icy moons from Optical Remote Sensing," *Enceladus and the Icy Moons of Saturn*, 2018.

[50] Domingue, D. L., Denevi, B. W., Murchie, S. L., and Hash, C. D., "Application of multiple photometric models to disk-resolved measurements of Mercury's surface: Insights into Mercury's regolith characteristics," *Icarus*, Vol. 268, Apr 2016, pp. 172–203.

[51] Verbiscer, A. J., Helfenstein, P., Buratti, B. J., and Royer, E., "Surface properties of Saturn's icy moons from Optical Remote Sensing," *Enceladus and the Icy Moons of Saturn*, 2018.

[52] Bray, V. J., Öhman, T., and Hargitai, H., "Central peak crater," *Encyclopedia of Planetary Landforms*, 2014, pp. 1–9.

[53] Smoluchowski, R., "Solar system ice: Amorphous or crystalline?" *Science*, Vol. 222, No. 4620, 1983, pp. 161–163.

[54] Paranicas, C., Roussos, E., Krupp, N., Kollmann, P., Hendrix, A., Cassidy, T., Johnson, R., Schenk, P., Jones, G., Carbary, J., and et al., "Energetic charged particle weathering of Saturn's inner satellites," *Planetary and Space Science*, Vol. 61, No. 1, 2012, pp. 60–65.

[55] Taffin, C., Grasset, O., Le Menn, E., Bollengier, O., Giraud, M., and Le Mouélic, S., "Temperature and grain size dependence of near-IR spectral signature of crystalline water ice: From lab experiments to Enceladus' south pole," *Planetary and Space Science*, Vol. 61, No. 1, 2012, pp. 124–134.

[56] Jaumann, R., Stephan, K., Hansen, G., Clark, R., Buratti, B., Brown, R., Baines, K., Newman, S., Bellucci, G., Filacchione, G., and et al., "Distribution of icy particles across Enceladus' surface as derived from Cassini-VIMS measurements," *Icarus*, Vol. 193, No. 2, 2008, pp. 407–419.

[57] Porco, C., DiNino, D., and Nimmo, F., "How the geysers, tidal stresses, and thermal emission across the south polar terrain of Enceladus are related," *The Astronomical Journal*, Vol. 148, No. 3, 2014, pp. 45.

[58] Kouchi, A. and Kuroda, T., "Amorphization of cubic ice by ultraviolet irradiation," *Nature*, Vol. 344, No. 6262, 1990, pp. 134–135.

[59] Raponi, A., Ciarniello, M., Capaccioni, F., Filacchione, G., Tosi, F., De Sanctis, M. C., Capria, M. T., Barucci, M. A., Longobardo, A., Palomba, E., and et al., "The temporal evolution of exposed water ice-rich areas on the surface of 67P/Churyumov-Gerasimenko: spectral analysis," *Monthly Notices of the Royal Astronomical Society*, 2016.

[60] Filacchione, G., Capaccioni, F., Clark, R., Cuzzi, J., Cruikshank, D., Coradini, A., Cerroni, P., Nicholson, P., McCord, T., Brown, R., and et al., "Saturn's icy satellites investigated by Cassini–VIMS," *Icarus*, Vol. 206, No. 2, 2010, pp. 507–523.